The Dissertation Committee for Yeong-jun Choi Certifies that this is the approved version of the following dissertation:

Development of a Large Displacement Flexure Based Nano-Precision XY Positioning Stage for Vacuum Environments

Committee:

S.V. Sreenivasan, Supervisor

Joseph J. Beaman

Richard H. Crawford

Raul G. Longoria

Benjamin W. Mooring

Development of a Large Displacement Flexure Based Nano-Precision XY Positioning Stage for Vacuum Environments

by

Yeong-jun Choi, B.S., M.S.

Dissertation

Presented to the Faculty of the Graduate School of
The University of Texas at Austin
in Partial Fulfillment
of the Requirements
for the Degree of

Doctor of Philosophy

The University of Texas at Austin
December, 2003

Dedication

In his heart a man plans his course, but the LORD determines his steps.

(Proverbs 16:9)

Acknowledgements

This dissertation could not have been completed without the dedication and support of Associate Professor S.V. Sreenivasan, my supervisor. He gave me the opportunity to explore my interests in precision engineering and provided me with the drive to become an independent researcher. I would also like to thank all of dissertation committee members, Professor Joseph J. Beaman, Professor Richard H. Crawford, Associate Professor Raul G. Longoria, and Dr. Benjamin W. Mooring for their review of this dissertation with many valuable comments and suggestions. I would also like to thank the past graduates of the Sreenivasan group. In particular, I thank Jin and Mario for their help in the early stages of this research. Finally, the constant support and encouragement of my wife helped me overcome many of the obstacles.

This work was funded by the Defense Advanced Research Projects Agency (Grant No. MDA972-97-1-0010) and the Texas Higher Education Coordinating Board (Grant No. ATP003658-0574-2001).

Development of a Large Displacement Flexure Based Nano-Precision XY Positioning Stage for Vacuum Environments

Publication No._____________

Yeong-jun Choi, Ph.D

The University of Texas at Austin, 2003

Supervisor: S.V. Sreenivasan

Flexures are widely used in precision machines since they offer frictionless, particle-free, and low maintenance operation, and they provide extremely high resolution. Existing flexure-based translation stages usually have motion range to size ratios of less than 0.01 as compared 0.5 or higher in this research. It is believed that large motion flexure based XY stages can be a cost-effective solution for semiconductor applications, particularly the ones that operate in vacuum. The use of air bearings in vacuum leads to complicated designs making flexures attractive. Flexures also lead to less expensive designs as compared to magnetically-driven bearings.

This dissertation presents a large displacement flexure based nano-precision XY positioning stage for vacuum-based semiconductor equipment. The weight support mechanism of the motion stage is made of links and flexure joints, and a linear motor is used as the actuator. This stage is not a dual servo stage, but it can provide large motion range of greater than 8” x 8” to support a substrate during semiconductor manufacturing. An over-constrained mechanism is used to incorporate symmetry to cancel out the effects of center shifting in large motion flexures. Advanced kinematic techniques such as screw system theory are used to achieve a good kinematic design. Dynamic models are developed for fully compliant machines to understand the dynamic behavior of the flexure based XY stage. A single axis motion stage actuated by a high-resolution linear motor with a laser interferometer providing real-time position feedback has been fabricated. Experiments are performed to characterize motion straightness, repeatability, dynamic response of the motion stage.

This research is, to our knowledge, the first work for developing a macro motion stage that can support the weight of the stage and guide the motion by a mechanism based purely on flexure joints. A flexure-based XY stage can be potentially used to accurately place photomasks and wafers in an electron beam lithography machine, semiconductor steppers, wafer handling equipment, defect analysis machines in semiconductor industry, chip inspection tools, and coordinate measurement machines.

Table of Contents

List of Tables

List of Figures

Chapter 1: Introduction

1.1 MOTIVATION

Nano-precision XY stages form a critical subsystem of high-end semiconductor manufacturing equipment, precision machining centers, and inspection equipment. Ball screws and roller bearings have been traditionally used in XY stages, but both have two major drawbacks, backlash and stick-slip friction that decrease motion accuracy [Lee and Kim, 1997; Novak et al., 2000]. Further, these systems undergo wear over time, and lubrication makes it undesirable for vacuum or particle-sensitive applications. The repeatability of roller bearing stages is on the order of a few microns, not good for high precision application. Friction drive systems that cause wear and generate particles at the contact surfaces are not good in vacuum environments. Since air bearings do not have backlash and stick-slip friction, most of the state-of-the-art commercial semiconductor equipment suppliers now use some form of air bearing. However, it is difficult and expensive to use air bearings inside vacuum environments, because it requires complicated design to take away exhausted air. A new approach using magnetic levitation (mag-lev) has been recently proposed [Kim and Trumper, 1998; Williams et al., 1997] to enhance the position accuracy of motion stage and to eliminate undesirable dynamic effects such as friction and backlash. However, it is not yet used commercially due to its high cost, physical limits such as thermal dissipation problems and inherent interference with electron beams in commercial electron beam based patterning and inspection equipment.

Since linear motors are completely non-contact devices, there is no friction, no cogging, and no parts to wear. As a linear-motor-based system can provide high speeds and accelerations, linear motors are becoming widely accepted as the best actuators for ultra-high precision applications [Formica, 2001]. Flexures are widely used in precision machines since they offer frictionless, particle-free and low maintenance operation, and they provide extremely high resolution. Since notch type flexure joints are ideal for small motion range [Smith and Chetwynd, 1992], all positioning stages developed so far are useful for a few hundreds of micrometer range. To achieve high precision in large motion range, many researchers have studied dual servomechanism that has a fine motion stage mounted on a coarse motion stage. They used flexure joints for guidance in fine motion stages. Obviously dual servo stage makes the whole stage complex, and errors associated with coarse motion stage cause undesirable effect on the whole stage.

A large displacement flexure-based nano-precision XY positioning stage for vacuum-based semiconductor equipment has been developed in this research. The weight support mechanism of this XY stage is made of links and flexure joints, and linear motors are used as actuators. This stage is not a dual servo stage, but it can provide large motion range of greater than 8"×8" to support a substrate during semiconductor manufacturing.

1.2 LITERATURE SURVEY

This section describes previous works on other XY stages and flexure based XY stages.

Many XY stages which consist of linear motor and air bearing are commercially available, but there are a few that use air bearings inside vacuum. Novak et al. [2000] developed an electron projection lithography system that includes a precision XY stage. They used an air bearing inside a vacuum chamber. Bisschops and Vijfvinkel [2001] developed an air bearing inside vacuum. However, it is difficult and expensive to use air bearings inside vacuum environments, because it requires a complicated design to take away exhausted air.

As mentioned in the previous section, magnetic levitation has been recently proposed to enhance the position accuracy of a motion stage. The magnetic levitation stage designed by Williams et al. [1997] can travel 300 μm in X, Y, Z and milliradians of rotation. The position of this stage is controlled by twelve electromagnets. They found that the actuator core saturates when the gap or the coil current increases. The magnitude of the force generated by the actuator is 80 Newtons at an air-gap of 200 μm. Six capacitance gauges were used as position sensors. A positioning noise of 20 nm was obtained from step responses in the X direction. The magnetically levitated stage designed by Kim and Trumper [1998] has a travel of 50 mm in the X and Y directions, and 400 μm in the Z direction. The position sensors for measurement in the plane are three laser interferometers with sub-nanometer resolution. The position sensors for measurement out of the plane are three capacitance gauges with nanometer resolution. A positioning accuracy of 5 nm rms in the X and Y direction and a positioning accuracy of 10 nm rms in the Z direction were achieved from several experiments.

Some researchers are trying to develop direct drive XY stages. Tomita et al. [1996] developed a high response XY stage driven by in-parallel linear motors. They achieved the positioning accuracy of ±10 μm. Sprenger and Siegwart [1998] developed high speed 3 DOF linear direct drive stage similar to the previous design. This stage has a travel range of 60 × 60 mm with a resolution better than 100 nm.

Shamoto and Moriwaki [1997] developed a rigid X-Y-θ table for ultraprecision machine tool driven by means of walking drive. The walking drive utilizes piezoelectric actuator to make a long-range motion. The stage has the motion range of 100 × 40 mm and the positioning error less than 10 nm.

As an effort to eliminate undesirable characteristics such as friction and backlash in traditional joints, a flexure joint was proposed in the 1960s [Paros and Weisbord, 1965]. Figure 1.1 shows typical flexure joints that do not have stick-slip friction or backlash. Additional advantages of flexure joints are that they are wear free and can be made as a monolithic element. If the force-displacement curves are known, then the displacements that are continuous at all ranges can be calculated from the external force. However, these flexures have several disadvantages such as the limited range of motion and the poor behavior under multi-axis loading.

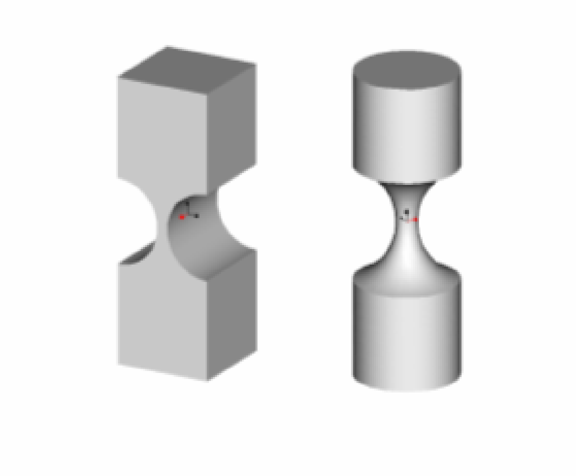

Figure 1.1 Typical flexure joints

The wire-type ball joint designed by Arai et al. [1993] does not appear to rotate much because of the working range of the whole system restricted to a fraction of a μm. The P-176.50/60 Flexible Tip of Physik Instrumente [1999] is a universal joint with the tilting angle of ±0.5°.

Goldfarb and Speich [1998, 1999] developed a new flexure revolute joint, called split-tube flexure. This has a large range of motion and better multi-axis loading behavior. The split-tube flexures have five times larger range of motion and the off-axis stiffness is three to four orders larger in magnitude than conventional flexures. Also the split-tube flexures have a fixed rotation axis, which contributes to a more accurate motion control. Goldfarb and Speich [1999] also mentioned some deficiencies of the split-tube flexures. The split-tube flexures are less compact and more difficult to fabricate than the conventional flexures. The contact between the links and the tube is not a precise line contact. This can bring geometric incompatibility and also increase the revolute stiffness. If the contact width can be reduced, this effect can be decreased.

Figure 1.2 depicts a crossed strip type flexure joint that provides large rotation. The Free-Flex Pivot made by Lucas Aerospace [1999] is a commercially available large deformation revolute flexure joint. This flexure does not have friction or backlash, and provides a large rotation of 60°. These flexure joints do not provide exact rotary motion over the entire 60° motion range. They can however, used in conjunction with symmetric kinematic designs, yield exact linear motion stages. Similar flexures made by C-Flex Bearing Inc. are used in this research.

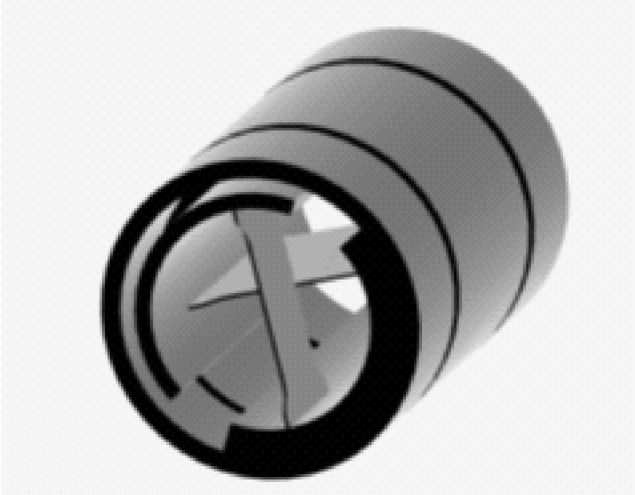

Figure 1.2 Crossed strip type flexure joint

Some researchers have developed high precision positioning systems using flexure joints. Tomita et al. [1992] developed a six D.O.F. fine motion stage that has a positioning resolution of 0.01 μm and 0.123 μrad. Spherical hinge flexures were used in this experiment. Rong and Zhu [1994] designed and analyzed a flexure-hinge mechanism that has a motion range of 100 μm and a positioning accuracy of 0.1 μm. Single-axis flexures and piezoelectric actuators are used in the motion stage. Yang et al. [1996] developed a micro-positioning stage that was actuated by piezo actuator and was guided by structure based on flexure joints. The motion range of that stage was only 200 μm. The comparison of static and dynamic characteristics between analytical model and FEM model was completed in that research. Ryu et al. [1997] developed a flexure hinge based X-Y-θ stage which has the total range of 41.5 × 47.8 μm. They presented an optimal design method. Tajbakhsh et al. [1998] used flexures to make a three D.O.F. optic mount with the motion limit of ±100 μm. The final accuracy is less than 10 nm and 0.5 μrad. The three D.O.F. finger module was introduced by Ohya et al. [1999]. The prototype includes a conventional flexure, a wire-type ball joint and a piezoelectric actuator. A repeatability of less than 0.1 μm and an absolute positioning accuracy of 2.0 μm were obtained from the experiments. They applied a wire as a ball joint that has a small working range. Commercially Physik Instrumente [2001] are selling P-731 Series X-Y Piezo Flexure Nano Positioners which can travel in ranges of 100 × 100 μm. The resolution of this mechanism is less than 1 nm in the X and Y direction and the repeatability is around ±5 nm. It uses low voltage PZTs (0 to 100 V) and flexures are used as the drive and guiding system. Integrated capacitive position feedback sensors provide sub-nanometer resolution. The flexures provide zero stiction/friction, ultra-high resolution and exceptional guiding precision. All positioning stages developed so far can give a few hundreds of micrometer motion range, because notch type flexure joints are adequate for small motion range.

In order to use flexure joints in large motion range, some researchers made dual servomechanism that has a fine motion stage mounted on a coarse motion stage. They incorporated flexure joints in fine motion stages. Lee and Kim [1997] presented an ultra precision three D.O.F. stage for alignment of wafers in micro lithography. For high precision they adopted a dual servo system and used flexures and piezoelectric actuators in the fine motion stage. The working range is 200 × 200 mm and the positioning reproducibility is 20 nm. Lee et al. [1998] developed an ultra precision positioning system using a dual servomechanism that consists of the global stage and the micro stage. The global stage can travel 40 cm and include a ball screw that has the position accuracy of 5 μm. Piezoelectric actuator actuates the micro stage connected by flexures. A position accuracy of 10 nm was obtained from this experiment. Dual servo stages make the whole stage complex, and errors associated with coarse motion stage degrade the performance of the whole stage.

Until now no research has been done on positioning system that can move large displacement only with flexure joints without using dual servo stages. This research is the first work for developing a macro motion stage that can support the weight of the stage and guide the motion by a mechanism based on flexure joints. As a complementary research, the tolerance analysis of a large displacement flexure-based overconstrained planar mechanism was performed by Szarka [2003] in the same research group. Szarka [2003] performed modeling and analysis of a large motion flexure-based XY stage in order to determine the causes of Y-motion deviation and stage angle deviation.

1.3 RESEARCH FOCUS

The hypothesis of this research is that it is possible to develop a large displacement flexure-based nano-precision XY positioning stage for vacuum environments.

Therefore, the objective of this research is to develop a large displacement flexure-based nano-precision XY positioning stage for vacuum-based semiconductor equipment. The following research works are performed.

Novel kinematic synthesis techniques are used to incorporate symmetry to cancel out the effects of ‘axis shifting’ in large motion flexures. Incorporation of symmetry can lead to undesirable singularities in mechanisms. Advanced kinematic techniques such as screw system theory are used to achieve a good kinematic design.

The kinematic and static analyses such as center shift analysis, mobility analysis, vertical deflection analysis, and position error analysis are performed. Dynamic models are developed for fully compliant machines to understand the dynamic behavior of the flexure XY stages. The prototype of the single axis flexure based motion stage is manufactured. The motion stage is actuated by a high-resolution linear motor with a laser interferometer providing real-time position feedback. The position control test by using PID controller is performed to find the control performance of the motion stage.

Horizontal straightness error, vertical deflection error, yaw, and pitch are observed experimentally by using the laser interferometer. Laser interferometers are used to characterize motion straightness over its entire range of motion. The repeatability tests are also carried out since the motion errors can be eliminated by using a lookup table. Modal test using accelerometers is performed to find the natural frequencies in the lateral and vertical direction.

1.4 ORGANIZATION

This chapter presents an introduction that includes motivation, literature survey, research focus, and organization. Chapter 2 explains the conceptual and detail design process of the proposed XY stage. Chapter 3 describes kinematic and static analysis, which includes center shift analysis of flexure joints, mobility analysis, deflection analysis, and position error analysis of the XY stage. Chapter 4 describes dynamic modeling, modal analysis, and control of the proposed motion stage. Then the experimental methods and results are demonstrated and discussed in Chapter 5, which covers horizontal straightness, yaw, their repeatability test, vertical deflection, pitch, their repeatability test, modal test, and control test. Finally, Chapter 6 presents concluding remarks, which summarizes conclusions and future works.

Chapter 2: Design of Flexure Based XY Stage

2.1 KINEMATIC DESIGN OF LINKAGE GUIDING MOTION

Figure 2.1 shows a double compound notch type small motion rectilinear spring that is used as the basic configuration for the new XY stage design. The moving body has one degree-of-freedom in its nominal configuration and has been used for small motion applications [Smith, 2000]. The nominal configuration as shown in Figure 2.1 is defined as the configuration with minimum strain energy. However, a mobility analysis based on Screw System Theory [Hunt, 1990] shows that the moving body has two degrees-of-freedom in its off-nominal configurations (see Figure 2.2). This mobility analysis is described in section 3.2. Therefore, the undesirable degree-of-freedom must be eliminated for a large motion application.

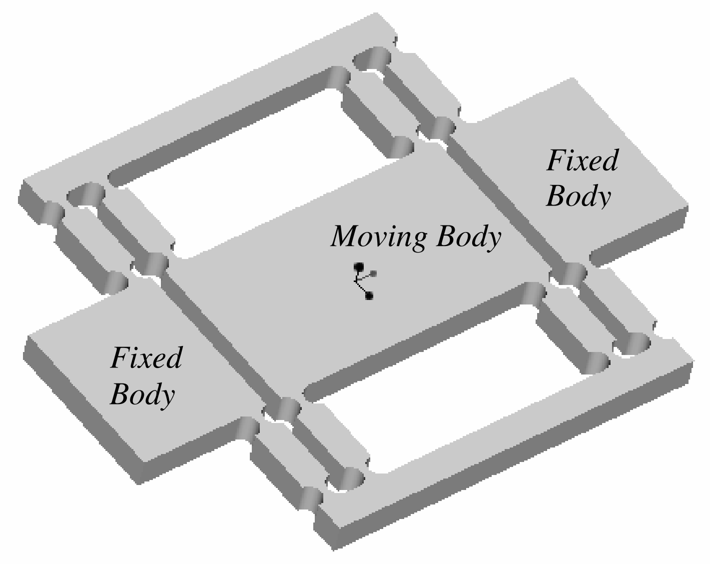

Figure 2.1 Double compound notch type small motion rectilinear spring

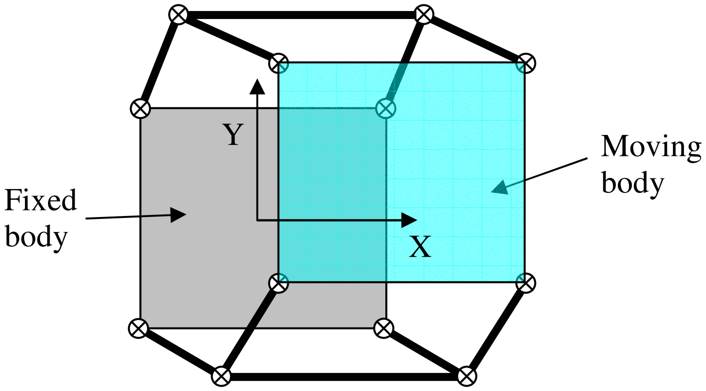

Figure 2.2 Two degree of freedom motion

The "Side Links" shown in Figure 2.3 eliminate this undesirable degree of freedom, which makes this stage one degree of freedom.

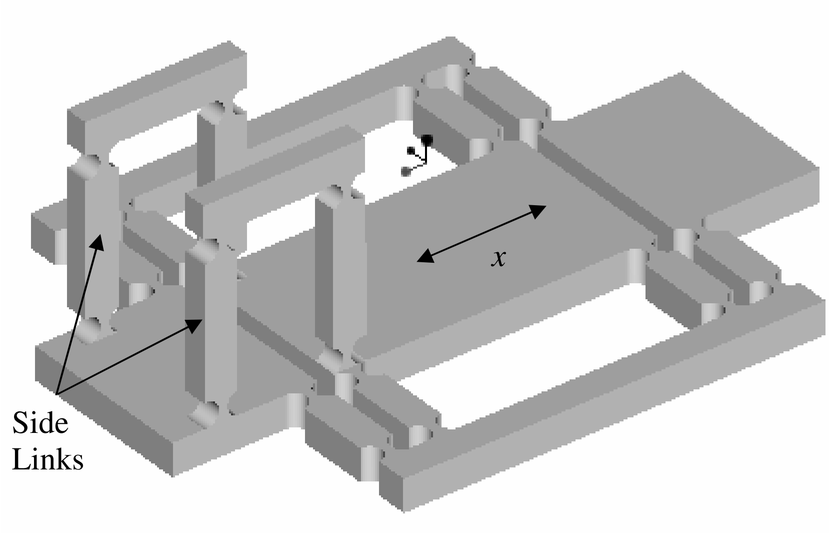

Figure 2.3 Modified one degree of freedom stage

Since semi-circular notch type flexures are ideal only for small motion range, large-motion flexure joints such as the one in Figure 1.2 are used here. However, when two stages are stacked orthogonal to each other to result in the XY stage, the actuation of one stage causes undesirable orthogonal excitations to the moving body. It is necessary to use additional linkages to eliminate the undesirable motion and constrain the moving body along the linear motion direction. Therefore, side links are installed at both sides of the moving body (see Figure 2.3).

Assuming that constraining linkages exist, the mechanism in Figure 2.3 can be optimized to lead to the smallest footprint for a 12" motion range. Figure 2.4 shows a schematic of the basic linkage in Figure 2.3. Links 1 and 3 are of the same length. When the moving body moves along X, all the joints in Figure 2.4 rotate by the same absolute angle. It should be noted that the motion range is independent of the length of the link 2. Due to kinematic constraints, link 2 remains parallel to the line connecting joints 1 and 4. The range of motion, x_{m}, is given by

$$x_m = 4 \cdot L \cdot sin(\theta) \tag{3.1}$$

where, θ is the angle of the joint 1, and L is the link length. Therefore, the link length is written by

$$L = \frac{x_m}{4 \cdot sin(\theta)} \tag{3.2}$$

The minimum link length for a 12" motion range is 6" when abs(θ_{max}) is 30°.

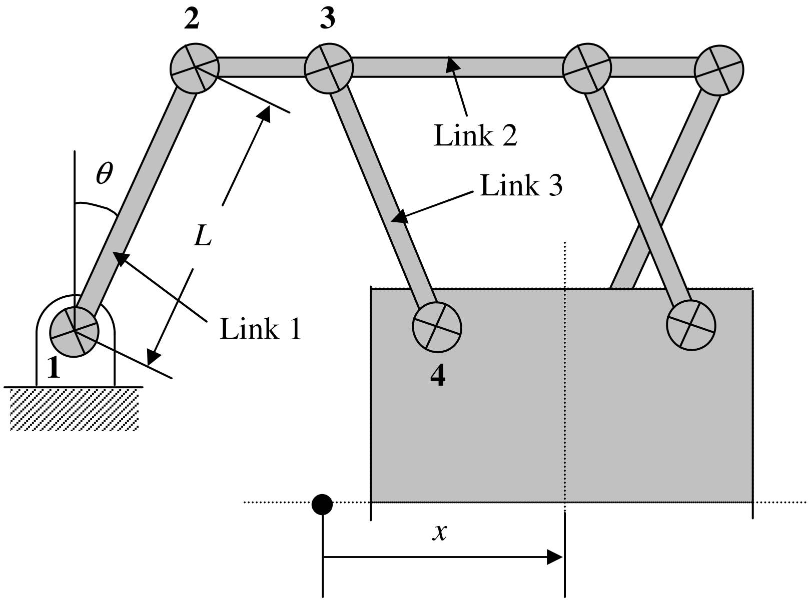

Figure 2.4 Linkage schematic for the stage

As mentioned earlier, an additional linkage system can be used to eliminate the undesirable motion (Y motion in Figure 2.2). Figure 2.5 represents the single axis motion stage based on the suggested mechanism. Figure 2.6 shows the three-dimensional model of the proposed XY stage and Figure 2.7 depicts the top and side view of the XY stage.

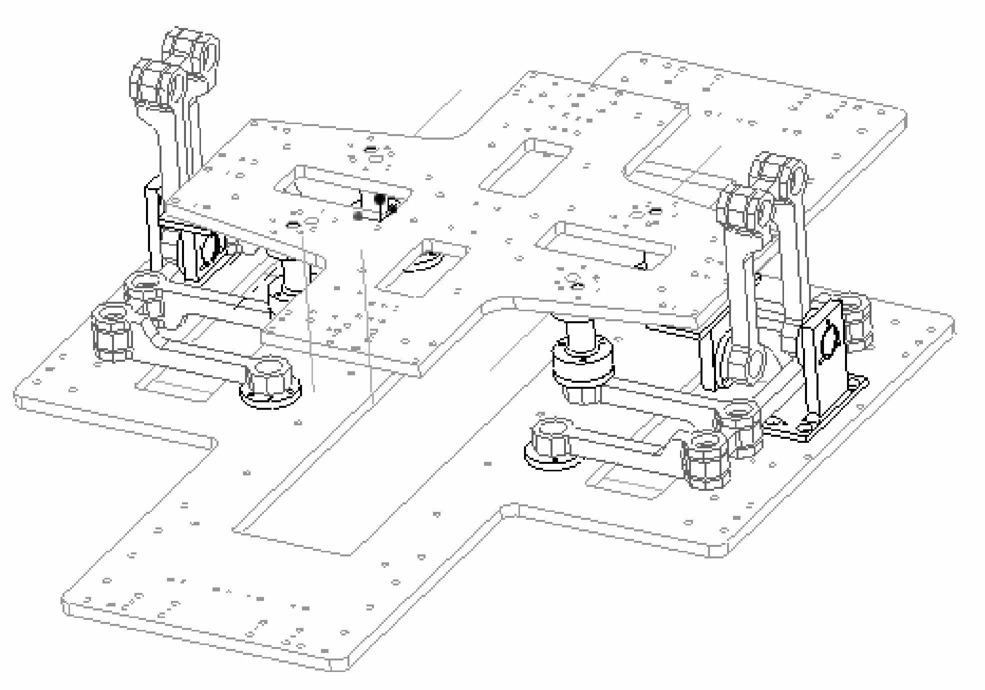

Figure 2.5 Proposed single axis motion stage

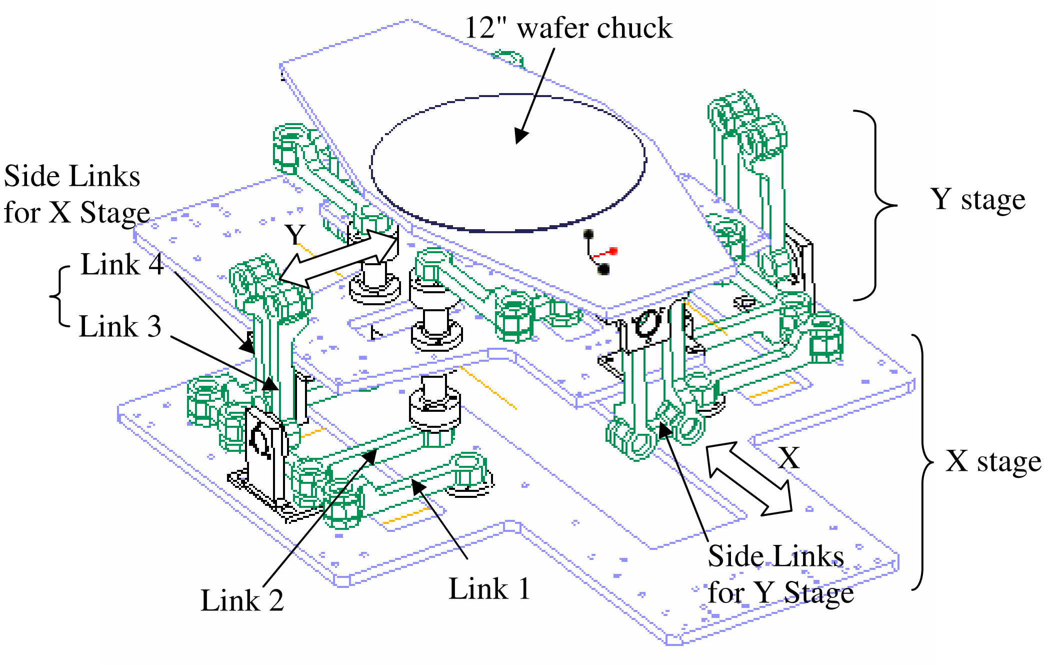

Figure 2.6 Proposed XY stage including side links

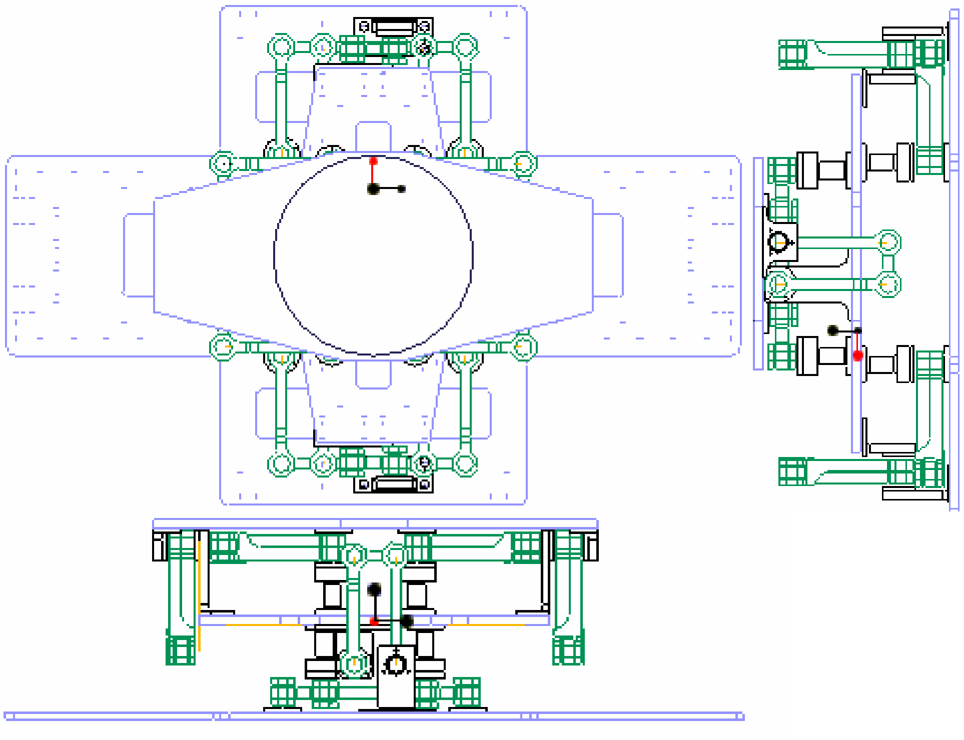

Figure 2.7 Top and side views of the proposed XY stage

2.2 REVISED DESIGN OF XY STAGE

Incorporation of symmetry can lead to undesirable singularities in mechanisms [Hunt, 1990]. From preliminary assembly of the proposed motion stage (see Figure 2.8 and Figure 2.9), an unexpected independent mode vibration problem was noticed. As shown in Figure 2.10, link 2 can vibrate independently in the nominal position, even when the moving plate is fixed at the nominal position. The screw analysis presented earlier did not account for this singularity because the analysis only studied the mobility of the moving plate.

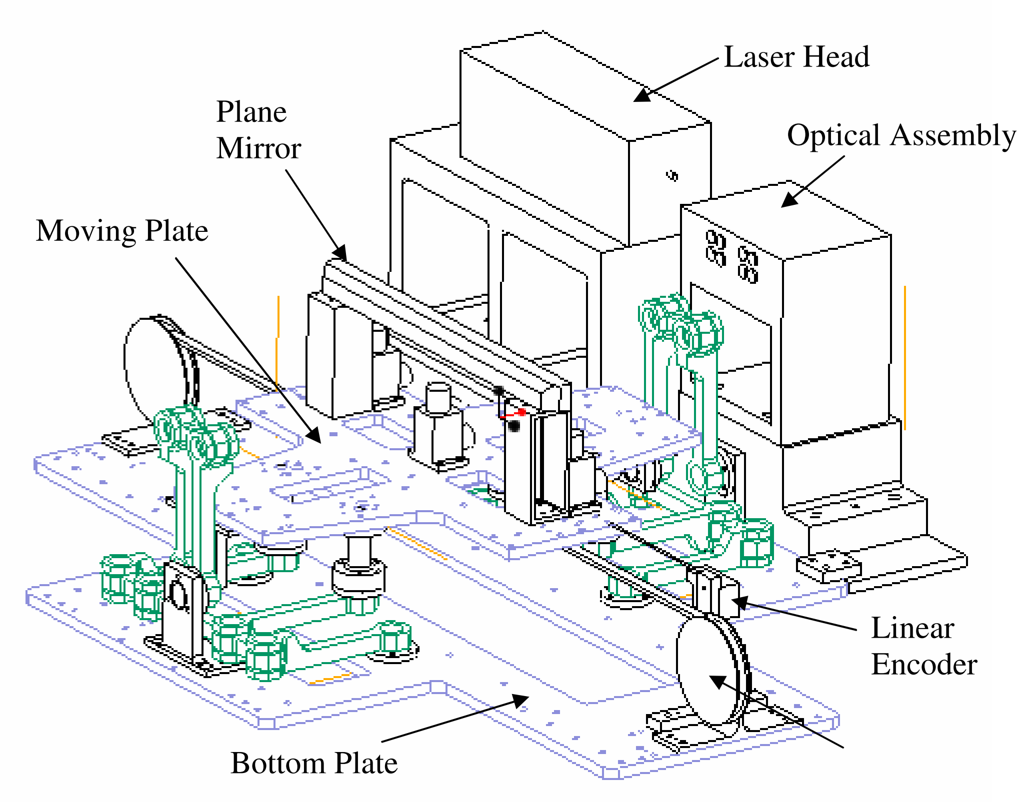

Figure 2.8 Assembly model of preliminary test setup

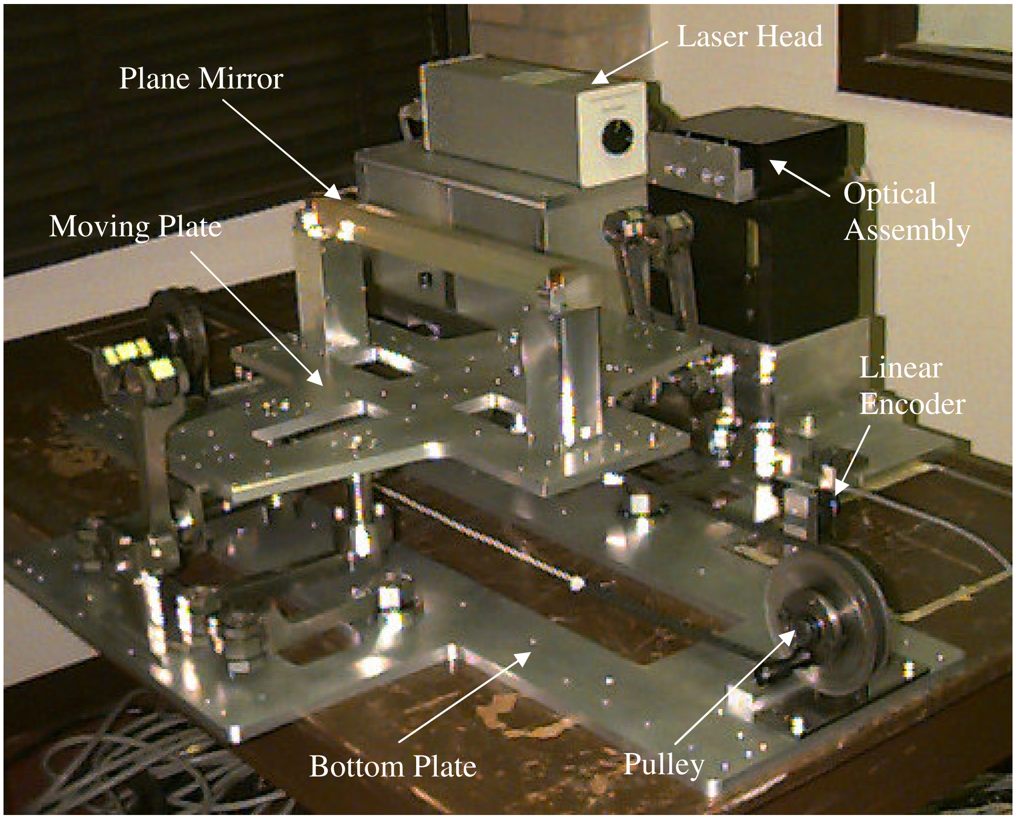

Figure 2.9 Photograph of preliminary test setup

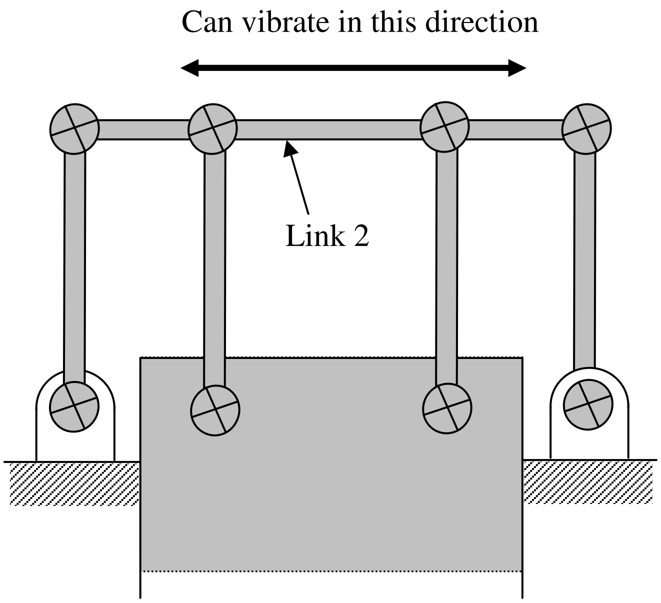

Figure 2.10 Independent vibration mode in nominal position

To prevent this independent vibration mode, the flexure joints are installed in the off-nominal configuration. This makes the nominal position of the entire linkage outside the motion range. Figure 2.11 depicts the new linkage structure with the modified design. Total travel range was reduced to 8 inches because of interference between linkages. Figure 2.12 depicts another method to prevent this independent vibration mode. In Figure 2.12, the links themselves cannot move even at nominal position since link A is longer than link B. This option was not chosen because the links vibrate very slightly at nominal position and it requires more machining change from the original system.

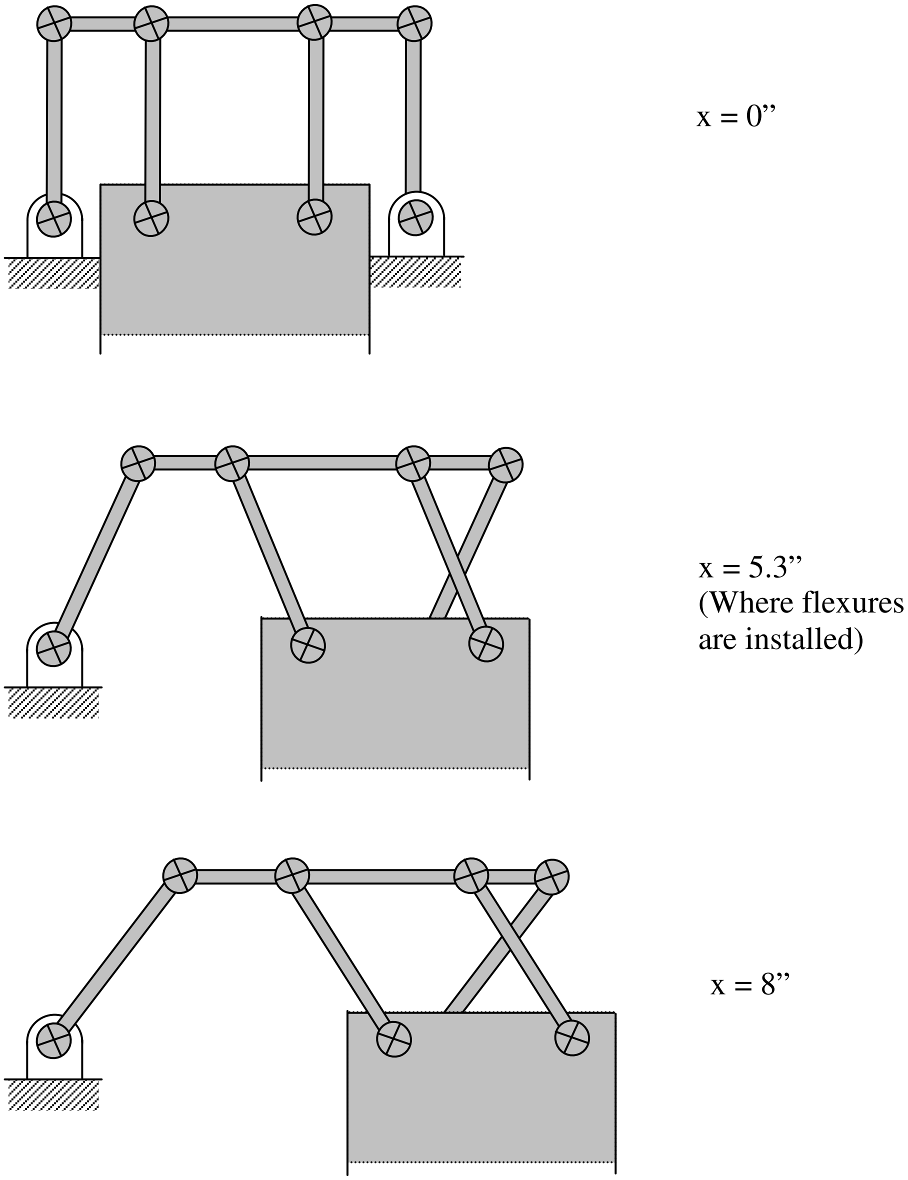

Figure 2.11 Selected method to prevent independent vibration

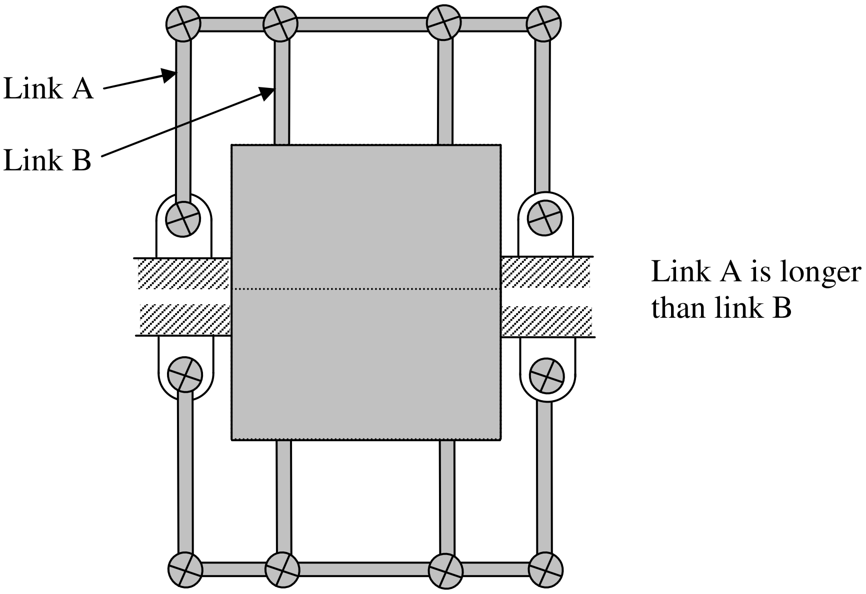

Figure 2.12 Another method to prevent independent vibration

Figure 2.13 shows the schematic of the modified side linkage to prevent independent vibration of the side linkage. These side linkages are oriented orthogonal to the XY plane and move in the XZ plane. Figure 2.14 represents the modified single axis motion stage. Figure 2.15 shows a modified 3D drawing of the resulting XY stage design and Figure 2.16 depicts top and side views of the new XY stage design. Figure 2.17 shows the close view of the side linkage and the planar linkage. Figure 2.18 through Figure 2.21 show the top views of the stage when the stage is at different positions.

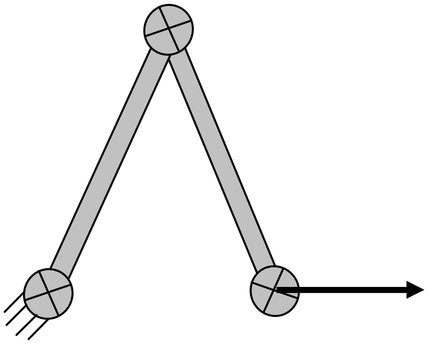

Figure 2.13 Schematic of modified side linkage

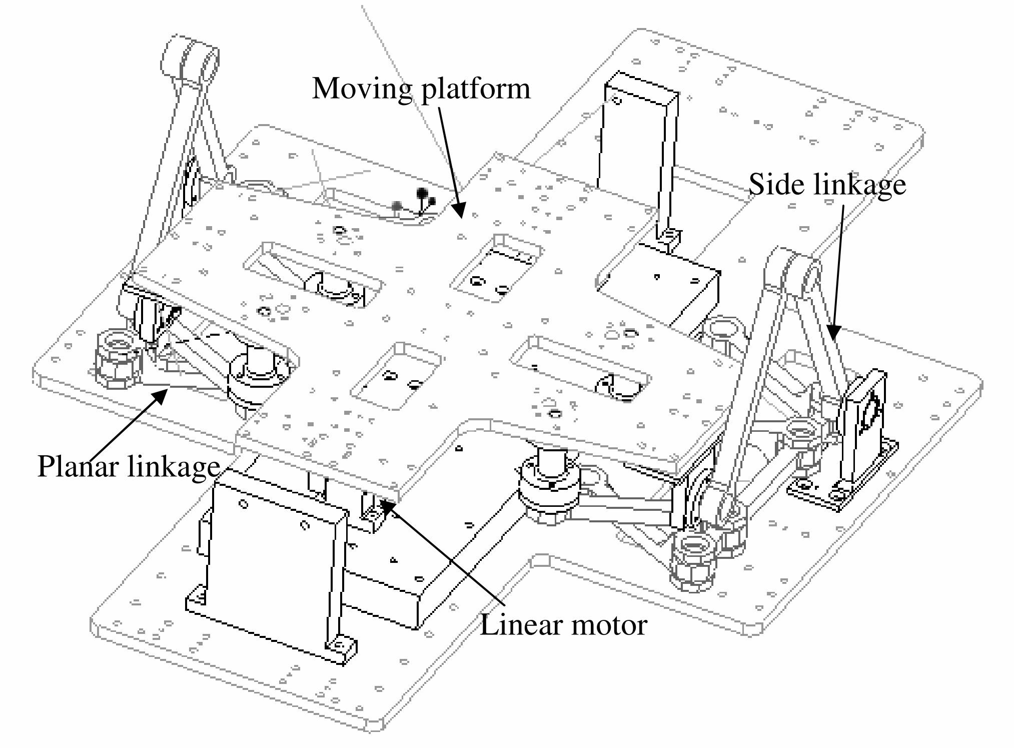

Figure 2.14 Modified single axis motion stage

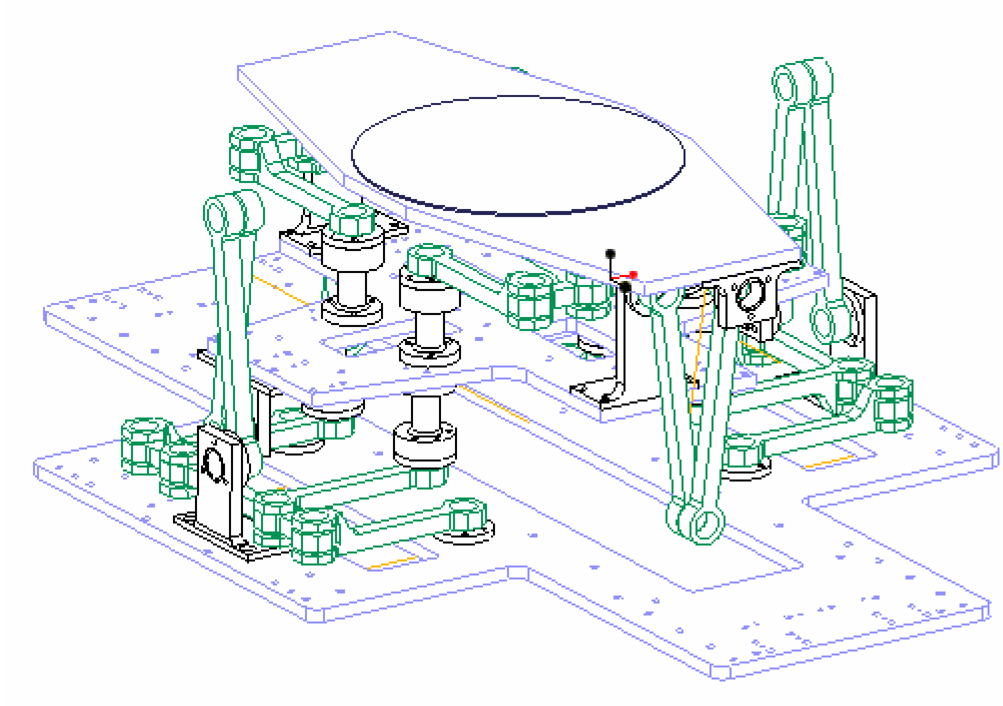

Figure 2.15 3-D model of modified XY stage

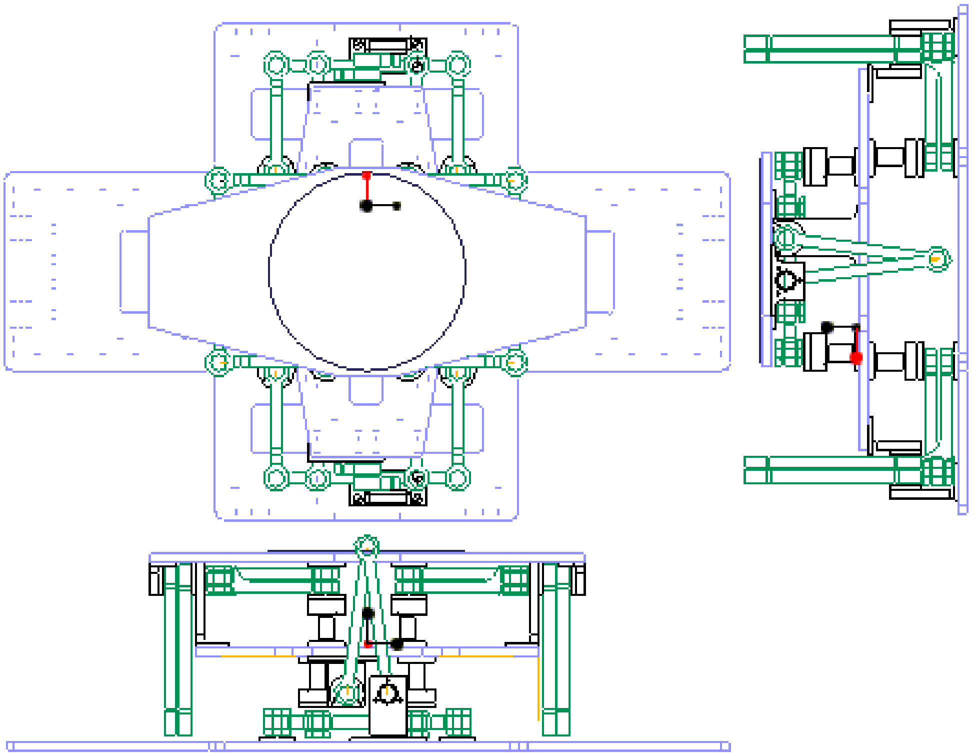

Figure 2.16 Top and side views of stage

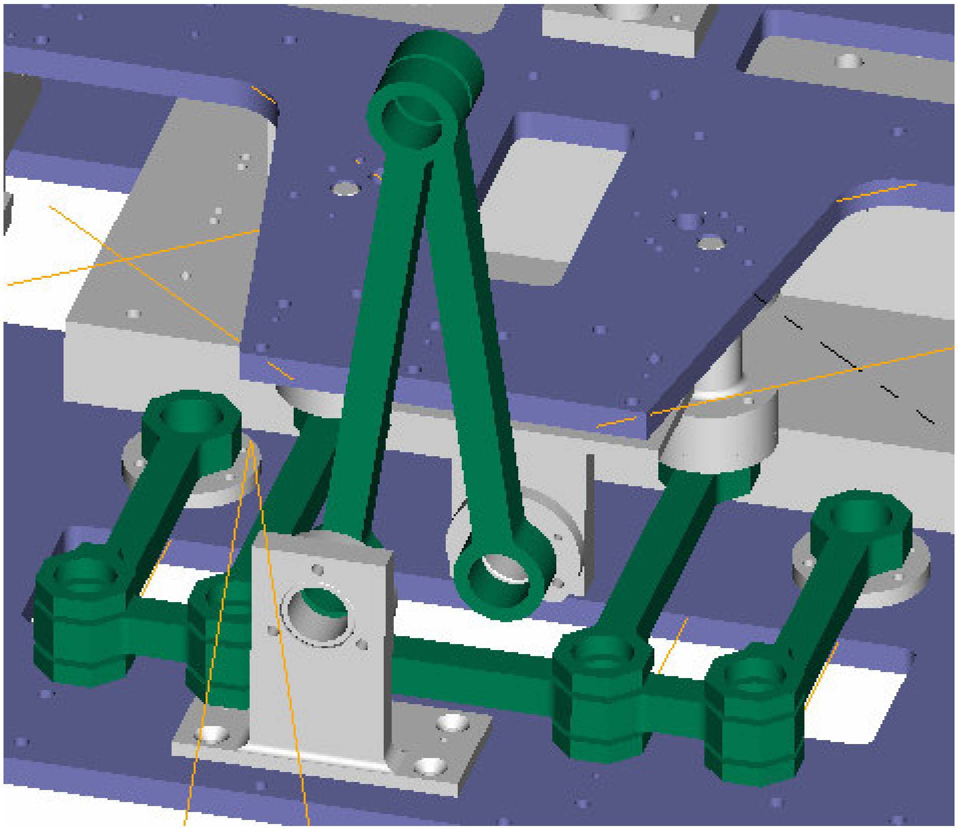

Figure 2.17 Close view of side linkage and planar linkage

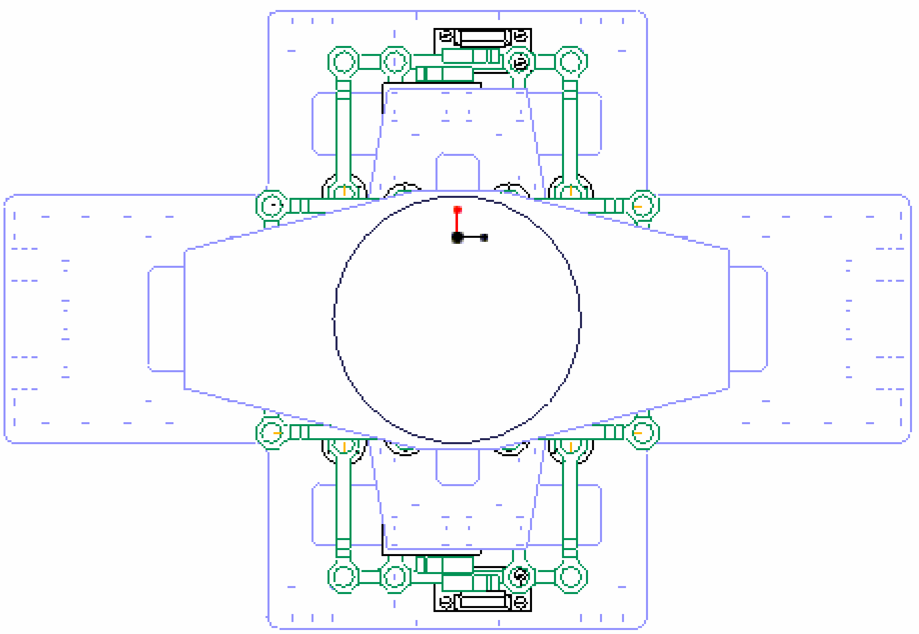

Figure 2.18 Stage (X = 0, Y = 0)

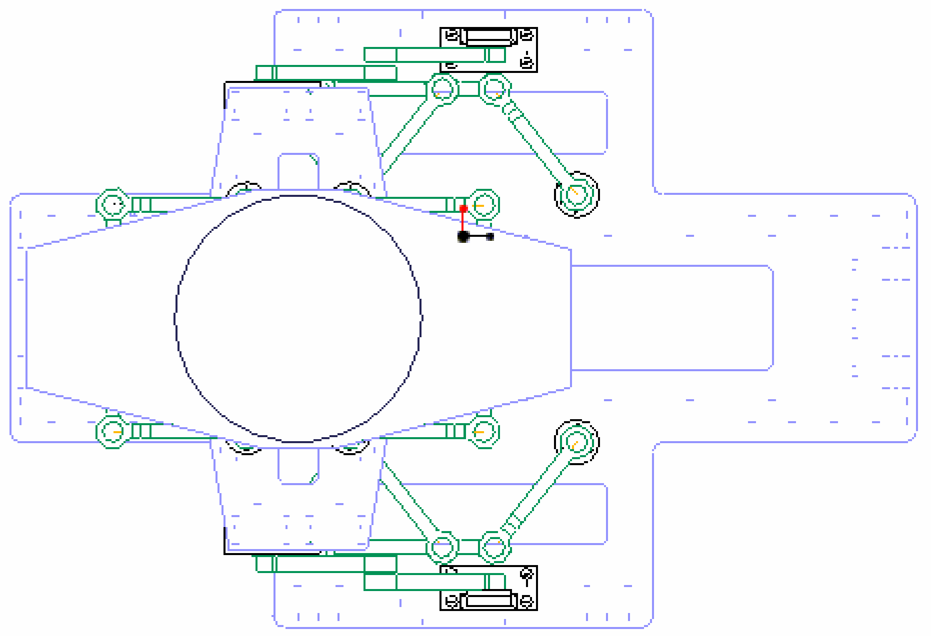

Figure 2.19 Stage (X = 8, Y = 0)

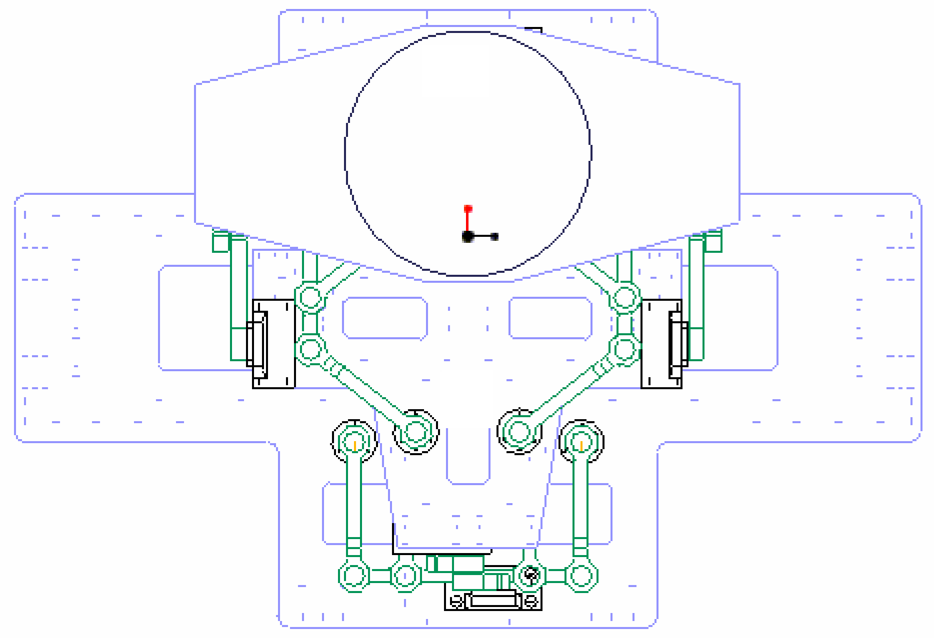

Figure 2.20 Stage (X = 0, Y = 8)

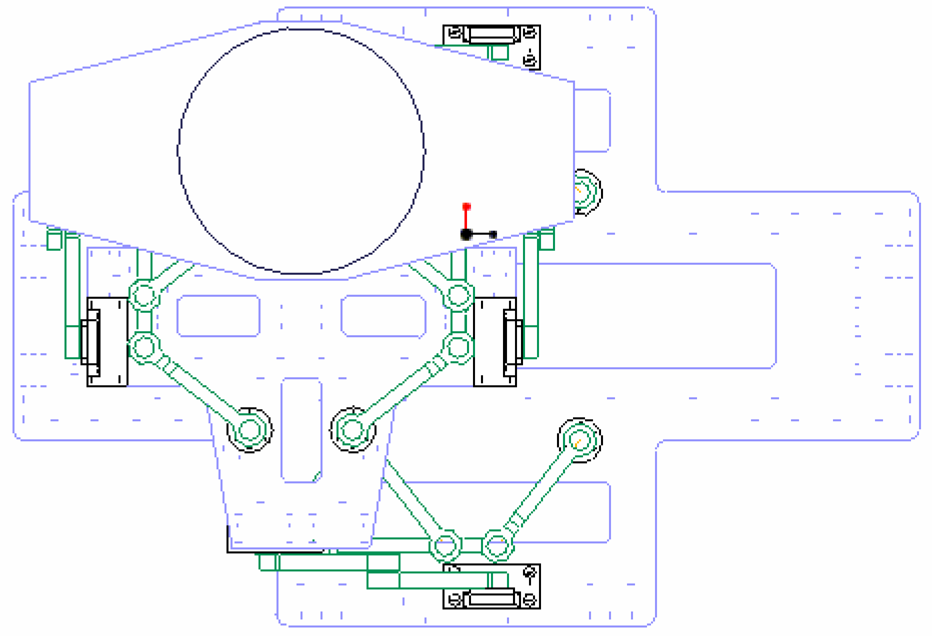

Figure 2.21 Stage (X = 8, Y = 8)

Chapter 3: Kinematic and Static Analysis of XY Stage

3.1 CENTER SHIFT ANALYSIS OF FLEXURE JOINT

3.1.1 Introduction

The flexural pivot has many advantages such as no rolling or Coulomb friction, no backlash, no lubrication, and applicability in vacuum. Some disadvantages, however, such as limited angular deformation, torsional spring load, and especially center shift may introduce inaccuracies in the positioning of a mechanical system using flexural joints. On the other hand, the cross strip flexural pivot has been found to provide relatively large angular deformation [Smith, 2000]. Figure 3.1 depicts a conventional cross strip flexural pivot that has limited application due to non-standardization. The modified flexural pivot that is used in this system is shown in Figure 3.2. The configuration of this pivot is based on the cross strip flexural pivot.

Figure 3.1 Conventional cross strip flexural pivot

Figure 3.2 Modified flexural pivot

3.1.2 Analysis of Center Shift of Flexural Pivot

3.1.2.1 Previous Works

For decades, researchers have been working on analyzing the center shift of the cross strip flexural pivot. Troeger [1962] defined the center as the intersection of the tangents to the neutral planes of the strips at their movable joints. The center shift of the flexural pivot used in this system can be defined as depicted in Figure 3.3. The magnitude of the center shift can be expressed by:

$$CS = (\sin\frac{\theta}{2} \Big/ \frac{\theta}{2} - \cos\frac{\theta}{2})D \text{ [Haringx, 1954]} \qquad (3.1)$$

$$CS = \frac{\sqrt{2}}{12}\theta^2 D \text{ [Troeger, 1962]} \qquad (3.2)$$

where CS is the center shift, θ is the deflection angle of the joint, and D is the length of the strip. Figure 3.4 shows the magnitudes of the center shifts of the flexural pivot with 1” outside diameter. The center shift data in the catalog of

Lucas Aerospace are between values of Equation (3.1) and (3.2). Both equations do not exactly match the values in the catalog of Lucas Aerospace because Troeger [1962] used 0.6D to compensate for the actual length of the strip in the flexural pivot. More accurate results were obtained in this research by using 0.69D instead of 0.6D, upon measuring the dimension of the real flexural pivot.

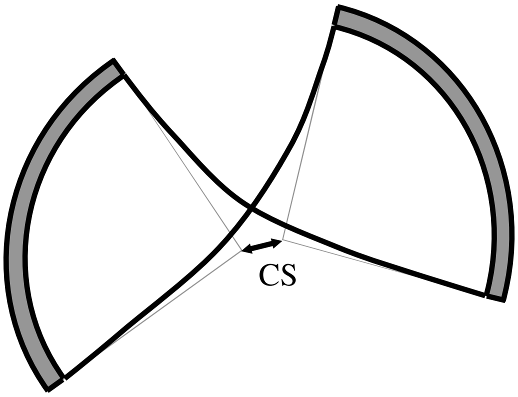

Figure 3.3 Definition of center shift

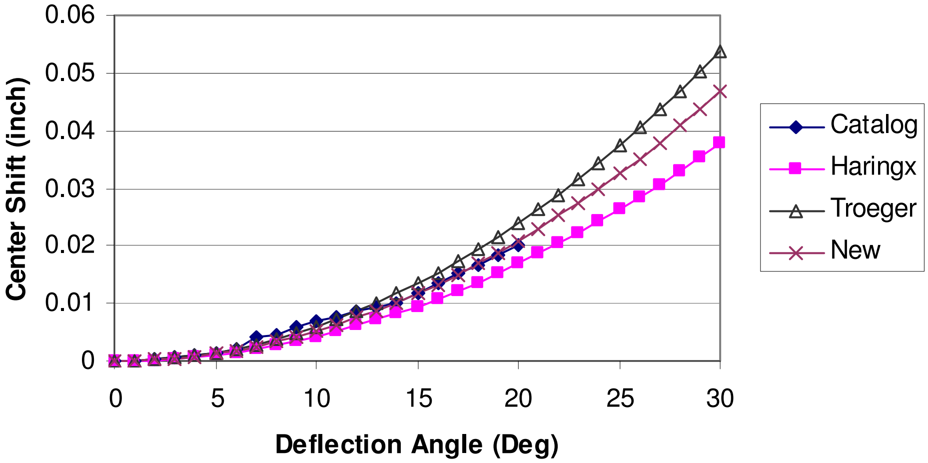

Figure 3.4 Center shift of flexural pivot

3.1.2.2 FEM Analysis

During this research, in order to get more accurate results, Finite Element Analysis was performed using Pro-MECHANICA Software. Figure 3.5 shows the model of the flexural pivot in a Pro-MECHANICA window. Since a problem associated with radial constraint occurred in the analysis of the actual model, the simplified model was used for the analysis. With the actual model, the moving cylindrical part showed radial expansion in all radial directions when it rotates. These phenomena were observed both in Pro-Mechanica and in I-DEAS. Figure 3.5 (a) is an actual model of the flexural pivot, and 3.5 (b) shows a simplified model used for the FEM analysis. A top view of the deformed shape of the simplified model is shown in Figure 3.6.

Figure 3.7 compares the center shift calculated by FEM with that calculated by the new analytical equation. The center shift calculated by FEM considers the displacement of the middle point of the outer ring of the moving part. As can be seen in Figure 3.7, the center shift calculated by FEM is very similar to the theoretical result.

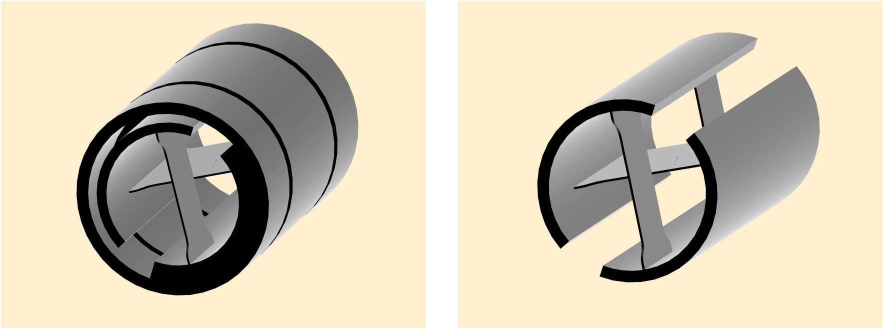

(a) The same model (b) Simplified model

Figure 3.5 CAD model of flexural pivot

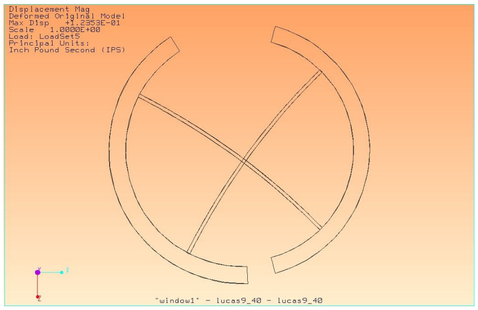

```
Displacement Mag
Deformed Original Model
Max Disp    +1.2353E-01
Scale    1.0000E+00
Load: LoadSet5
Principal Units:
Inch Pound Second (IPS)
```

```
"window1" - lucas9_40 - lucas9_40
```

Figure 3.6 Deformation result of flexural pivot in Pro-Mechanica

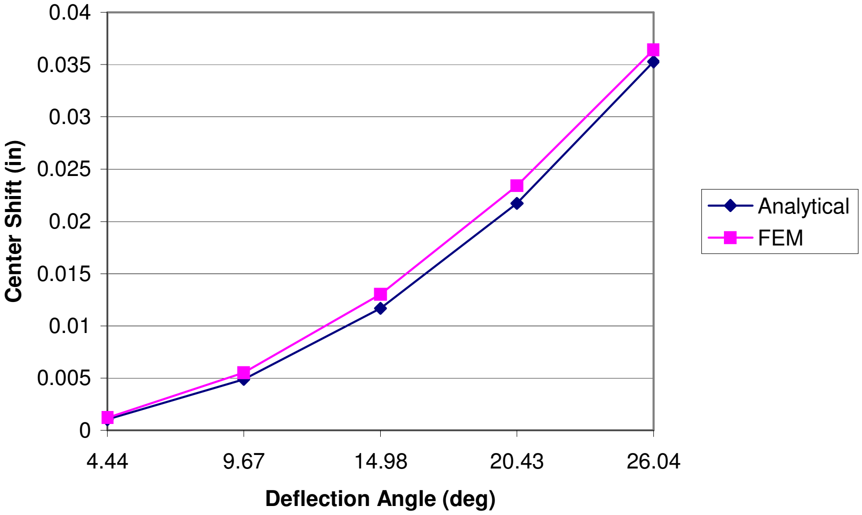

Figure 3.7 FEM and analytical solution of center shift

For the case of complex loading, since the center shift is a function of the deflection angle and the X stage has a symmetrical structure, it is assumed that the center shift does not make any significant error in the direction perpendicular to the moving direction of the stage.

3.2 MOBILITY ANALYSIS

The mobility of a double compound notch type rectilinear spring shown in Figure 2.1 is given by

$$M = 3(n-1) - 2j = 3(12-1) - 2(16) = 1 \tag{3.4}$$

where M is the mobility, n is the number of links, and j is the number of joints. This is only applicable when the stage is in its nominal configuration.

The actual mobility of the mechanism in its off-nominal position can be found by using screw system theory. More detailed descriptions related to screw system theory can be found in Hunt [1990]. Figure 3.8 shows the schematic for mobility analysis. Points A, B, C, and D are located in the center of link 2 or the edge of the moving body.

The motor of point A of link 2, $\mathbf{v_A}$, can be obtained simultaneously starting at joint 1 or joint 3. The resultant motors from the two starting points should be same.

The screw of point A by joint 1, $\mathbf{\$_1}$, can be given by

$$\mathbf{\$_1} = \begin{pmatrix} \mathbf{w_1} \\ \boldsymbol{\rho}_\mathbf{1} \times \mathbf{w_1} \end{pmatrix} \tag{3.5}$$

where

$$\mathbf{w_1} = \begin{pmatrix} 0 \\ 0 \\ 1 \end{pmatrix} \qquad \boldsymbol{\rho}_\mathbf{1} \times \mathbf{w_1} = \begin{vmatrix} \mathbf{i} & \mathbf{j} & \mathbf{k} \\ l_{1x} + l_2 & l_{1y} & 0 \\ 0 & 0 & 1 \end{vmatrix} = \begin{pmatrix} l_{1y} \\ -(l_{1x} + l_2) \\ 0 \end{pmatrix} \tag{3.6}$$

where l_2 is the length of link 1 ($l_{1x} = l_1 cos\theta$, $l_{1y} = l_1 sin\theta$) and also equal to half of the length of link 2, $\boldsymbol{\rho}_1$ is the position vector of point A relative to joint 1, and $\mathbf{w}_1$ is the screw axis direction by joint 1.

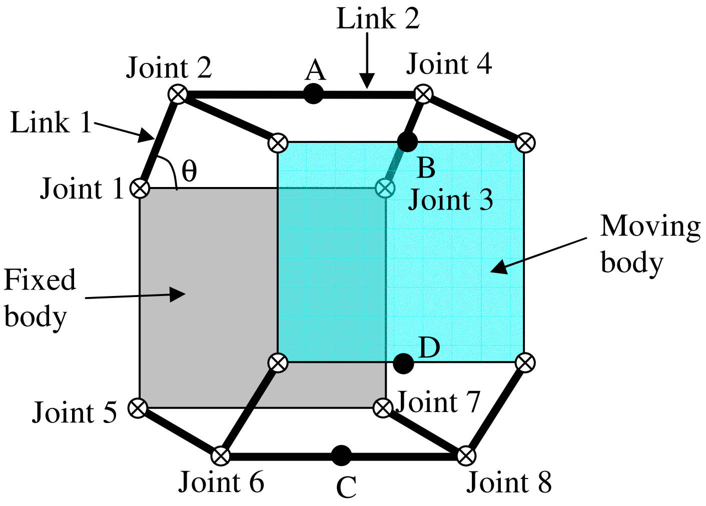

Figure 3.8 Schematic for mobility analysis

The screw of point A by joint 2, $\$_2$, can be given by

$$\$_2 = \begin{pmatrix} \mathbf{w}_2 \\ \boldsymbol{\rho}_2 \times \mathbf{w}_2 \end{pmatrix} \tag{3.7}$$

where

$$\mathbf{w}_2 = \begin{pmatrix} 0 \\ 0 \\ 1 \end{pmatrix} \qquad \boldsymbol{\rho}_2 \times \mathbf{w}_2 = \begin{vmatrix} \mathbf{i} & \mathbf{j} & \mathbf{k} \\ l_2 & 0 & 0 \\ 0 & 0 & 1 \end{vmatrix} = \begin{pmatrix} 0 \\ -l_2 \\ 0 \end{pmatrix} \tag{3.8}$$

where $\boldsymbol{\rho}_2$ is the position vector of point A relative to joint 2, and $\mathbf{w}_2$ is the screw axis direction by joint 2.

The resultant screw axes $\$_1$ and $\$_2$ are given by

$$\$_1 = \begin{pmatrix} 0 \\ 0 \\ 1 \\ l_{1y} \\ -(l_{1x} + l_2) \\ 0 \end{pmatrix} \qquad \$_2 = \begin{pmatrix} 0 \\ 0 \\ 1 \\ 0 \\ -l_2 \\ 0 \end{pmatrix} \tag{3.9}$$

The motor of point A of link 2, $\mathbf{v_A}$, starting at joint 1 can be written by

$$\mathbf{v_A} = \omega_1 \$_1 + \omega_2 \$_2 \tag{3.10}$$

where ω_1 and ω_2 are the scalar angular velocities of the screw axes $\$_1$ and $\$_2$ respectively.

The motor of point A of link 2, $\mathbf{v_A}$, starting at joint 3 can be calculated by a similar procedure.

The screw of point A by joint 3, $\$_3$, can be given by

$$\$_3 = \begin{pmatrix} \mathbf{w}_3 \\ \boldsymbol{\rho}_3 \times \mathbf{w}_3 \end{pmatrix} \tag{3.11}$$

where

$$\mathbf{w_3} = \begin{pmatrix} 0 \\ 0 \\ 1 \end{pmatrix} \qquad \boldsymbol{\rho}_\mathbf{3} \times \mathbf{w_3} = \begin{vmatrix} \mathbf{i} & \mathbf{j} & \mathbf{k} \\ l_{1x} - l_2 & l_{1y} & 0 \\ 0 & 0 & 1 \end{vmatrix} = \begin{pmatrix} l_{1y} \\ l_2 - l_{1x}\,) \\ 0 \end{pmatrix} \tag{3.12}$$

where $\boldsymbol{\rho}_\mathbf{3}$ is the position vector of point A relative to joint 3, and $\mathbf{w_3}$ is the screw axis direction by joint 3.

The screw of point A by joint 4, $\mathbf{\$_4}$, can be given by

$$\mathbf{\$_4} = \begin{pmatrix} \mathbf{w_4} \\ \boldsymbol{\rho}_\mathbf{4} \times \mathbf{w_4} \end{pmatrix} \tag{3.13}$$

where

$$\mathbf{w_4} = \begin{pmatrix} 0 \\ 0 \\ 1 \end{pmatrix} \qquad \boldsymbol{\rho}_\mathbf{4} \times \mathbf{w_4} = \begin{vmatrix} \mathbf{i} & \mathbf{j} & \mathbf{k} \\ -l_2 & 0 & 0 \\ 0 & 0 & 1 \end{vmatrix} = \begin{pmatrix} 0 \\ l_2 \\ 0 \end{pmatrix} \tag{3.14}$$

where $\boldsymbol{\rho}_\mathbf{4}$ is the position vector of point A relative to joint 4, and $\mathbf{w_4}$ is the screw axis direction by joint 4.

The resultant screw axes $\mathbf{\$_3}$ and $\mathbf{\$_4}$ are given by

$$\mathbf{\$_3} = \begin{pmatrix} 0 \\ 0 \\ 1 \\ l_{1y} \\ l_2 - l_{1x} \\ 0 \end{pmatrix} \qquad \mathbf{\$_4} = \begin{pmatrix} 0 \\ 0 \\ 1 \\ 0 \\ l_2 \\ 0 \end{pmatrix} \tag{3.15}$$

The motor of point A of link 2, $\mathbf{v_A}$, starting at joint 3 can be written by

$$\mathbf{v_A} = \omega_3 \mathbf{\$_3} + \omega_4 \mathbf{\$_4} \tag{3.16}$$

where ω_3 and ω_4 are the scalar angular velocities of the screw axes $\mathbf{\$_3}$ and $\mathbf{\$_4}$ respectively.

Since Equations (3.7) and (3.11) should be equal, the following relation can be obtained.

$$\begin{pmatrix} 0 \\ 0 \\ \omega_1 + \omega_2 \\ \omega_1 l_{1y} \\ -\omega_1 (l_{1x} + l_2) - \omega_2 l_2 \\ 0 \end{pmatrix} = \begin{pmatrix} 0 \\ 0 \\ \omega_3 + \omega_4 \\ \omega_3 l_{1y} \\ \omega_3 (l_2 - l_{1x}) + \omega_4 l_2 \\ 0 \end{pmatrix} \tag{3.17}$$

Equation (3.13) can be rewritten by

$$\begin{aligned} &\omega_1 + \omega_2 = \omega_3 + \omega_4 \\ &\omega_1 l_{1y} = \omega_3 l_{1y} \\ &-\omega_1 (l_{1x} + l_2) - \omega_2 l_2 = \omega_3 (l_2 - l_{1x}) + \omega_4 l_2 \end{aligned} \tag{3.18}$$

Therefore,

$$\begin{aligned}\omega_2 &= \omega_4 \\ \omega_1 &= \omega_3 \\ \omega_2 &= -\omega_1\end{aligned} \tag{3.19}$$

The motor of link 2, $\mathbf{v_A}$, can be simplified by

$$\mathbf{v_A} = \begin{pmatrix}0 & 0 & 0 & \omega_1 l_{1y} & -\omega_1 l_{1x} & 0\end{pmatrix}^{\mathbf{T}} \tag{3.20}$$

Similarly, the motor of point B of the moving body, $\mathbf{v_B}'$, relative to the link 2 can be written by

$$\mathbf{v_B}' = \begin{pmatrix}0 & 0 & 0 & -\omega_2' l_{1y} & \omega_2' l_{1x} & 0\end{pmatrix}^{\mathbf{T}} \tag{3.21}$$

where ω_2' is the scalar angular velocity of the screw axis of point B by joint 2.

The motor of point B of the moving body, $\mathbf{v_B}$, is the sum of $\mathbf{v_A}$ and $\mathbf{v_B}'$ given by

$$\mathbf{v_B} = \begin{pmatrix}0 & 0 & 0 & \omega_1 l_{1y} - \omega_2' l_{1y} & -\omega_1 l_{1x} - \omega_2' l_{1x} & 0\end{pmatrix}^{\mathbf{T}} \tag{3.22}$$

Similarly, the motor of point D of the moving body, $\mathbf{v_D}$, starting at joints 5 and 7 can be expressed by

$$\mathbf{v_D} = \begin{pmatrix} 0 & 0 & 0 & \omega_5 l_{1y} - \omega_6' l_{1y} & \omega_5 l_{1x} - \omega_6' l_{1x} & 0 \end{pmatrix}^{\mathbf{T}} \tag{3.23}$$

where ω_5 and ω_6' are the scalar angular velocities of the corresponding screw axes.

Since equation (3.15) and (3.16) should be equal, the following relations can be derived.

$$\begin{aligned} \omega_1 - \omega_2' &= \omega_5 - \omega_6' \\ -\omega_1 - \omega_2' &= \omega_5 + \omega_6' \end{aligned} \tag{3.24}$$

Since the number of equations is two and the number of arbitrary variables is four, the degree of freedom of this system is two.

3.3 VERTICAL DEFLECTION ANALYSIS

The designed XY stage consists of many links and flexure joints that show compliant behavior. Therefore, the vertical deflection can have undesirable effects on the performance of the stage. The vertical deflection varies with the position of the stage because of the different vertical loading conditions with position.

Figure 3.9 shows the schematic of the half portion of the moving stage. Major deflections can occur in link 1, link 2, link 3, and the flexure joints. It is assumed that the vertical forces are applied at each contact point equally (A and B in Figure 3.9), so the vertical load at the end of each link 1 is the total weight divided by four.

Link 1 in Figure 3.9 can be simplified as a cantilever beam shown in Figure 3.10. It is assumed that link 1 has the boundary condition of zero deflection angles at both ends. From the boundary condition, the deflection can be calculated by using superposition of force and moment effects as

$$\delta_1 = \frac{PL_1^3}{3EI_1}, \quad \varphi_1 = \frac{PL_1^2}{2EI_1} \tag{3.25}$$

$$\delta_2 = \frac{ML_1^2}{2EI_1}, \quad \varphi_2 = \frac{ML_1}{EI_1} \tag{3.26}$$

where P = applied force (same as W/4)

M = applied moment

L_1 = length of link 1

E = Young's modulus of link1

I_1 = moment of inertia of link 1

δ_1 = deflection due to force

δ_2 = deflection due to moment

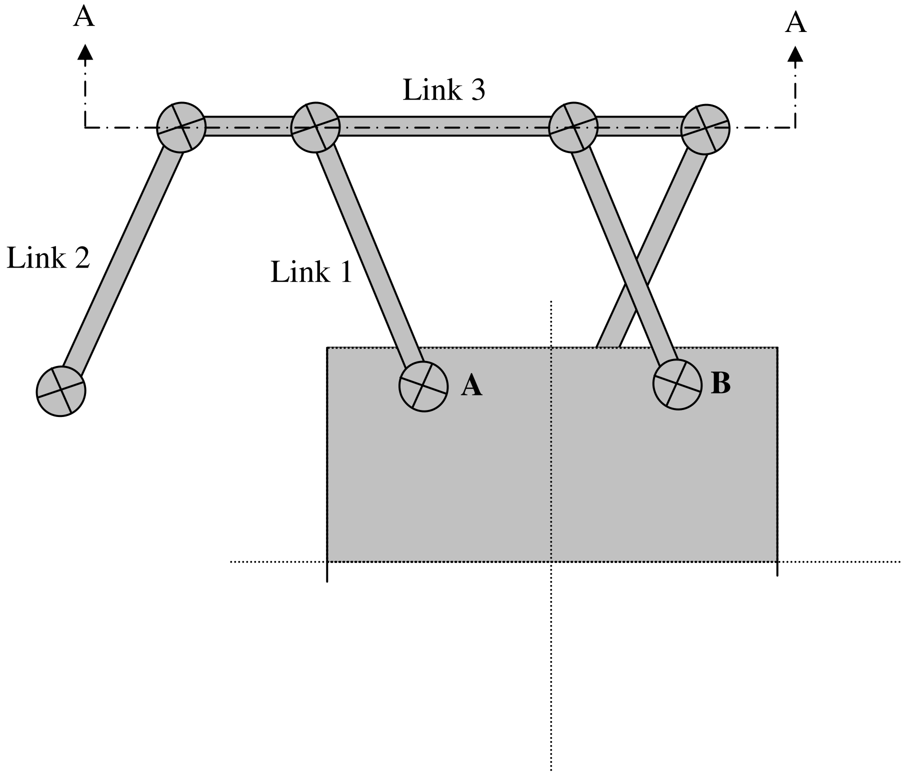

Figure 3.9 Schematic of the half portion of the stage

By applying the boundary condition, the unknown moment can be calculated by

$$\varphi = \varphi_1 - \varphi_2 = \frac{PL_1^{\,2}}{2EI_1} - \frac{ML_1}{EI_1} = 0 \quad \Rightarrow \quad \therefore M = \frac{PL_1}{2} \tag{3.27}$$

The total deflection (δ) is given by

$$\delta = \delta_1 - \delta_2 = \frac{PL_1^{\,3}}{3EI_1} - \frac{ML_1^{\,2}}{2EI_1} = \frac{PL_1^{\,3}}{12EI_1} \tag{3.28}$$

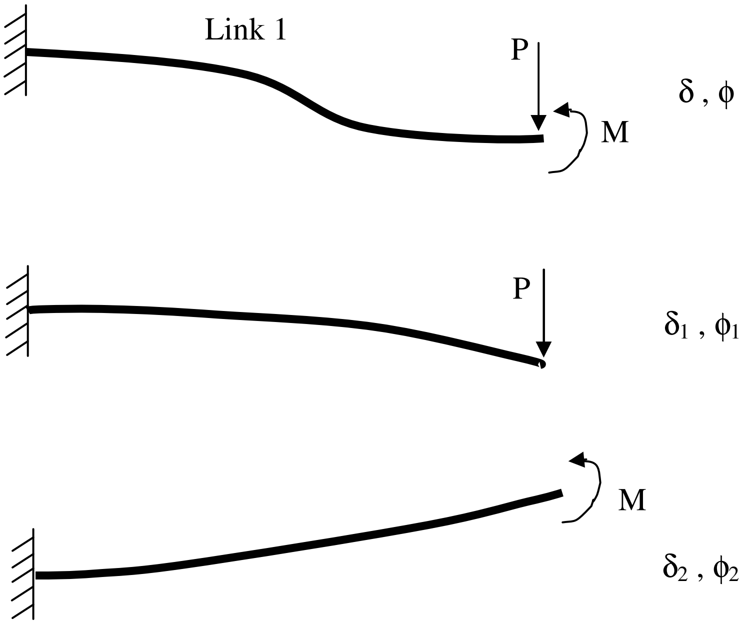

Figure 3.10 Cantilever beam simplifying link 1

A similar approach can be applied for link 2 in Figure 3.9, so the deflection is the same as the result above.

Vertical deflection can also occur in the flexure joints. The bending stiffness of the flexure joints should be considered to find the vertical deflection of the flexure joints. Figure 3.11 depicts the strip inside the flexure joint. If the bending stiffness of the strip is compared with that of link 1, the vertical deflectin due to the bending of the strip can be estimated.

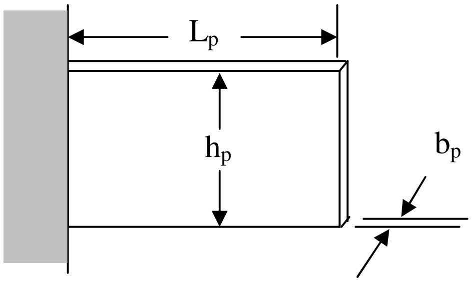

Figure 3.11 Strip inside the flexure pivot

The ratio between the bending stiffness of the strip and that of link 1 is given by

$$\frac{L_1^3 / EI_1}{L_p^3 / EI_p} = 10.96 \tag{3.29}$$

From this result, the bending effect of the strip can be neglected, so only the axial stiffness of the flexure joints contributes significant vertical deflection.

Other significant effects come from torsion and bending of link 3 in Figure 3.9. It is assumed that the end points at link 3 are simply supported. With this assumption, the vertical deflection can easily be calculated. Figure 3.12 depicts the loading condition in the deflection analysis of link 3. The external loads are the vertical force, the bending moment, and the torsion at the point connecting link 1 and link 3. It can be assumed that the vertical forces do not vary with position, but the bending moment (M) and torsion (T) vary with position as written by

$$M = \frac{W}{4} L_1 sin\theta , \qquad T = \frac{W}{4} L_1 cos\theta \tag{3.30}$$

where θ is the deflection angle of the flexure joints and W is the weight of the moving platform.

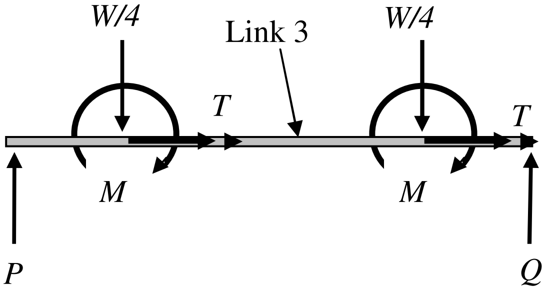

Figure 3.12 Loading condition in link 3

Figure 3.13 shows the cross section of link 3. Since link 3 has a rectangular cross section, the torsional deflection angle is given by

$$\varphi = \frac{TL_3}{c_2 Gab^3} \tag{3.31}$$

where ϕ = deflection angle of link 3

L_3 = distance between the end point and the loading point in the link 3

c_2 = coefficient for the torsion of a rectangular shaft (= 0.141)

G = shear modulus of link 3

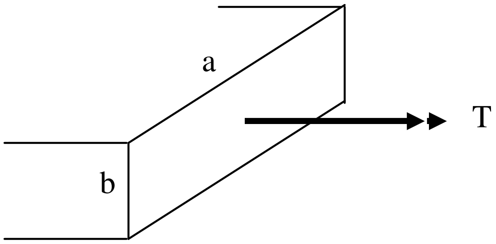

Figure 3.13 Cross section of link 3

The total deflections at point A and B in Figure 3.9 that are functions of position are given by

$$
\begin{aligned}
\delta_A(\theta) = {} & 2 \cdot \frac{\frac{W}{4} L_1^{3} + \frac{\omega L_1^{4}}{2}}{12EI_1} + 4 \cdot \frac{\frac{W}{4}}{KAc} + \frac{TL_1L_2\cos\theta}{c_2Gab^{3}} \\
& - \frac{\frac{W}{4}\left(2L_2 + L_3 - L_1\sin\theta\right)L_2^{3}}{6EI_2\left(2L_2 + L_3\right)} \\
& + \frac{\frac{W}{4}\left(2L_2 + L_3 - L_1\sin\theta\right)\left(2L_2 + L_3\right)L_2}{EI_2} \\
& - \frac{\frac{W}{24}\left(L_2 + L_3\right)^{3} L_2}{EI_2\left(2L_2 + L_3\right)} + \frac{\frac{W}{8} L_1L_2\left(L_2 + L_3\right)^{2}\sin\theta}{EI_2\left(2L_2 + L_3\right)} \\
& - \frac{\frac{W}{24} L_2^{4}}{EI_2\left(2L_2 + L_3\right)} + \frac{\frac{W}{8} L_1L_2^{3}\sin\theta}{EI_2\left(2L_2 + L_3\right)} \qquad (3.32)
\end{aligned}
$$

where *KAc* is the compressive stiffness of the flexure joint and L_2 is the length of link2.

$$
\begin{aligned}
\delta_B(\theta) = {} & 2 \cdot \frac{\frac{W}{4} L_1^{3} + \frac{\omega L_1^{4}}{2}}{12EI_1} + 4 \cdot \frac{\frac{W}{4}}{KAc} + \frac{TL_1 L_2 cos\theta}{c_2 Gab^{3}} \\
& - \frac{\frac{W}{4}\left(2L_2 + L_3 - L_1 sin\theta\right)\left(L_2 + L_3\right)^{3}}{6EI_2\left(2L_2 + L_3\right)} \\
& + \frac{\frac{W}{24} L_3^{3}}{EI_2} - \frac{\frac{W}{8} L_1 L_3^{2} sin\theta}{EI_2} \\
& + \frac{\frac{W}{4}\left(2L_2 + L_3 - L_1 sin\theta\right)\left(2L_2 + L_3\right)\left(L_2 + L_3\right)}{EI_2} \\
& - \frac{\frac{W}{24}\left(L_2 + L_3\right)^{4}}{EI_2\left(2L_2 + L_3\right)} + \frac{\frac{W}{8} L_1\left(L_2 + L_3\right)^{3} sin\theta}{EI_2\left(2L_2 + L_3\right)} \\
& - \frac{\frac{W}{24} L_2^{3}\left(L_2 + L_3\right)}{EI_2\left(2L_2 + L_3\right)} + \frac{\frac{W}{8} L_1 L_2^{2}\left(L_2 + L_3\right) sin\theta}{EI_2\left(2L_2 + L_3\right)}
\end{aligned}
\tag{3.33}
$$

Table 3.1 shows the summary of the total deflection analysis with different materials for the links in the upper and lower stage. The deflections vary with position of the stage. The two points (point A and B in Figure 3.9) six inches apart from each other along the motion axis are used for calculation. The differences between the two points are small compared to the total deflection values in every case, which show the low pitch error of the stage. Aluminum alloy or stainless steel is used as material for all the links. Obviously the vertical deflection is smaller with stainless steel than with aluminum alloy. If aluminum alloy is used for the links of the upper stage and stainless steel for the lower stage, the smallest vertical deflection in the lower stage can be obtained. On the other hand, the smallest total deflection can result in the case of all stainless steel links. The maximum deflections for the upper stage and the lower stage are 133 μm and 260 μm respectively for the case of all stainless steel links. The minimum deflections for the upper stage and the lower stage are 92 μm and 233 μm, respectively. Figure 3.14 and 3.15 show the results of the vertical deflection at points A and B of the upper and lower stage with all stainless steel links. Figure 3.16 represents the pitch of the upper and lower stage. The calculated maximum pitches are -6.3×10^{-10} radian for the upper stage and -1.8×10^{-9} radian for the lower stage.

Table 3.1 Summary of deflection analysis

Material for Link 1, 2, & 3		**Vertical Deflection (μm)**				**Total Maximum Deflection**
Upper Stage	**Lower Stage**	**Upper Stage**		**Lower Stage**		
		Min	max	Min	Max	
Al Alloy	**Al Alloy**	203	323	447	534	**857**
Stainless Steel	**Stainless Steel**	92	133	233	260	**393**
Al Alloy	**Stainless Steel**	267	320	212	239	**559**

Since the vertical deflection varies with position, this error motion should be compensated by adding a vertical stage when the vertical deflection is critical in the application.

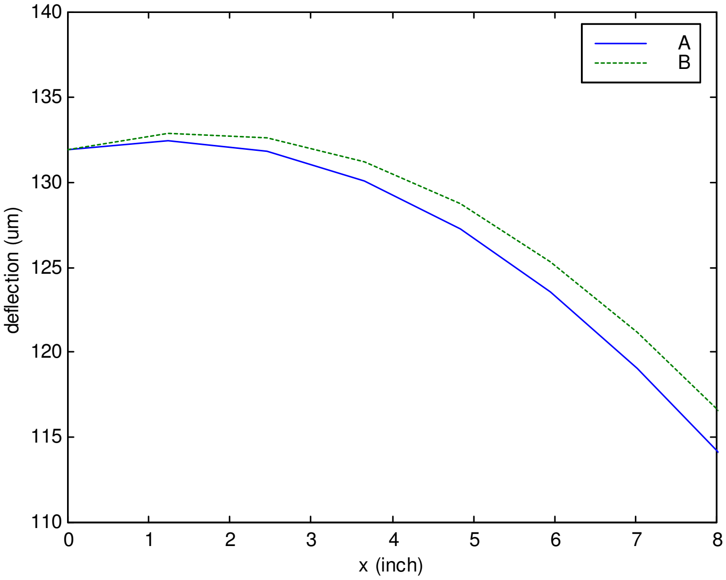

Figure 3.14 Deflection of upper stage

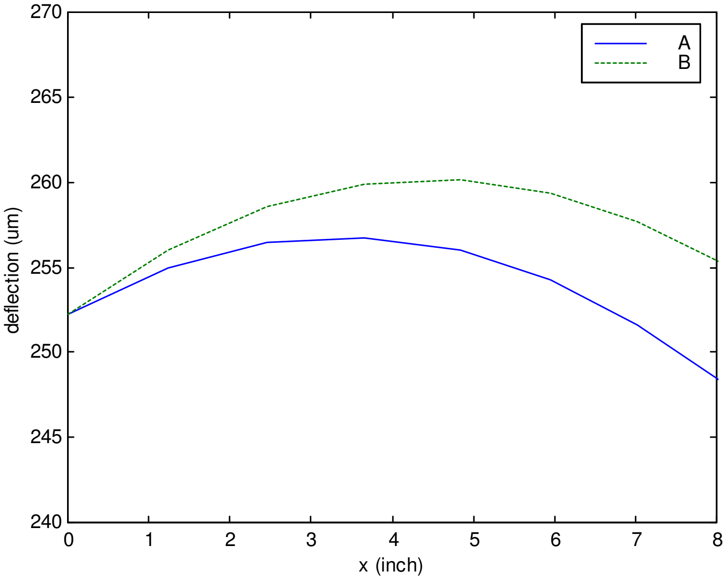

Figure 3.15 Deflection of lower stage

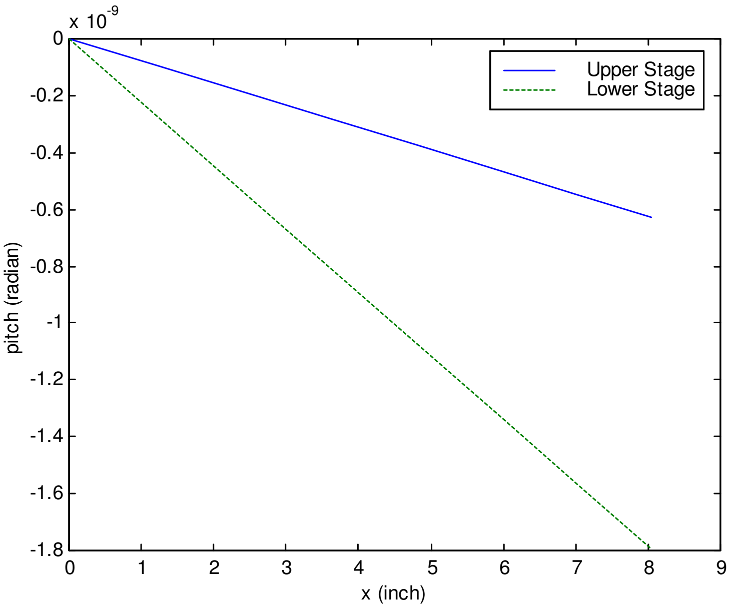

Figure 3.16 Pitch of upper and lower stage

3.4 POSITION ERROR ANALYSIS

There are many sources that can be contributed to the position error of the proposed XY stage. The dimensional tolerance, limited by the accuracy of the machining equipment, is a primary source, but it is difficult to calculate the effect of the dimensional tolerance mathematically since this system is an over-constrained mechanism. Kinematic analysis is not enough for calculation of the effect; it is necessary to do deformation analysis as well. The misalignment of the linkages during the assembly process can be a major source for the position error. This misalignment introduces undesirable deformations in the flexure joints. If these deformations produce an undesirable moment on the moving plate, the moment can affect the position accuracy of the stage. In this section, only the effect of this misalignment on horizontal straightness and yaw error will be demonstrated.

Figure 3.17 depicts a misalignment case during the assembly of the side linkage. The angular error causes the flexure joints to be deflected slightly from the desirable position. If the flexure joints generate a torque caused by the angular error, as shown in Figure 3.18 the corresponding horizontal force can be given by

$$Fs = (T1+T2+T3)/h \tag{3.34}$$

If the forces at both ends of the side linkages are applied in opposite direction, an undesirable moment can occur as shown in Figure 3.19. The undesirable moment can make the moving platform rotate.

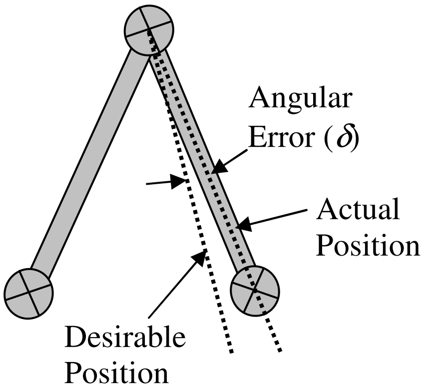

Figure 3.17 Misalignment during the assembly of the side linkage

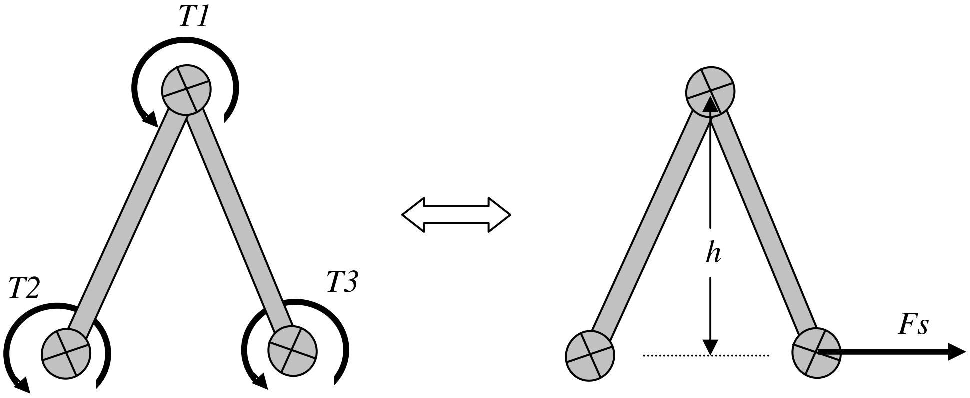

Figure 3.18 Corresponding horizontal force

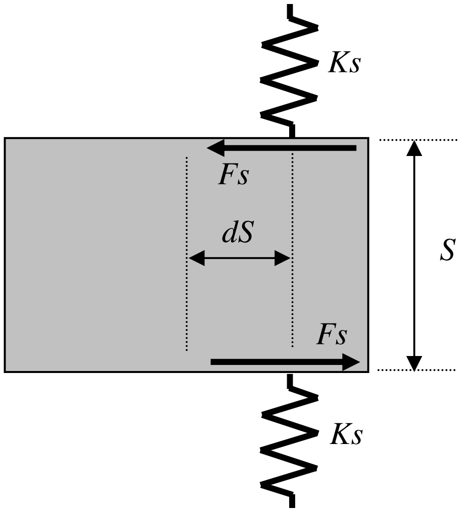

dS = Distance between center of moving platform and connected position of side linkage
S = Distance between front and rear side linkage
Fs = Force induced by misalignment of side linkage
Ks = Stiffness of side linkage

Figure 3.19 Undesirable loading

The angular deflection can also occur in the planar linkage structure. By using a similar method, the stage may generate a moment that can cause the angular deflection of the moving stage (see Figure 3.20 ~ 3.22).

The total angular deflection should be calculated by the sum of moments due to both the planar and the side linkages. Figure 3.23 shows the calculated result of the yaw error. The maximum error is $-3.3\cdot10^{-7}$ radian.

There are several other error sources such as the unequal spring constants of the flexure joints installed, machining errors of the links and the holes, the assembly errors of planar and side linkage, and so on. It is difficult to find which of these sources affects the motion error, quantitatively. Therefore, it is necessary to perform experiments such as straightness tests to find the actual error of the stage. In addition, Szarka [2003] in the same research group performed tolerance analysis of a large motion flexure-based XY stage to determine the causes of Y-motion deviation and stage angle deviation seen during preliminary testing of the device.

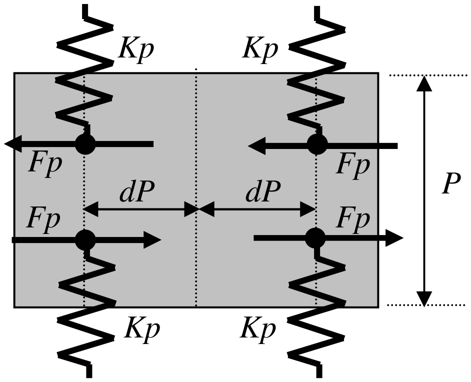

dP = Distance between center of moving platform and connected position of planar linkage
P = Distance between front and rear planar linkages
Fp = Force induced by misalignment of planar linkage
Ks = Spring constant of planar linkage

Figure 3.20 Undesirable loading in planar linkage

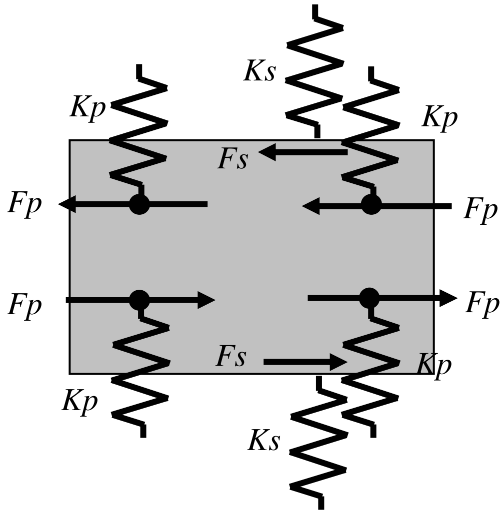

Figure 3.21 Undesirable loading in total system

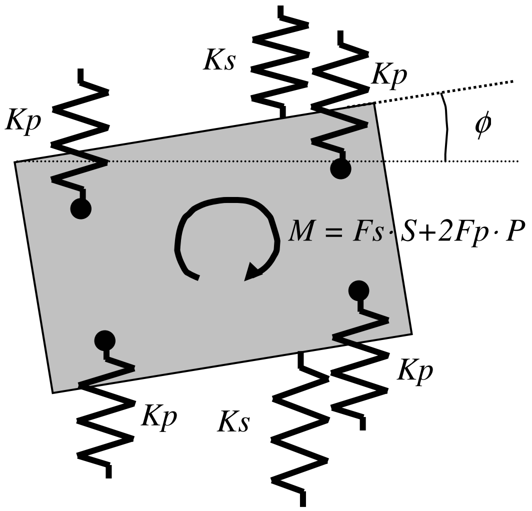

Figure 3.22 Resulting moment and deformation from undesirable loading

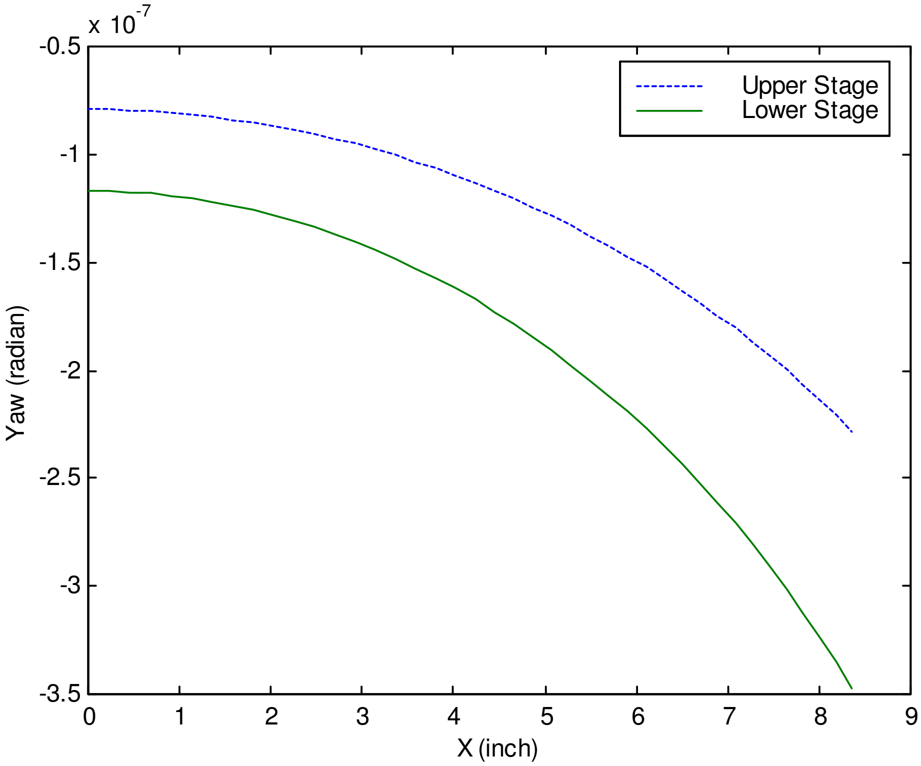

Figure 3.23 Calculated result of yaw error of XY stage

Chapter 4: Dynamics Analysis and Control

4.1 DYNAMIC MODELING

Figure 4.1 shows a notch type rectilinear spring with two added side linkages. The equation of motion can be derived by using Lagrange's equation. For a single degree of freedom system, Lagrange's equation can be expressed by

$$\frac{d}{dt}\left(\frac{\partial T}{\partial \dot{x}}\right)-\frac{\partial T}{\partial x}+\frac{\partial V}{\partial x}=F_x \tag{4.1}$$

where T is the kinetic energy, V the potential energy, x the displacement, and F_x is the external force.

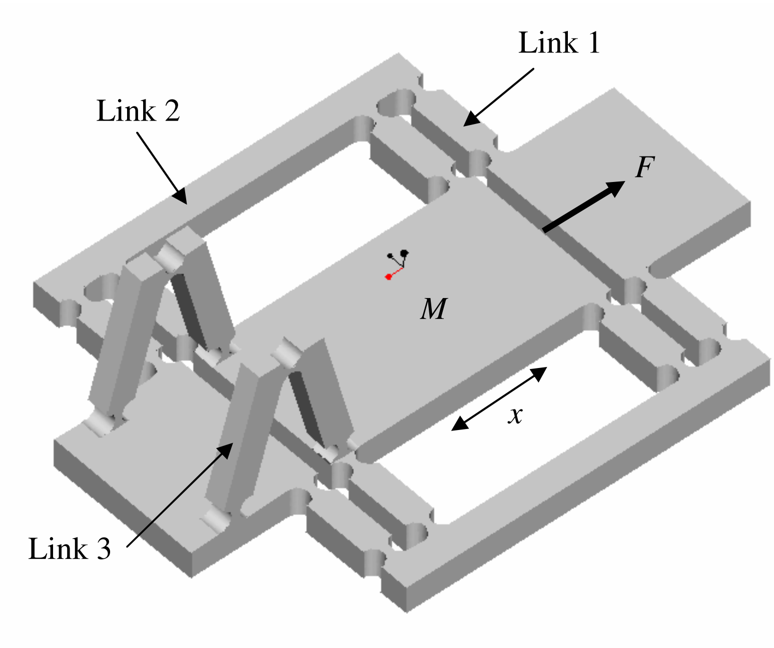

Figure 4.1 Notch type rectilinear spring with two added side linkages

The kinetic and potential energy of the mechanism are given by

$$T = \frac{1}{2}M\dot{x}^2 + 2\frac{1}{2}m_2(\frac{\dot{x}}{2})^2 + 4\frac{1}{2}m_1(\frac{\dot{x}}{4})^2 + 4\frac{1}{2}m_1(\frac{\dot{x}+\frac{\dot{x}}{2}}{2})^2 + 8\frac{1}{2}I_1(\frac{\dot{x}}{2L_1})^2$$

$$+ 2\frac{1}{2}m_3(\frac{\dot{x}}{4})^2 + 2\frac{1}{2}m_3(\frac{\dot{x}+\frac{\dot{x}}{2}}{2})^2 + 4\frac{1}{2}I_3(\frac{\dot{x}}{2L_3})^2$$

$$= \frac{1}{2}(M + \frac{m_2}{2} + \frac{5m_1}{2} + \frac{2I_1}{L_1^{\,2}} + \frac{5m_3}{4} + \frac{I_3}{L_3^{\,2}})\dot{x}^2 \tag{4.2}$$

$$V = 16\frac{1}{2}k(\frac{x}{2L_1})^2 + 4\frac{1}{2}k(\frac{x}{2L_3})^2 + 2\frac{1}{2}k(\frac{x}{L_3})^2 \tag{4.3}$$

where I_i, m_i, and L_i (i=1,2,3) are the moment of inertia, the mass, and the length of the link i, and k is the torsional spring constant of the flexure joint.

Substituting Equations (4.2) and (4.3) into Lagrange's equation gives the equation of motion

$$(M + \frac{m_2}{2} + \frac{5m_1}{2} + \frac{2I_1}{L_1^{\,2}} + \frac{5m_3}{4} + \frac{I_3}{L_3^{\,2}})\ddot{x} + (\frac{4}{L_1^{\,2}} + \frac{3}{L_3^{\,2}})kx = F_{\mathbf{x}} \tag{4.4}$$

Because in the proposed XY stage the flexure joints are installed in the off-nominal position, these forces should be included in the external force term. The external force term can be written by

$$F_x = F + \frac{8k\theta_{10}}{L_1} + \frac{6k\theta_{30}}{L_3} \tag{4.5}$$

where F is the real external force, θ_{10} is the deflected angle of link 1 in Figure 4.1 when the flexure joints are installed in the planar linkage, and θ_{30} is the difference between the rotated angle of the side link in the installation position and that in nominal position as shown in Figure 4.2.

$$\theta_{30} = \theta_{3a} - \theta_{3b} \tag{4.6}$$

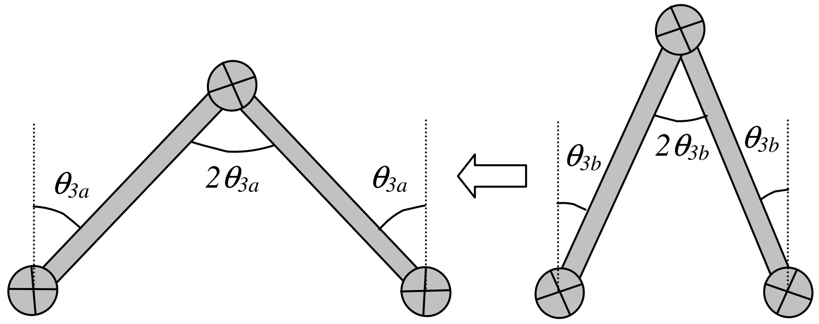

Where the flexure joints are installed
(Zero deflection in flexure joints)

Nominal Position

Figure 4.2 Schematic explaining definition of θ_{30}

Since this system has nonlinear behavior in the off-nominal position, it is difficult to derive the equation of motion. However, in Equation (4.4) the mass term can be assumed to be constant in the off-nominal configuration, because other mass terms are very small compared to the mass of the moving platform as shown in Table 4.1. Figure 4.3 shows the stage in the off-nominal configuration (the side linkage are not shown).

Table 4.1 Comparison of mass terms

Stage	**M**	**Sum of other masses**	**Ratio**
Upper Stage	0.0852	0.0128	6.66
Lower Stage	0.2439	0.0128	19.05

The potential energy term in the off-nominal position can be expressed by

$$V = 16 \cdot \frac{1}{2} k(\theta_1 - \theta_{10})^2 + 4 \cdot \frac{1}{2} k(\theta_3 - \theta_{30})^2 + 2 \cdot \frac{1}{2} k(2\theta_3 - 2\theta_{30})^2 \tag{4.5}$$

where θ_1 is the rotated angle of the link in the planar linkage and θ_3 is that in the side linkage. The derivative of the potential energy with respect to the position (x) is

$$\frac{dV}{dx} = 16k(\theta_1 - \theta_{10})\frac{d\theta_1}{dx} + 12k(\theta_3 - \theta_{30})\frac{d\theta_3}{dx} \tag{4.6}$$

Since $\frac{d\theta_1}{dx} = \frac{1}{2L_1 cos\theta_1}$ and $\frac{d\theta_3}{dx} = \frac{1}{2L_3 cos\theta_3}$,

$$\frac{dV}{dx} = 16k(\theta_1 - \theta_{10})\frac{1}{2L_1 cos\theta_1} + 12k(\theta_3 - \theta_{30})\frac{1}{2L_3 cos\theta_3} \tag{4.7}$$

Since $\theta_1 = sin^{-1}\dfrac{x}{2L_1}$ and $\theta_3 = sin^{-1}\dfrac{x}{2L_3}$,

$$\frac{dV}{dx} = k\left[\left(sin^{-1}\frac{x}{2L_1} - \theta_{10}\right)\frac{16}{x\sqrt{4{L_1}^2 - x^2}} + \left(sin^{-1}\frac{x}{2L_3} - \theta_{30}\right)\frac{12}{x\sqrt{4{L_3}^2 - x^2}}\right]x \tag{4.8}$$

Substituting Equation (4.8) into Lagrange's equation, the simplified equation of motion for off-nominal configuration can be written by

$$(M + \frac{m_2}{2} + \frac{5m_1}{2} + \frac{2I_1}{{L_1}^2} + \frac{5m_3}{4} + \frac{I_3}{{L_3}^2}) \cdot \ddot{x} + k \cdot f(x) \cdot x = F_x \tag{4.9}$$

where $F_x = F$,

$$f(x) = \left[\left(sin^{-1}\frac{x}{2L_1} - \theta_{10}\right)\frac{16}{x\sqrt{4{L_1}^2 - x^2}} + \left(sin^{-1}\frac{x}{2L_3} - \theta_{30}\right)\frac{12}{x\sqrt{4{L_3}^2 - x^2}}\right]$$

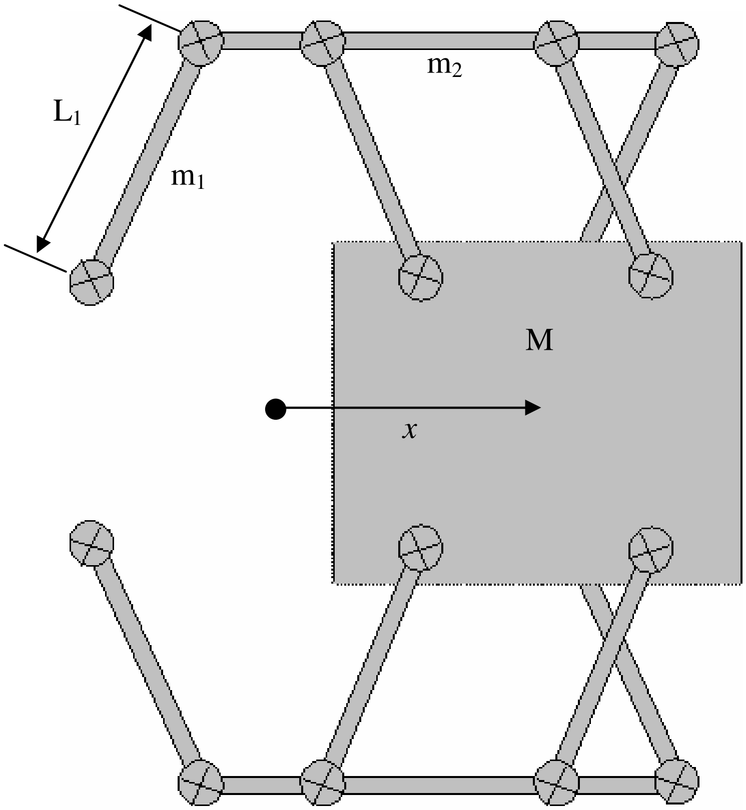

Figure 4.3 Moving stage in off-nominal position

4.2 MODAL ANALYSIS

The proposed XY stage is an overlapped-type XY stage such that the Y axis stage is installed on the X axis stage. With overlapped-type XY stages, the natural frequency of the X axis (or Y axis) stage along the Y axis (or X axis) should be larger than the bandwidth of the Y axis (or X axis) stage. The structural design of the XY stage is very important to achieve fast operation.

Several assumptions are made before calculation to simplify the analysis. The side linkages are responsible for the stiffness in the lateral direction because the planar linkages allow the stage to move freely in the Y direction. All compliant components can be modeled as simple linear springs. All springs and masses in the system should be identified before calculating the natural frequency. The spring constants of the side links can be calculated by basic solid mechanics theory. In figure 2.17, the side links undergo only bending and the boundary condition is zero angles at both ends. The spring constant of the side link (*KLs*) is given by

$$KLs = \frac{F}{\delta} = \frac{12EI_s}{L_s{}^3} \tag{4.10}$$

where F is the external force, δ the corresponding deflection, E the Young's modulus, I_s the mass moment of inertia of the side link, and L_s is the length of the side link. The spring constant of the flexure joint can be found in the data sheet. The configuration of the total system is shown in Figure 4.4. Table 4.2 describes the parameters used in Figure 4.4.

Table 4.2 Parameters used in modal analysis

Parameters	**Description**
KAt	Tensile axial stiffness of single-ended flexure joint
KAc	Compression axial stiffness of single-ended flexure joint
KLs	Stiffness of side link for kinematic constraint
M	Mass of moving platform

The overall spring constant (K) and the natural frequency (ω) can be calculated as shown in Equation (4.11) and (4.12).

$$K = \frac{2 \cdot \dfrac{\frac{KAc}{3} \cdot KLs}{\frac{KAc}{3} + KLs} \cdot \dfrac{\frac{KAt}{3} \cdot KLs}{\frac{KAt}{3} + KLs}}{\dfrac{\frac{KAc}{3} \cdot KLs}{\frac{KAc}{3} + KLs} + \dfrac{\frac{KAt}{3} \cdot KLs}{\frac{KAt}{3} + KLs}} = \frac{\frac{KAc}{3} \cdot KLs}{\frac{KAc}{3} + KLs} \tag{4.11}$$

$$\omega = \sqrt{\frac{K}{M}} \tag{4.12}$$

The feedback control bandwidth from the calculated natural frequency can be given by

Feedback Control Bandwidth of X (Y) stage
= Natural Frequency of Y (X) stage / 4 (4.14)

In order to achieve higher natural frequency, several combinations of materials for the planar and side links are suggested. Table 4.3 summarizes all the results of the natural frequencies and control bandwidths for the links with different materials. Higher bandwidth can be achieved with the lower stage, so the lower stage is used as the X stage and the upper stage as the Y stage.

Table 4.3 Summary of natural frequency and bandwidth

Material for Links		**Natural Frequency**		**Control Bandwith**	
Upper Stage	Lower Stage	Upper Stage	Lower Stage	Upper Stage	Lower Stage
Al Alloy	**Al Alloy**	61	37	9.3	15.3
Stainless Steel	**Stainless Steel**	53	35	8.7	13.3
Al Alloy	**Stainless Steel**	61	43	10.7	15.3

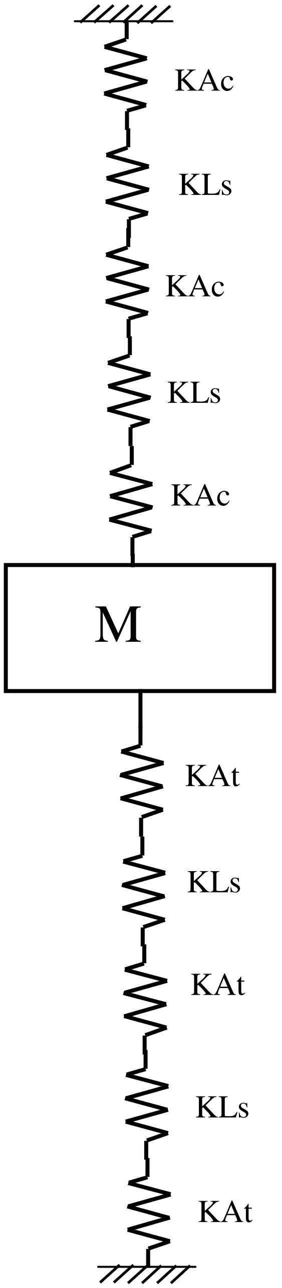

Figure 4.4 Complete model for modal analysis

4.3 CONTROL

From Equation (4.9), the relationship between position and force in the static situation is shown in Figure 4.5. The flexure based linkage guide behaves as a nonlinear spring, but its behavior is very close to a linear spring. The linear spring constant is 1.05 lbf/in that can be approximated from the curve.

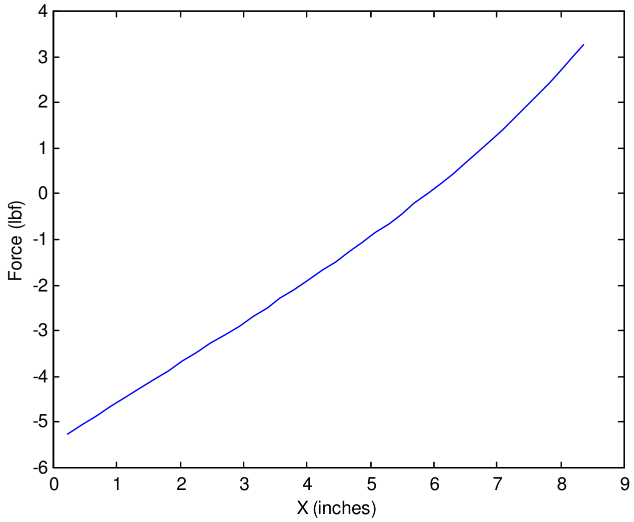

Figure 4.5 Relationship between Force and Position

The stage dynamics can be simplified as a simple spring and mass model. The transfer function of the stage including the linear motor and the flexure stage is given by

$$\mathbf{G}(\mathbf{s}) = \frac{33.3}{7\mathbf{s}^2 + 10\mathbf{s} + 306.6} \tag{4.15}$$

The SIMULINK model including PID controller for the stage is depicted in Figure 4.6. The transfer function of the flexure stage contains a pair of complex-conjugate poles that lie close to the imaginary axis in the s-plane. This results in an undesirable closed-loop system that is unstable or only lightly damped. Since this kind of system only allows small gain increase, there is large overshoot, long settling time, and large steady-state error. One way to control this system is to design a controller with zeros near the undesirable, lightly-damped poles of the plant. These zeros can attenuate the effect of these poles. The poles of the controller can then be placed in a more desirable position. Such a controller is called a notch filter. But it is difficult to obtain exact pole/zero cancellation due to uncertainty of the system.

Most motion controller manufacturers recommend their users to use a sampling period as small as possible for better performance. Because the flexure stage dynamics does not allow even a very small integral gain, it is necessary to use a larger sampling period to include an appropriate integral gain.

Figure 4.7 shows the schematic for the control hardware of the stage. The BLM-203-A linear motor manufactured by Aerotech Inc. is used as an actuator to move the stage. The BA20-160 amplifier produced by the same company generates input power into the linear motor. The Agilent 10889B servo axis board is employed as the motion controller to send the control signal to the amplifier. A digital PID control algorithm is employed to control the position of the stage.

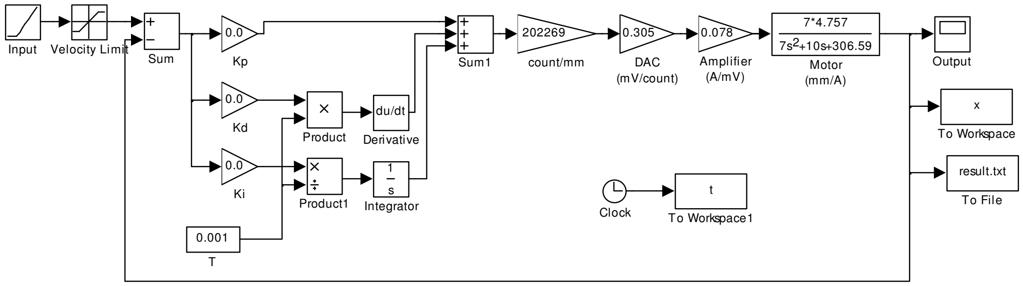

Figure 4.6 Simulink Model with PID Controller

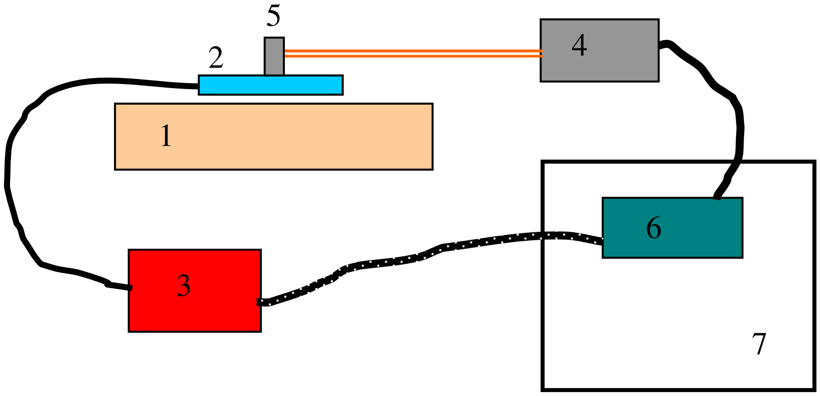

1. Linear Motor (Magnet Track)
2. Linear Motor (Moving Coil)
3. Amplifier
4. Laser Interferometer
5. Measurement Mirror
6. Motion Control Board
7. Host Computer

Figure 4.7 Schematic for motion control parts of stage

The linear motor testbed is fabricated to perform the control test before installing the linear motor into the X stage. The linear springs are installed to include the dynamic behavior of the actual stage. Figure 4.8 shows the solid model of the linear motor testbed.

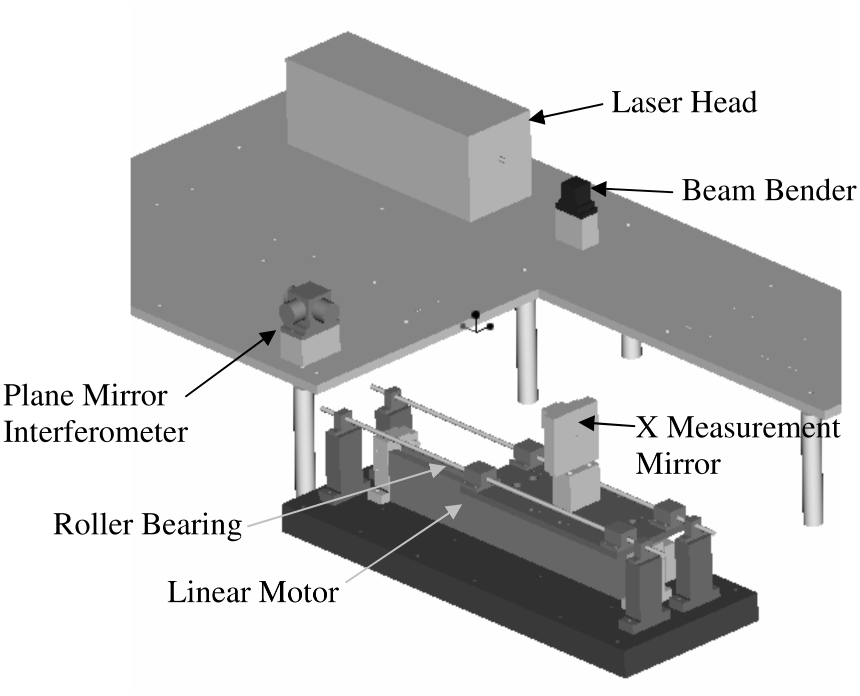

Figure 4.8 Linear motor testbed

Figure 4.9 shows a continuous step positioning of the linear motor testbed. A 10 mm step is repeated five times and a 50 mm displacement is obtained overall. The standard deviation of the X position is around 170~300 nm. Figure 4.10 represents the same test results with 10 micron stepwise input. The standard deviation of the X position is about 35~72 nm.

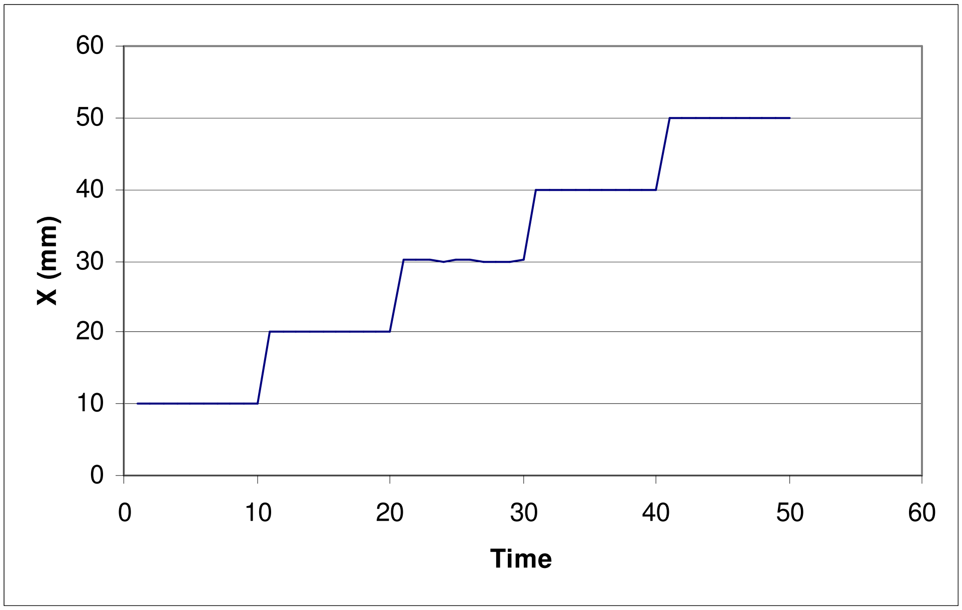

Figure 4.9 Control test result of the linear motor testbed with 10 mm step input

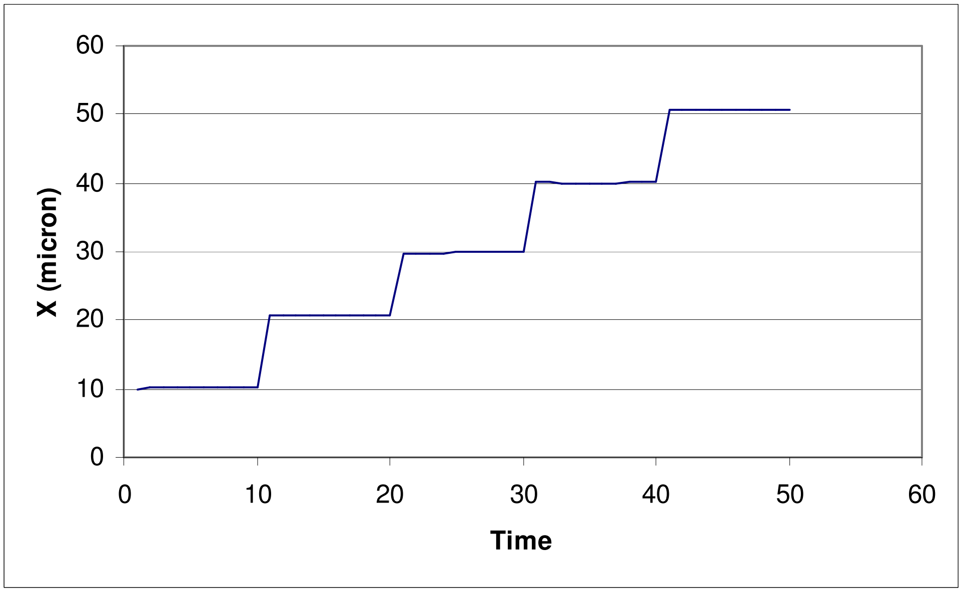

Figure 4.10 Control test result of the linear motor testbed with 10 μm step input

A single-axis motion stage is fabricated to verify the control performance of the proposed flexure stage experimentally. The photograph of the fabricated motion stage is shown in Figure 4.11 as well as the close up view of linkages is in Figure 4.12. The linear motor installed in the stage is shown in Figure 4.13. A digital PID control algorithm is employed to control the position of the stage. Although the motion stage can move kinematically up to 200mm, the controller tuning is optimized up to 100mm. The control test results and discussions are described in Chapter 5.

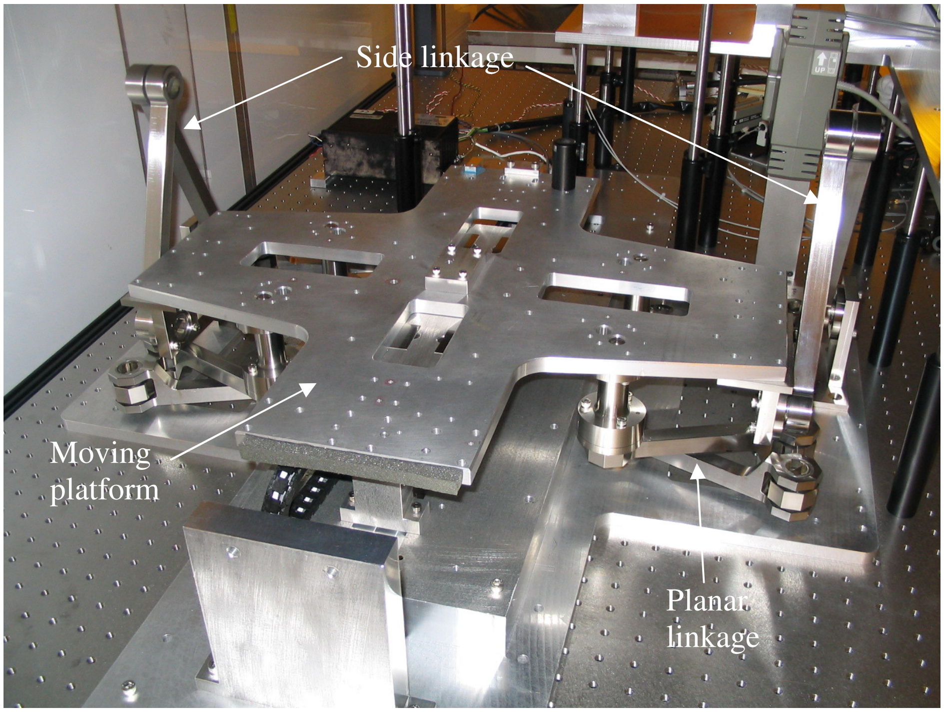

Figure 4.11 Photograph of the fabricated motion stage

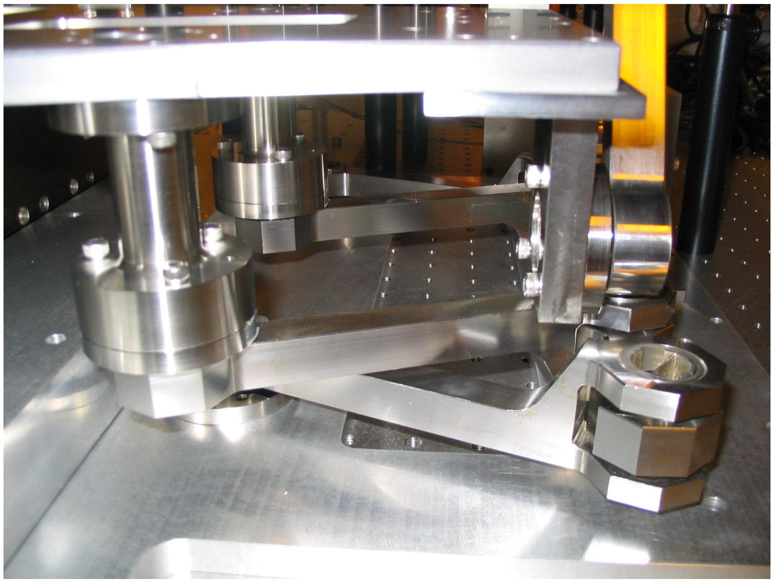

Figure 4.12 Close up view of linkages

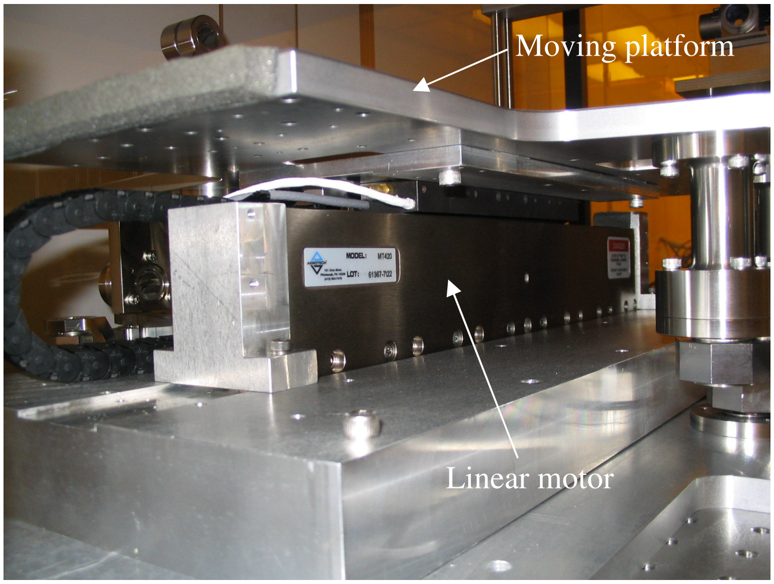

Figure 4.13 Linear motor installed in the stage

Chapter 5: Experimental Results and Discussion

5.1 MOTION ERRORS

Figure 5.1 depicts the motion errors in a single axis linear motion carriage. An ideal single-axis motion stage should give only motion in the X direction, but an actual linear motion stage has three translational and three rotational errors, such as X axis servo error (δ_x), horizontal straightness error (δ_y), vertical deflection (δ_z) error, roll (θ_x), yaw (θ_y), and pitch (θ_z) [Slocum, 1992]. Since the proposed stage is symmetric about the X axis, roll is less significant than yaw and pitch. Horizontal straightness error, vertical deflection error, yaw, and pitch are observed experimentally by using laser interferometers.

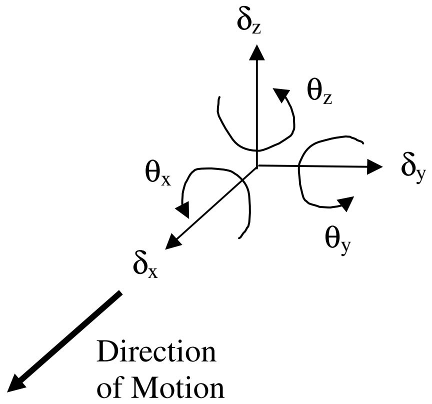

Figure 5.1 Motion errors in a single axis linear motion carriage

In the measurement setup, the horizontal straightness error and yaw can be measured simultaneously by using two laser interferometers (Y1 and Y2) parallel to the Y axis. The horizontal straightness error can be obtained from Y1 or Y2, or as an average of y1 & y2. The yaw error of the stage can be calculated by dividing the difference between the two straightness errors by the distance (D) between the two laser beams (see Figure 5.2). Similarly, the vertical deflection error and pitch can be measured simultaneously by using two laser interferometers (Z1 and Z2) parallel to the Z axis. The yaw and pitch are given by

$$\theta_z = \tan^{-1}\left(\frac{Y2 - Y1}{D}\right) \quad \text{and} \quad \theta_y = \tan^{-1}\left(\frac{Z2 - Z1}{D}\right) \tag{5.1}$$

When a stage moves in the travel direction, any Y and Z direction movements are undesirable. If this undesirable motion is repeatable, a lookup table can eliminate such errors. If not, it is necessary to do a complicated coordinated control of the two stages which is more difficult to be implemented in real-time at high bandwidths. Five kinds of tests are performed with the test setup: horizontal straightness test, horizontal straightness repeatability test, vertical deflection test, vertical deflection repeatability test, and modal test.

5.2 HORIZONTAL STRAIGHTNESS, YAW, AND REPEATABILITY

5.2.1 Test Setup

Figure 5.2 shows the schematic of the laser interferometer setup for the horizontal straightness & yaw tests. The Agilent 5517C laser head generates a coherent, collimated, light beam consisting of two orthogonally polarized frequency components. The wavelength of light from the laser head is used as the length standard for the laser interferometer measurement system. Three beam splitters and one beam bender are implemented to distribute light into the appropriate directions. Two Agilent 10706A plane mirror interferometers are utilized to measure the Y-axis movement. One Agilent 10706B high stability plane mirror interferometer is used to measure the X-axis position for control purposes. Three laser receivers are used: one for the X-axis control and two for the Y-axis measurements. The signal from the X-axis receiver is sent to the Agilent 10889B servo axis board installed in the host computer. The 10889B board measures the X-axis position and sends a control signal to the amplifier to reposition the linear motor. The other two receivers are connected to two Agilent 10885A PC axis boards that only read the Y-axis positions.

Figure 5.3 illustrates a solid model of the experimental setup for the horizontal straightness & yaw test. Figure 5.4 shows the corresponding photograph of the horizontal straightness and yaw test setup.

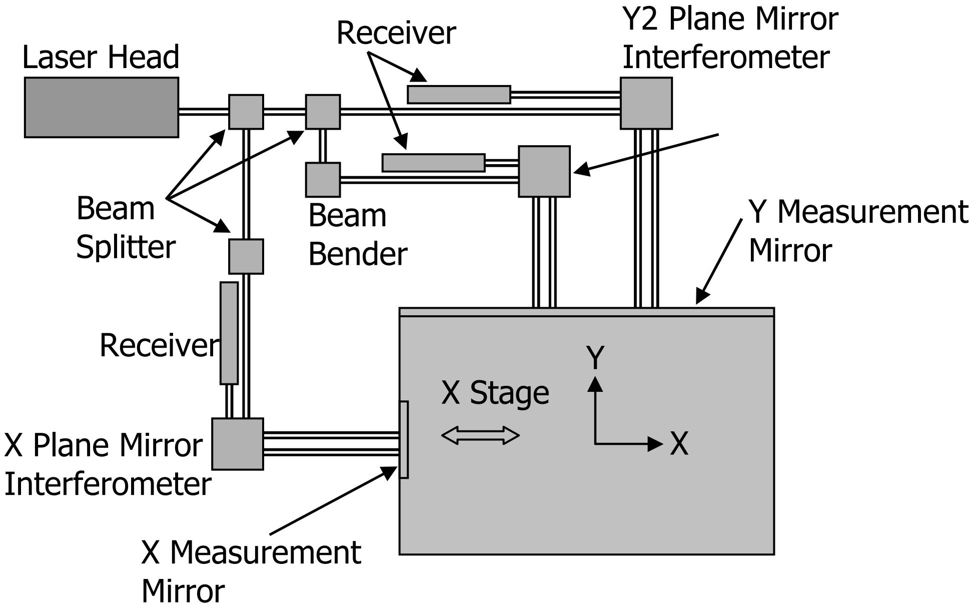

Figure 5.2 Schematic of laser interferometer setup for horizontal straightness test

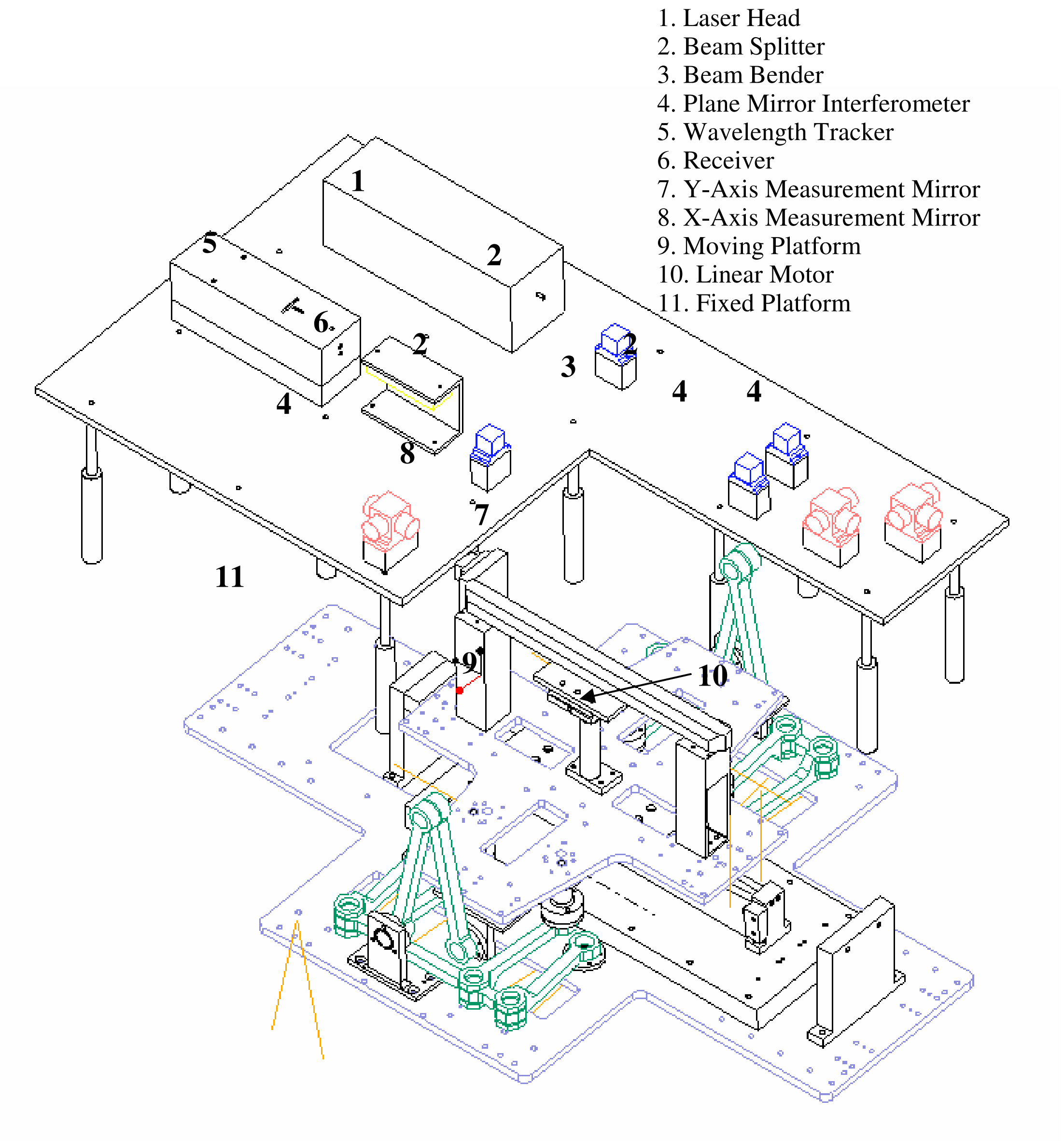

1. Laser Head
2. Beam Splitter
3. Beam Bender
4. Plane Mirror Interferometer
5. Wavelength Tracker
6. Receiver
7. Y-Axis Measurement Mirror
8. X-Axis Measurement Mirror
9. Moving Platform
10. Linear Motor
11. Fixed Platform

Figure 5.3 Solid model of experimental setup for horizontal straightness test

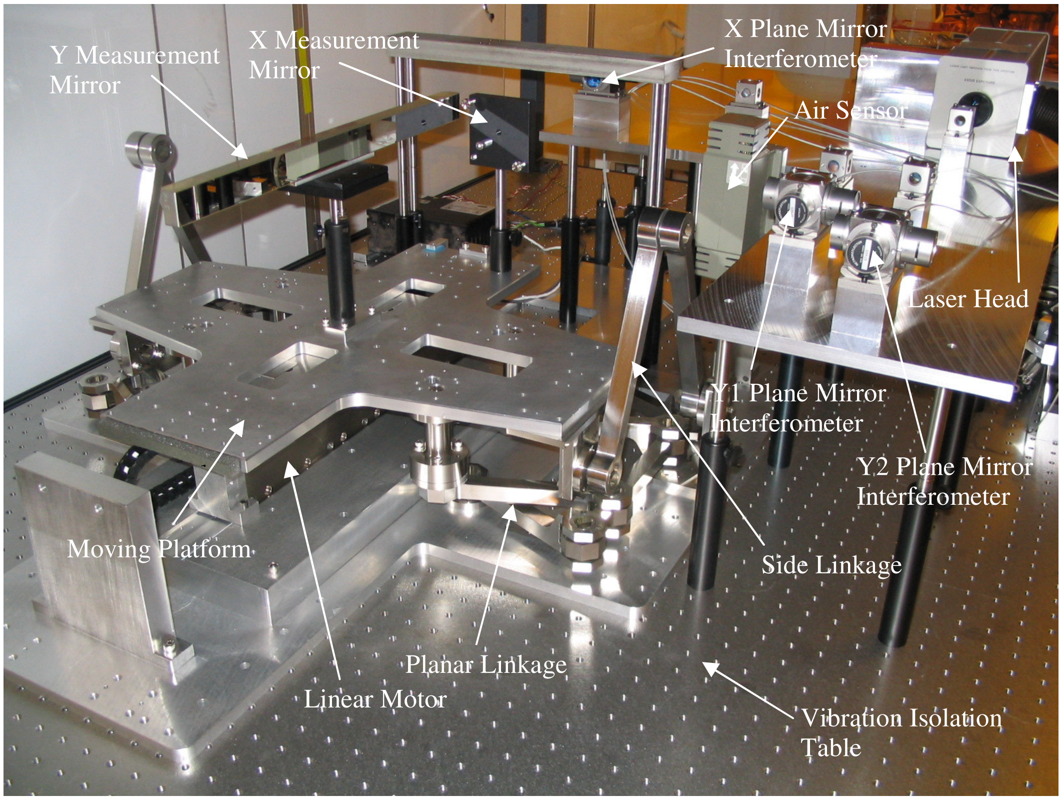

Figure 5.4 Photograph of horizontal straightness test setup

5.2.2 Horizontal Straightness Test Result

As the stage is moved step-by-step at the increment of 10 mm for a distance of 100 mm, for 3 runs, the lateral displacements (Y1 and Y2) at each step are measured using the laser interferometer. Figure 5.5 shows the straightness test results. Figure 5.6 represents the corresponding straightness errors which are obtained by subtracting the lateral displacements from the least-square fitting line. The straightness error results show very repeatable behavior. Figure 5.7 shows the measured values of the yaw of the stage.

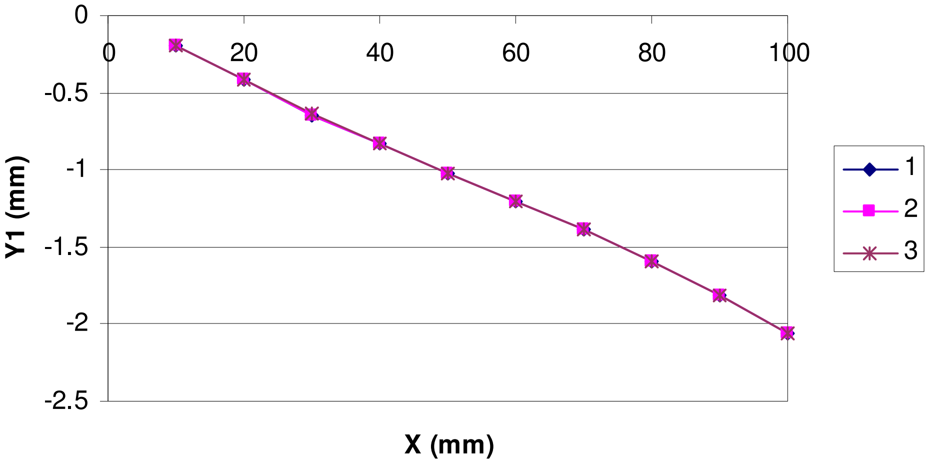

(a) Test result – Y1

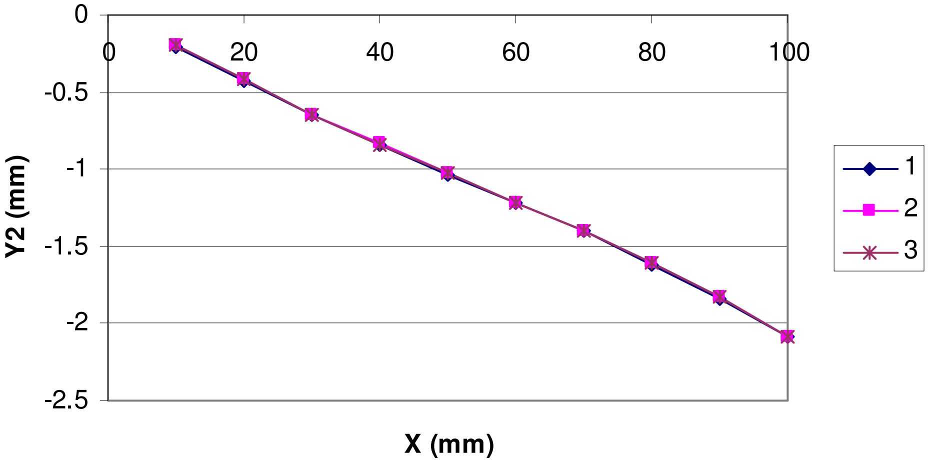

(b) Test result – Y2

Figure 5.5 Horizontal straightness test result

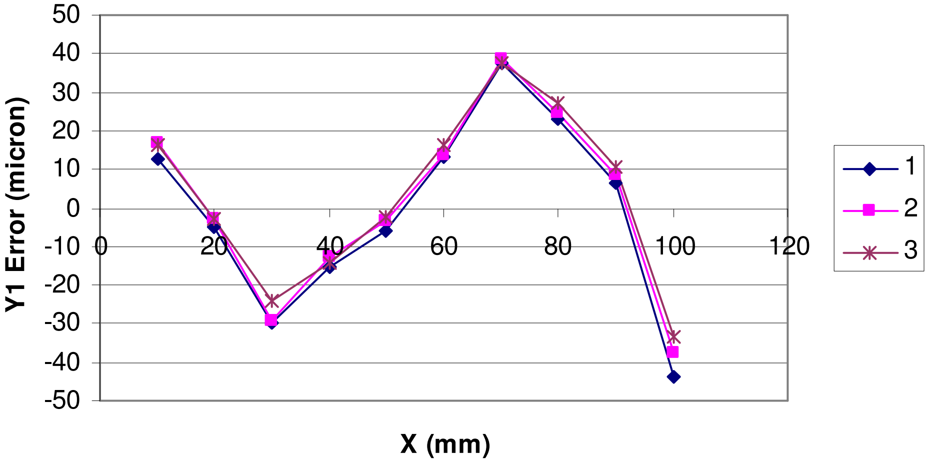

(a) Y1 straightness error

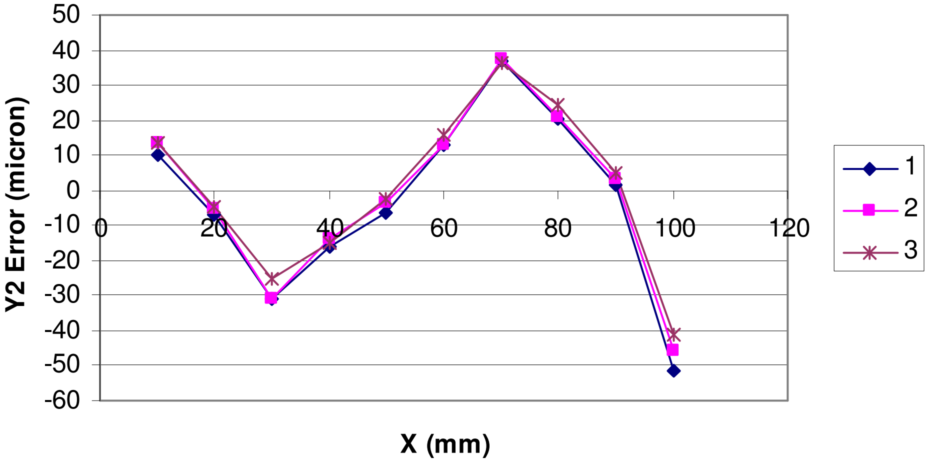

(b) Y2 straightness error

Figure 5.6 Straightness error test result

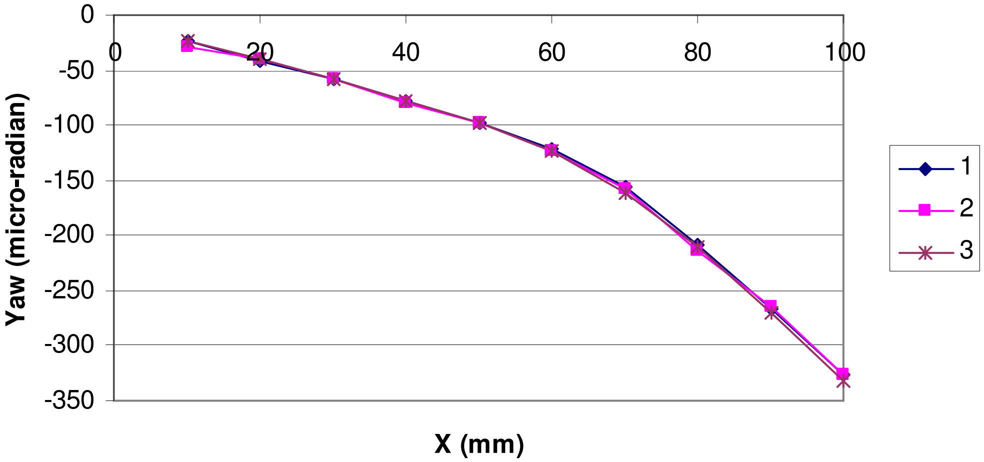

Figure 5.7 Yaw motion error test result

5.2.3 Repeatability Test

The repeatability of the horizontal straightness of the stage is also examined. Moving the stage forward and backward twenty times, the Y axis displacements at 50 mm from the home position are measured. Figure 5.8 shows the repeatability test results of the horizontal straightness and Figure 5.9 is the yaw repeatability test result. The standard deviation (σ) is about 1.29 micron for Y1, 1.30 micron for Y2, and 1.5 μ-radian for yaw. The repeatability (3σ) of the horizontal straightness of the stage is about 3.9 micron, but the stage shows a very excellent yaw repeatability of 4.5 μ-radian.

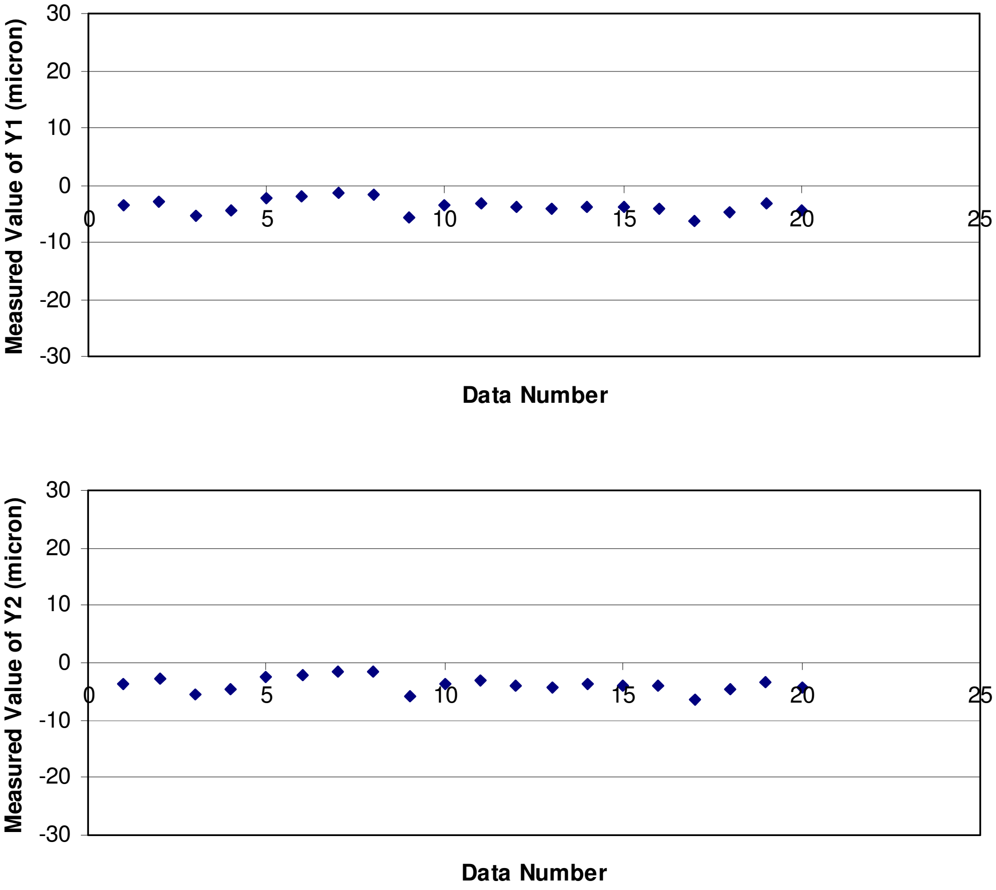

Figure 5.8 Horizontal straightness repeatability test results

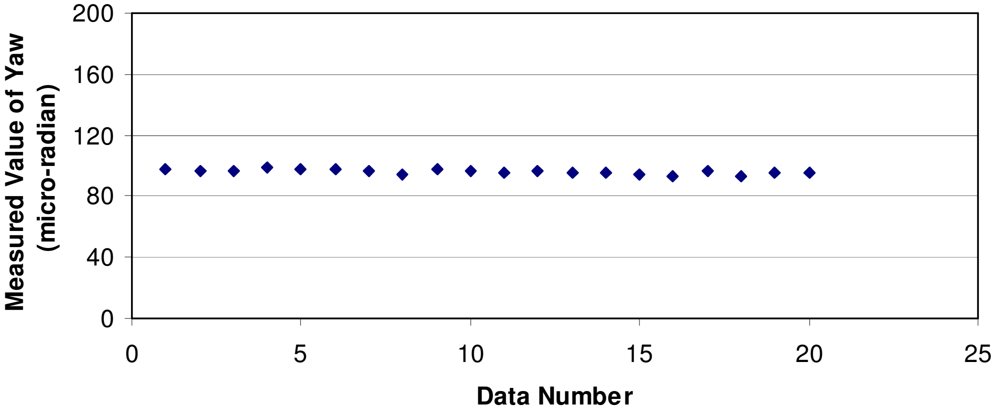

Figure 5.9 Yaw repeatability test result

5.2.4 Discussions and Suggestions

The major reason for relatively large straightness repeatability error compared to the commercial air bearing stages (less than 0.5 micron) is low lateral stiffness of the current flexure stage in the Y direction. The lateral stiffness range of typical air bearings is on the order of 100 N/micron, and that of the flexure stage around 1.2 N/micron. Additional dummy side linkages should be attached to increase this stiffness. In order to obtain the stiffness comparable to that of typical air bearing stage, around 83 side linkages need to be used, which makes it impractical.

A stack of buckled strips can be used to increase the lateral stiffness of the stage as shown in Figure 5.10. According to beam buckling theory, if the compression load reaches the critical load, the stiffness of the column drops quickly and allows a lot of displacement in that direction. The post buckling behavior of wide thin plates can be incorporated to achieve a high lateral stiffness while still allowing large displacement in the moving direction.

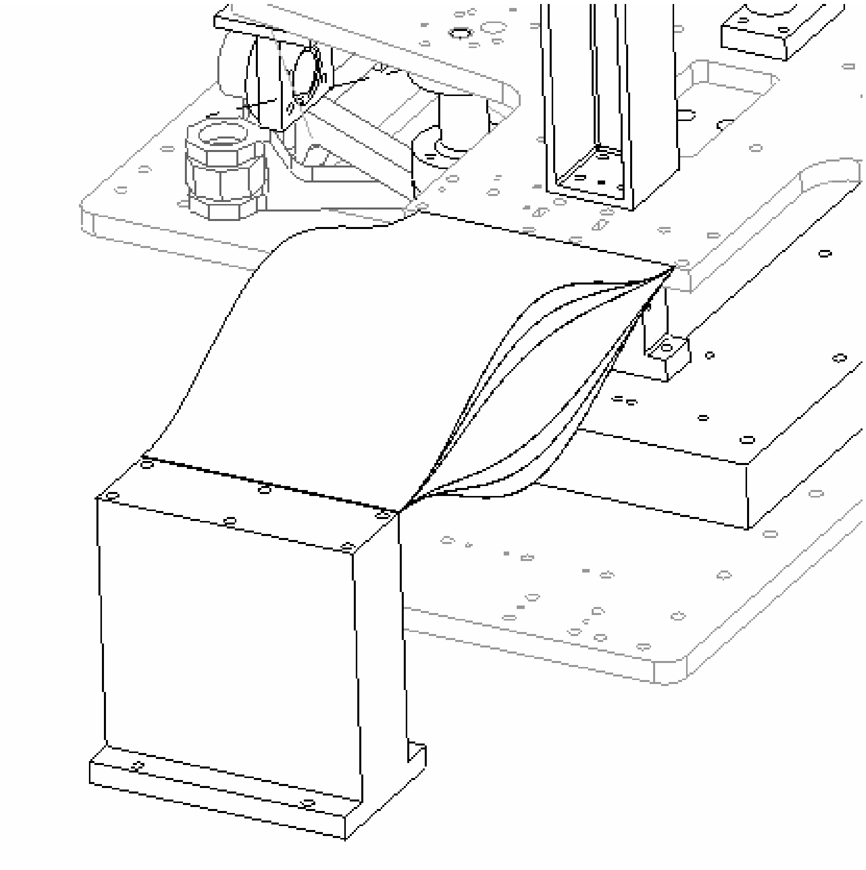

Figure 5.10 Buckled strip installed in the stage

The buckled strips are installed in the stage, but there was a difficulty in achieving control stability. However, since the repeatability error depends on the position reading noise, the Y positions are measured with or without buckled strips when the stage is stationary at zero position. Figure 5.11 shows the Y position reading test results for three cases. Table 5.1 shows the lateral stiffness of each case and the standard deviations of test results. Figure 5.12 shows the plot of Table 5.1. As the lateral stiffness increases, the position noise level decreases rapidly. This result supports the hypothesis that the low lateral stiffness is the main reason for large straightness repeatability error.

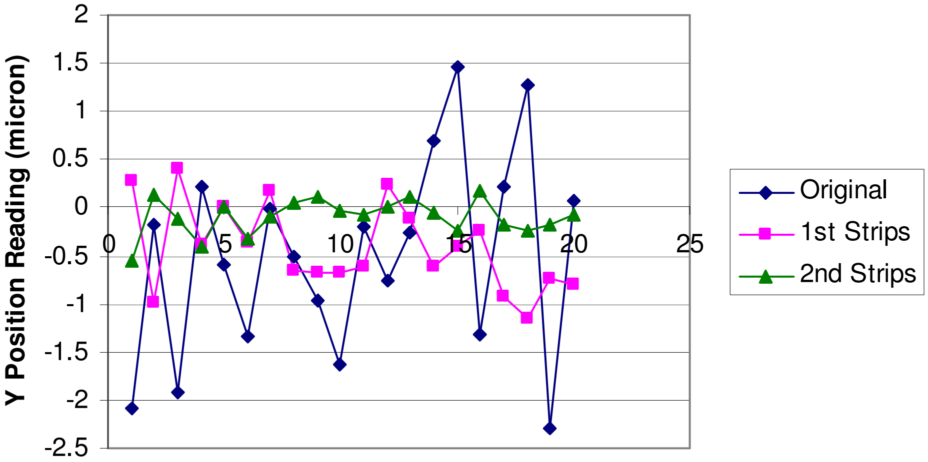

Figure 5.11 Y Position reading with or without buckled strips

Table 5.1 Lateral position reading test results with and without buckled strips

	Lateral Stiffness (N/micron)	Standard Deviation of Position Reading (micron)
Original System	1.2	1.0505
With 1st Buckled Strips	4.5	0.4519
With 2nd Buckled Strips	16	0.1899

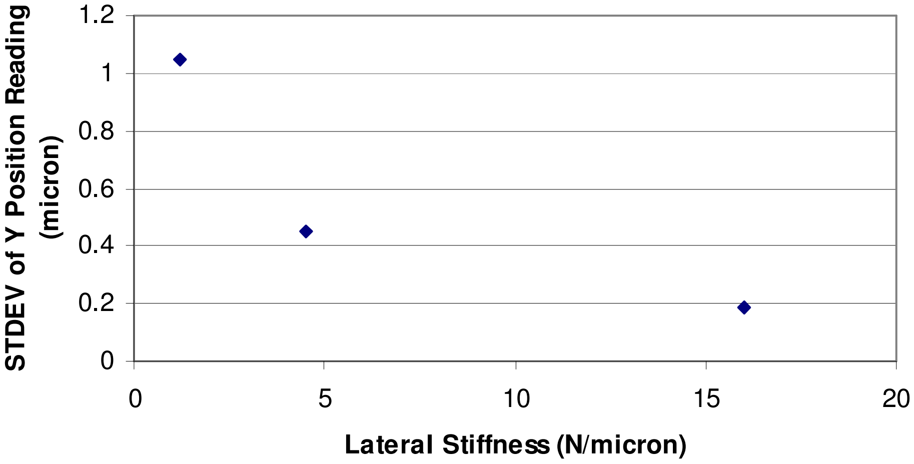

Figure 5.12 Plot of Table 5.1

Since the vibration isolation table absorbs mostly the high frequency disturbances, the magnitude of the position noise depends on the DC gain of the system as given by

$$\mathbf{DC\_gain} = \left|\frac{1}{\mathbf{ms}^2 + \mathbf{k}}\right| = \frac{1}{\mathbf{k}} \tag{5.2}$$

Obviously the DC gain of the system transfer function decreases as the lateral stiffness increases. Figure 5.13 demonstrates the position fluctuation analytically by applying a random noise to the system with or without buckled strips. The magnitude of the random signal was selected based on the experimental results.

After adding the sensor noise (100 nm) to the standard deviation of the analytical results, the analytical result showed similar trends with the experimental results as shown in Figure 5.14.

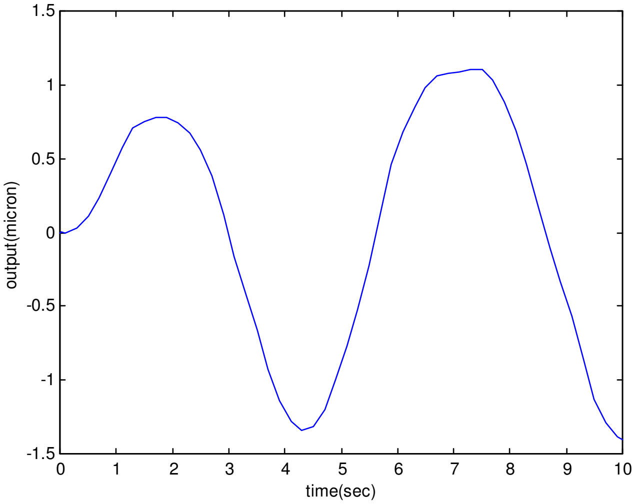

(a) Original system

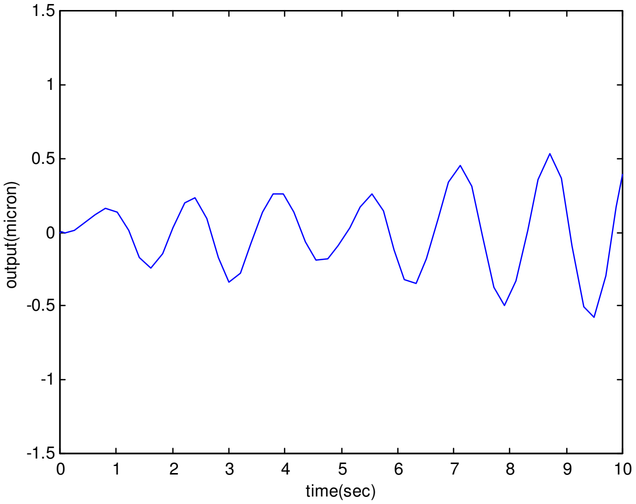

(b) With 2nd buckled strips

Figure 5.13 Simulation of position fluctuation by noise

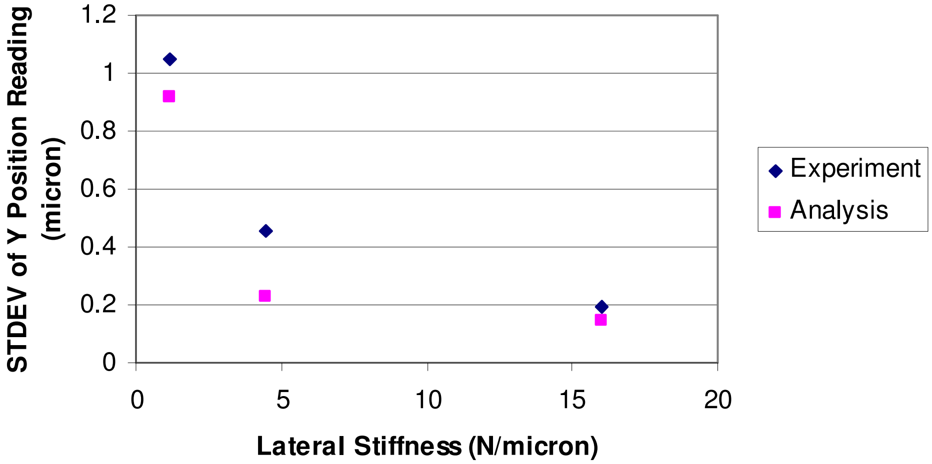

Figure 5.14 Position reading versus lateral stiffness

If the Peaucellier linkages as shown in Figure 5.15 are employed instead of the current linkages, the stiffness can be increased in more efficient way. Figure 5.16 shows the schematic of the new stage design using 6 Peaucellier linkages. The stage including 16 Peaucellier linkages can make the same order of the lateral stiffness of the typical air bearing stage. Table 5.2 shows the calculated lateral stiffness for several different configurations. The stiffness analysis is assumed that the radial stiffness of the flexure is constant and does not change with rotation angle.

Table 5.2 Stiffness for different configurations

	Stiffness (N/um)	**Number of Flexures**	**(Range of motion) /√(Foot Print Area)**
Original System	1.2	6	0.27
With 5 Side Linkage	6.0	12	0.27
With 50 Side Linkage	60	120	0.02
With 83 Side Linkage	100	1200	0.005
4 Peaucellier linkage	22	28	0.17
6 Peaucellier linkage	35	50	0.12
12 Peaucellier linkage	70	100	0.12
16 Peaucellier linkage	100	130	0.098
Typical Air Bearing	100	-	0.33

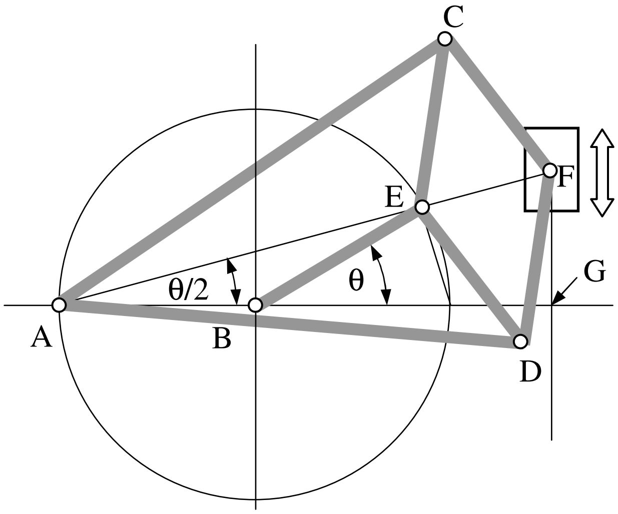

|AB|=|BE|, |AC|=|AD|, and |CE|=|ED|=|DF|=|FC|.

Figure 5.15 Design concept using Peaucellier linkage

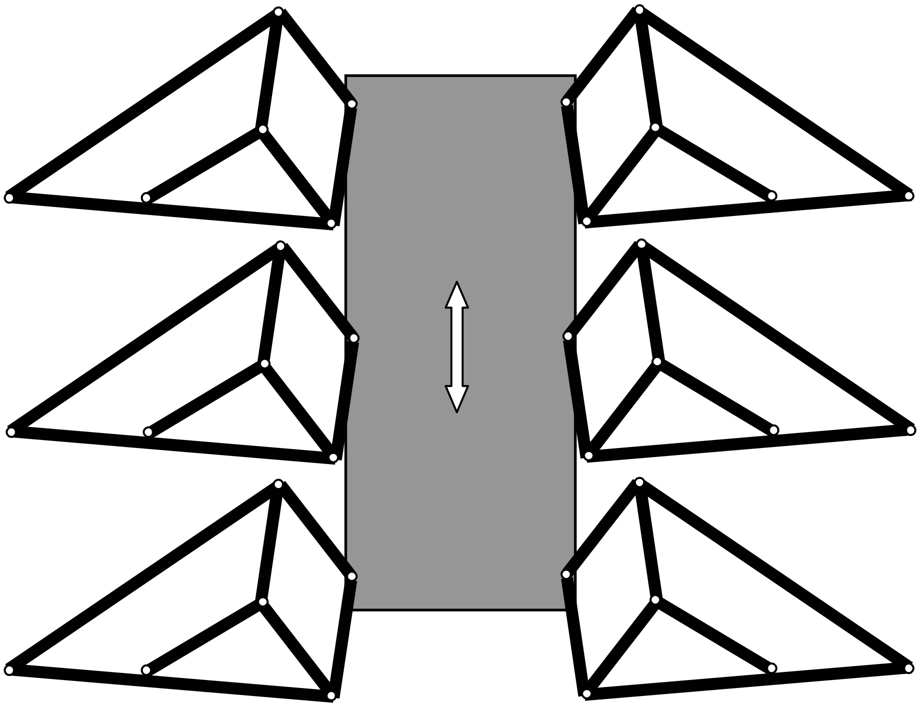

Figure 5.16 New Stage Design Using 6 Peaucellier linkage

5.3 VERTICAL DEFLECTION, PITCH AND REPEATABILITY

5.3.1 Test Setup

Figure 5.17 represents the solid model of the vertical deflection & roll test. The general idea is the same as the horizontal straightness & yaw test. Figure 5.18 represents the corresponding photograph of the vertical deflection and pitch test setup.

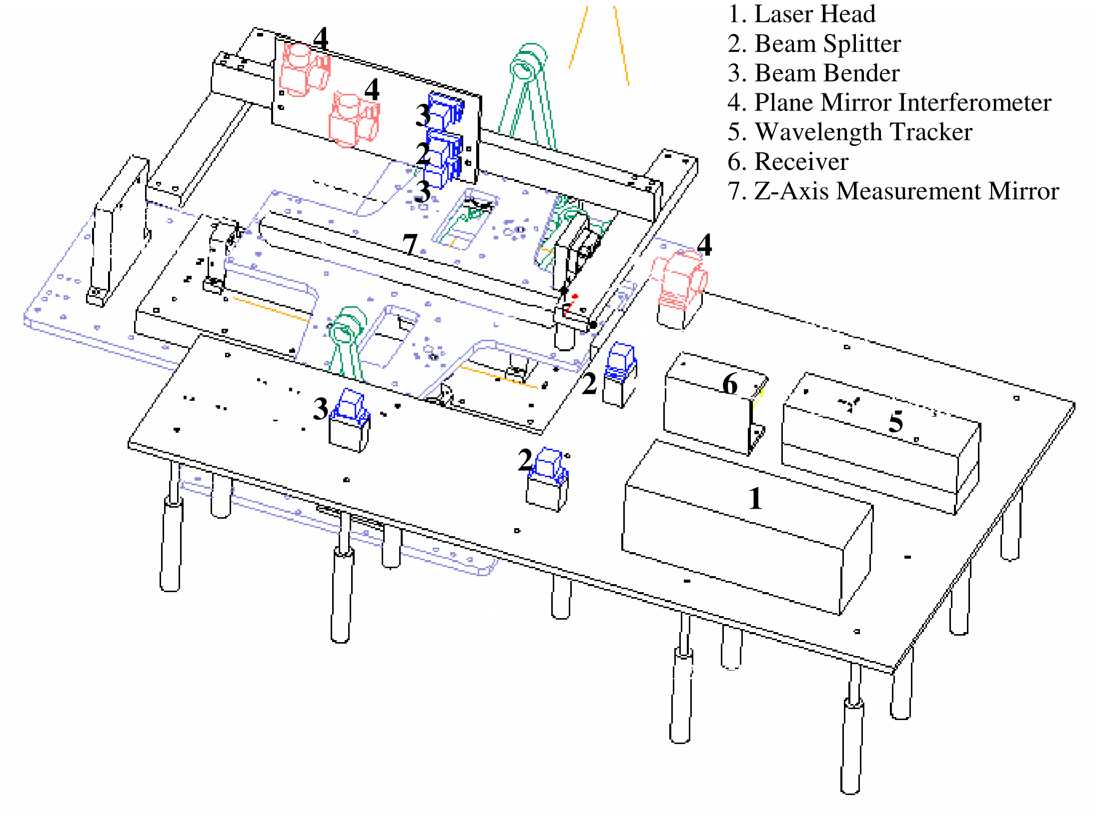

Figure 5.17 Solid model of experimental setup for vertical deflection test

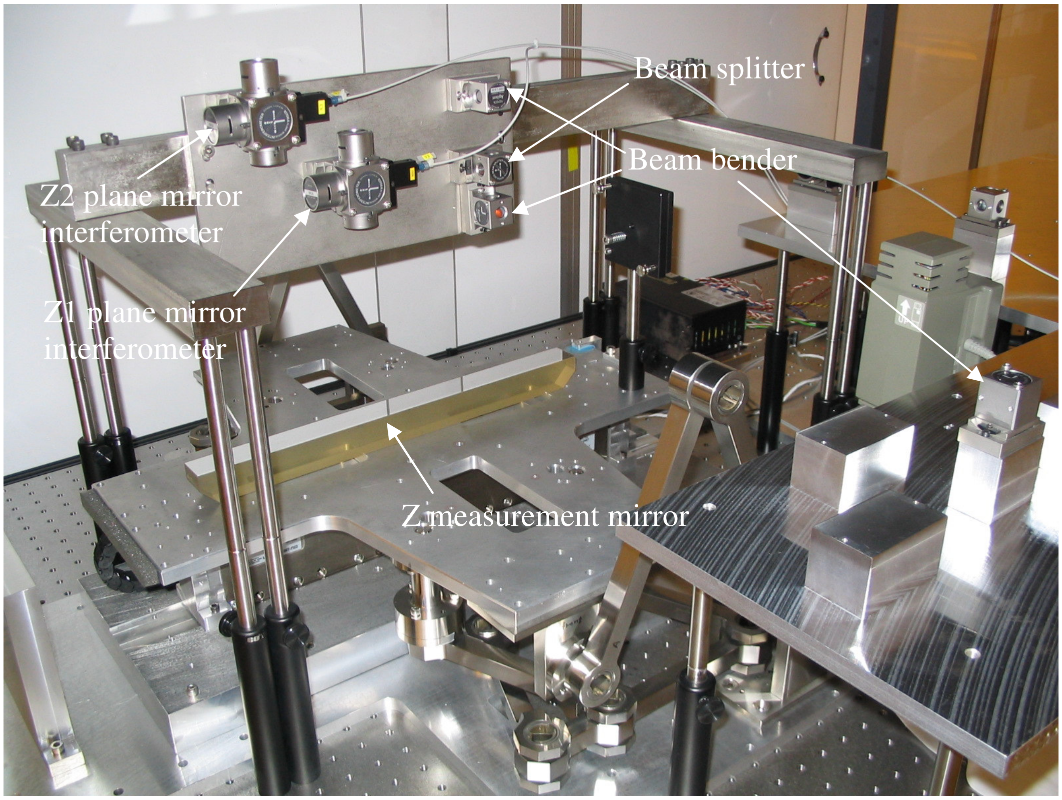

Figure 5.18 Photograph of vertical deflection test setup

5.3.2 Vertical Deflection Test Results

The vertical deflection of the motion stage is also examined because large deflections may require a vertical stage for compensation. On the other hand, if this motion stage is used in a XYZ 3 DOF stage, the existing Z stage compensates these deflections. Test procedures are similar to that for the horizontal straightness test.

As the stage is moved step-by-step at the increment of 10 mm for a distance of 100 mm, for 3 runs, the vertical displacements (Z1 and Z2) at each step are measured using the laser interferometer. Figure 5.19 shows the vertical deflection test results. The stage showed the maximum error of about 0.6 mm at the position where the flexures are installed. It is greater than the analytical results because the axial stiffness of the flexure joints was very low in the experiment. Since these errors are large but repeatable, it can be compensated by a Z stage. Figure 5.20 represents the pitch motion error of the stage.

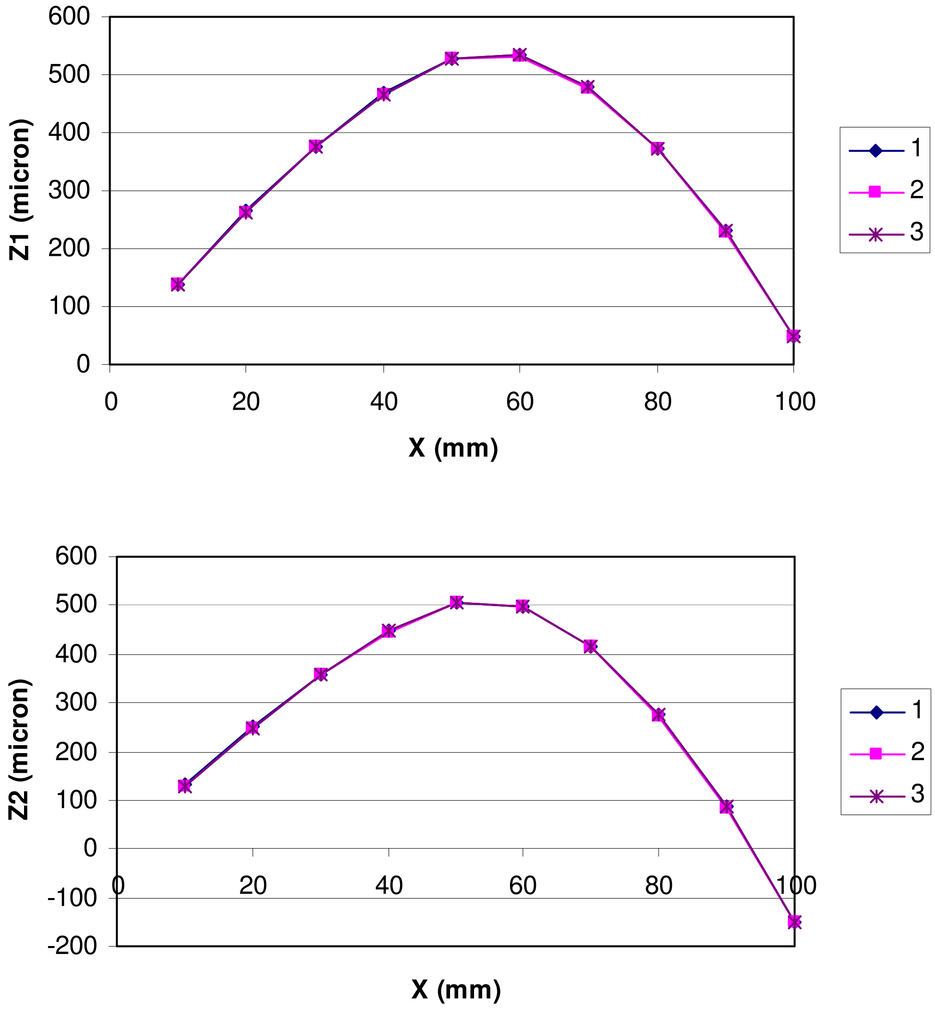

Figure 5.19 Vertical deflection test result

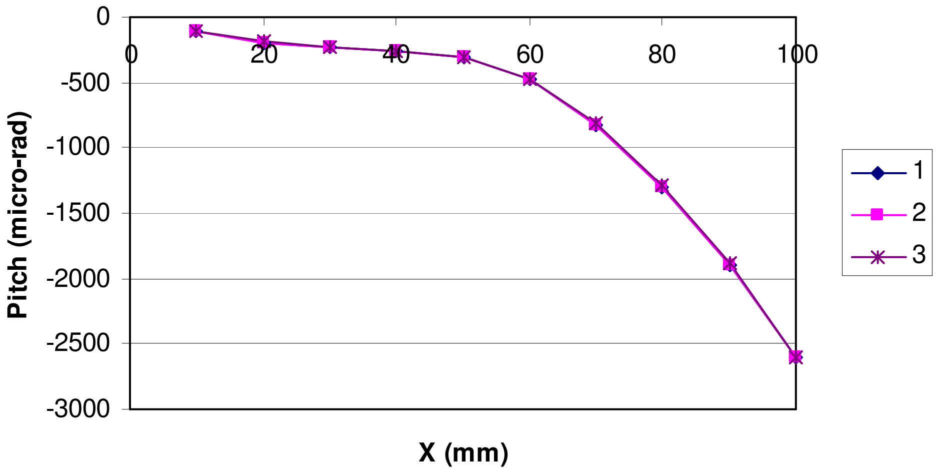

Figure 5.20 Pitch error test result

5.3.3 Repeatability Test Results

The repeatability of the vertical deflection of the stage is also examined. Moving the stage forward and backward twenty times, the Z axis displacements at 50 mm from the home position are measured. Figure 5.21 shows the repeatability test results of Z1 and Z2, and Figure 5.22 is the pitch repeatability test result. The standard deviation (σ) is about 0.22 micron for Z1, 0.28 micron for Z2, and 0.99 μ-radian for pitch. The repeatability of the vertical deflection of the motion stage is less than 0.84 micron (3σ) which is better than the horizontal case, because the stage has higher vertical stiffness.

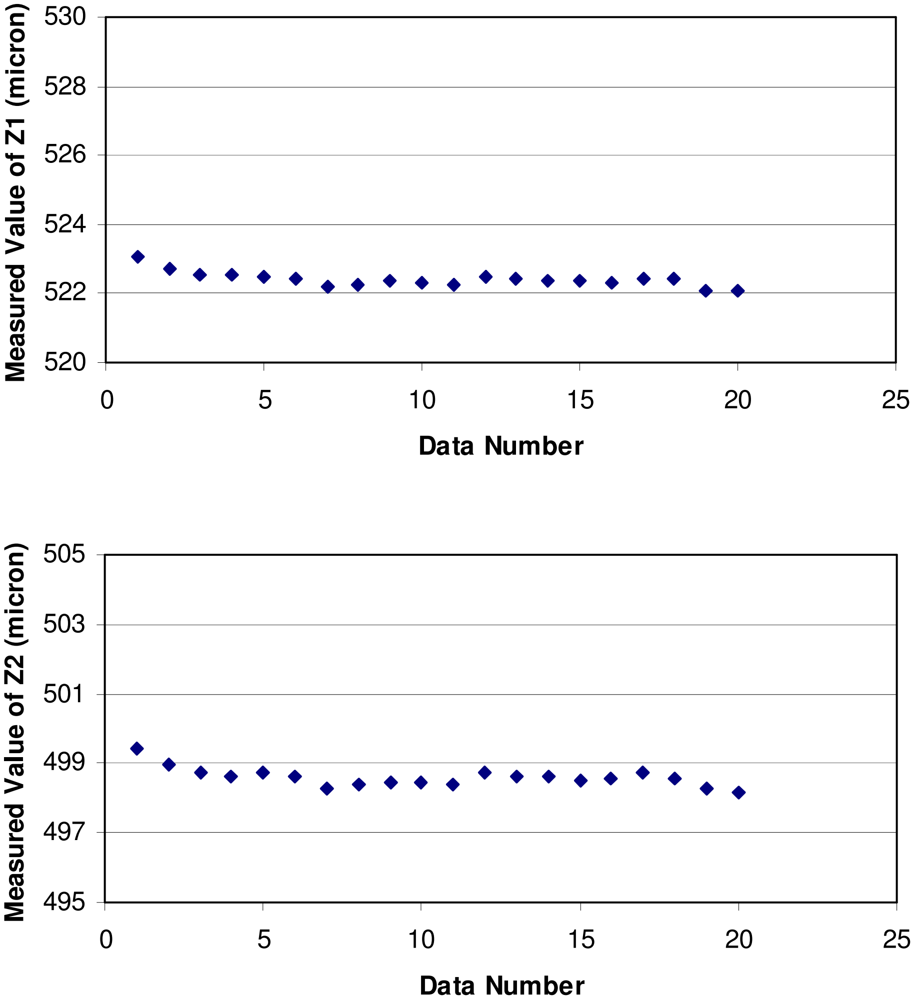

Figure 5.21 Vertical deflection repeatability test result

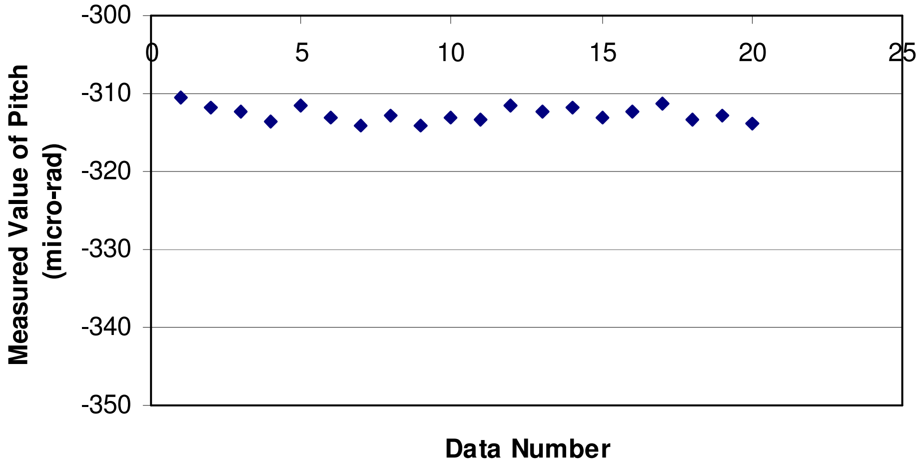

Figure 5.22 Pitch repeatability test result

5.3.4 Discussions and Suggestions

The repeatability of the vertical deflection of the motion stage is better than the horizontal case. Especially the stage shows very excellent repeatability of the pitch error. In order to increase the repeatability of the vertical deflection, the vertical stiffness of the stage needs to be increased as suggested in the horizontal straightness repeatability test. Obviously using more planar linkages will increase the vertical stiffness.

In order to minimize the current vertical deflection error of the stage, the flexures need to be installed at the end position of the stage since the vertical deflection is maximum at the position where the flexures are installed. These will change the vertical deflection to increase (or decrease) monotonically. Also the superposition of the planar linkages is suggested as depicted in Figure 5.23. Since two planar linkages operate symmetrically and reversely, the total vertical deflection error remains very low through the motion range as described in Figure 5.24. If the vertical deflection can be below some level, an additional translation stage to compensate the vertical deflection is not required.

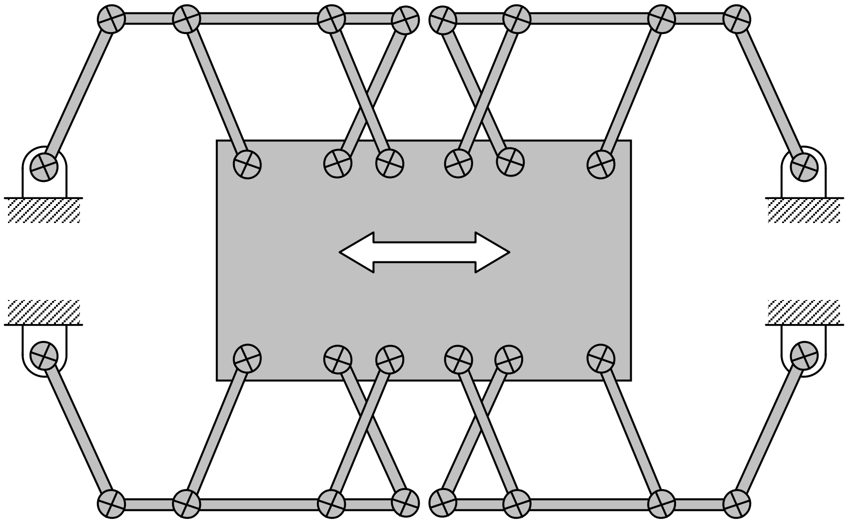

Figure 5.23 Mechanism to eliminate vertical deflection error

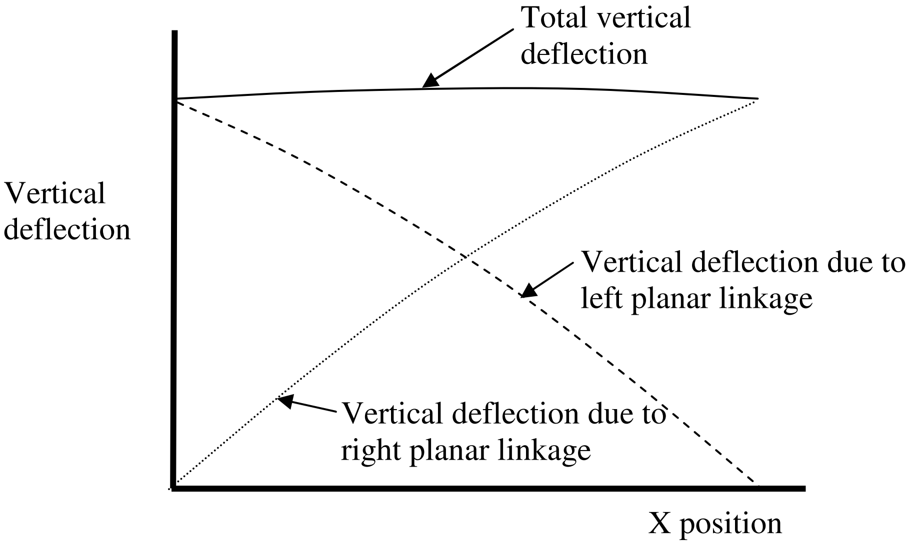

Figure 5.24 Cancellation of vertical deflection error

5.4 MODAL TEST

5.4.1 Experimental Procedures and Setup

Impact tests are performed to identify the resonant frequencies in the lateral and vertical direction. Figure 5.25 portrays the schematic of the modal test. An impulsive force by using an impact hammer is applied to the moving platform to the lateral direction and then to the vertical direction. The power supply provides a constant current to the amplifier. The supply current and voltage are 2 mA and 15 volts, respectively. JAE-5V accelerometers made by Japan Aviation Electronics Industry Ltd are used to measure the resulting transient response. Figure 5.26 shows the photograph of the accelerometer installed on the moving platform. Two accelerometers are installed in the lateral and vertical direction. Fast Fourier Transform is used to find the resonant frequencies of the motion stage.

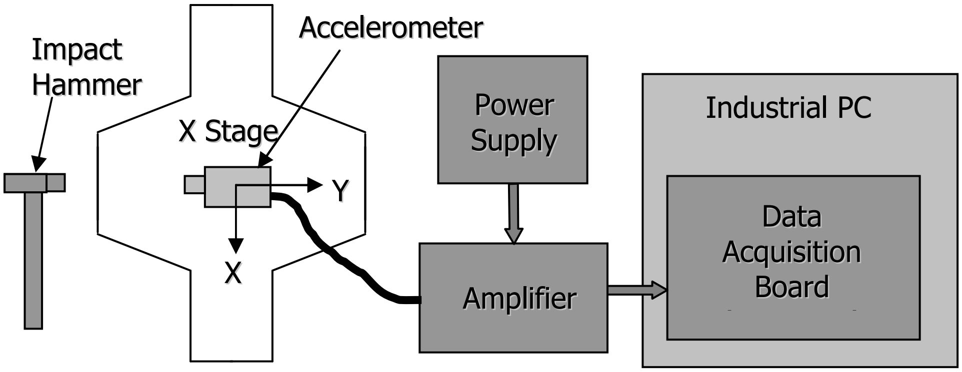

Figure 5.25 Schematic of modal test setup

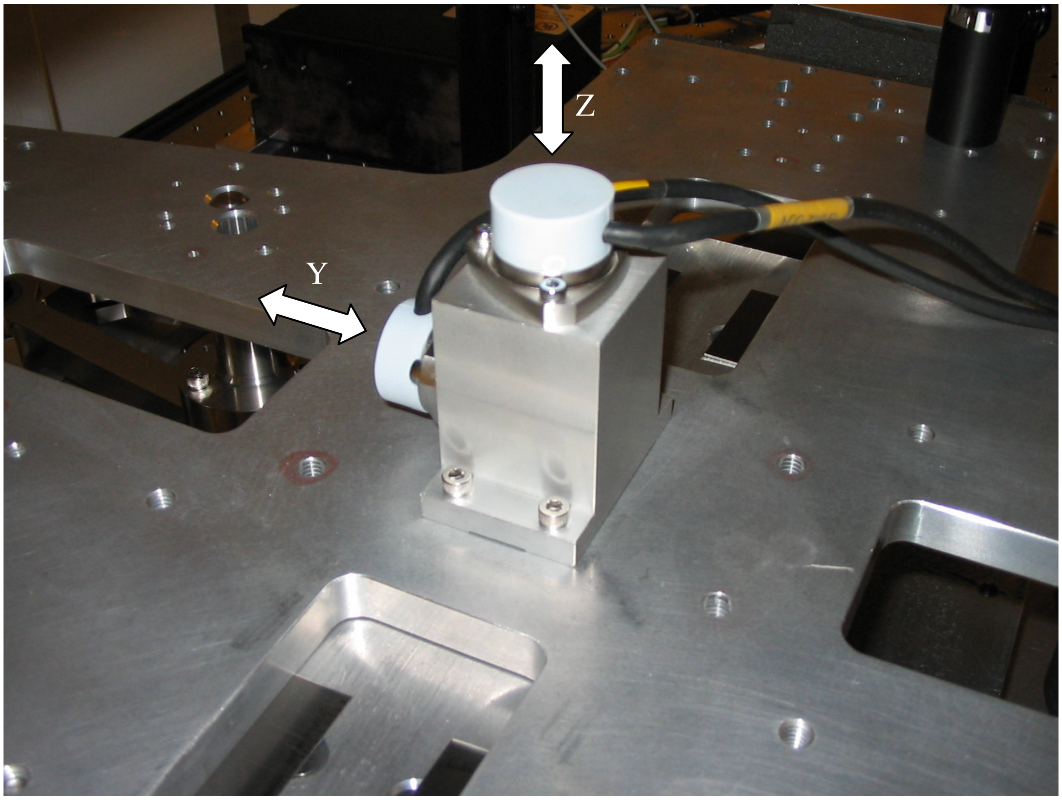

Figure 5.26 Photograph of the accelerometer installed on moving platform

5.4.2 Results and Discussions

Figure 5.27 illustrates the test results of the accelerometer signal and the frequency spectrum in the lateral direction of the test setup. The experimental natural frequency in the lateral direction is 12.3 Hz. The lateral stiffness needs to be increased to improve the natural frequency, which is the same conclusion with the horizontal straightness repeatability test result. Figure 5.28 illustrates the test results of the accelerometer signal and the frequency spectrum in the vertical direction of the test setup. The experimental natural frequency in the vertical direction is 46.7 Hz. The natural frequency in the vertical direction is larger than that in the lateral direction. These caused better vertical deflection repeatability compared to horizontal straightness repeatability.

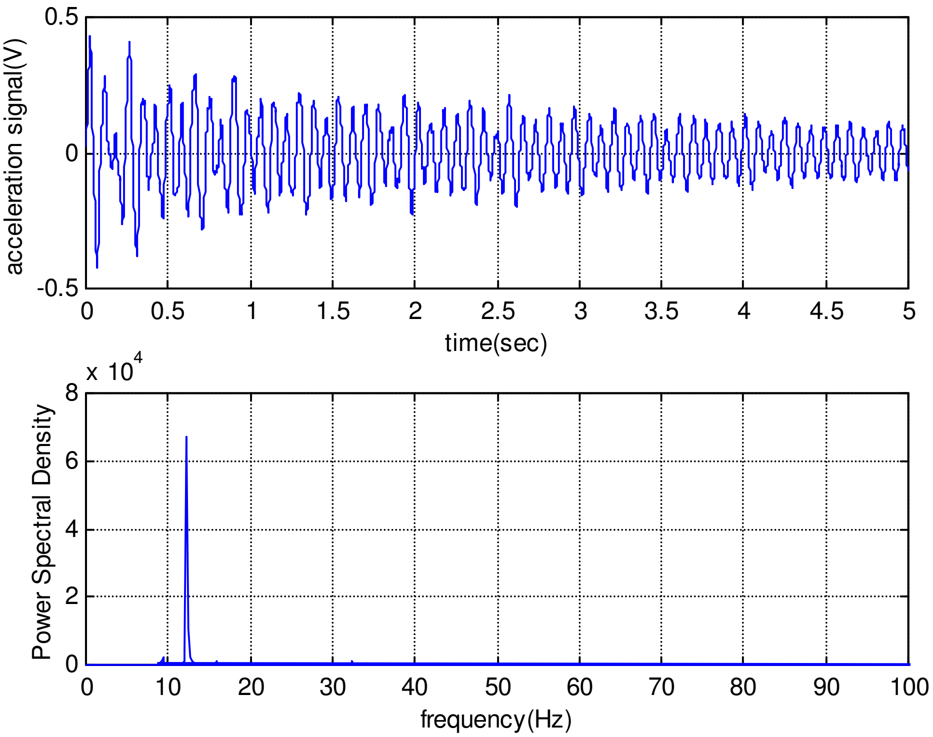

Figure 5.27 Lateral frequency response test result

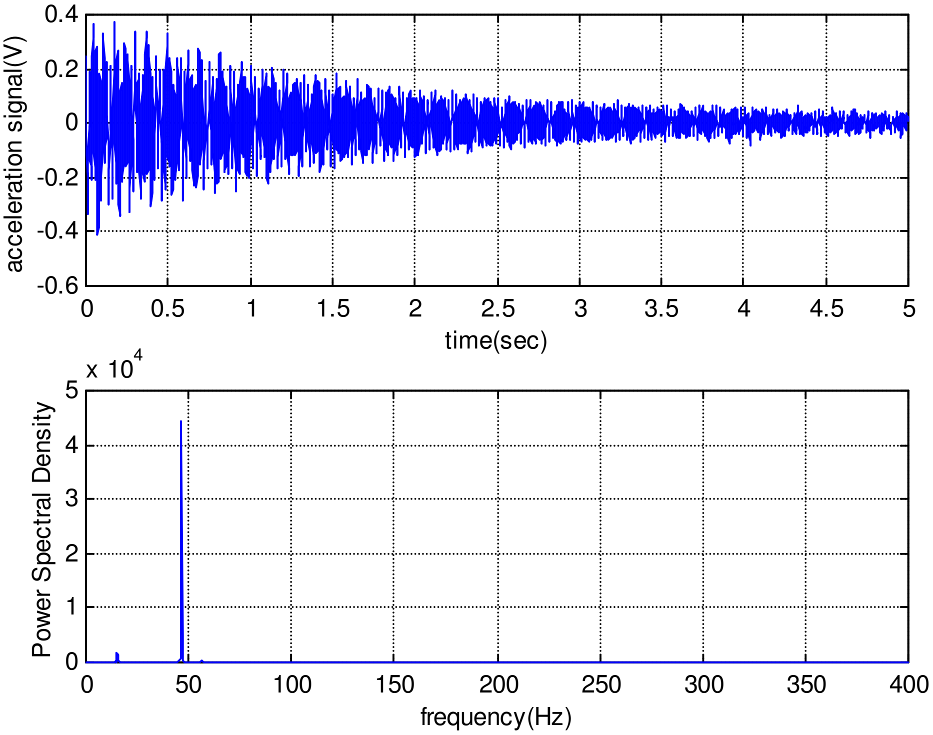

Figure 5.28 Vertical frequency response test result

5.5 CONTROL TEST RESULTS AND DISCUSSIONS

Figure 5.29 shows the laser interferometer position reading when the measurement mirror is fixed to the ground. The standard deviation of the position reading is about 20 nm and the peak-to-peak difference is about 120 nm. Figure 5.30 represents the analytical and experimental PID position control results with 0.1 mm step input. Figure 5.31 shows the analytical and experimental PID position control results with 1 mm step input. Both results show that the analytical model predicts the experimental results very closely. The step response with 0.1 mm input shows under damped behavior.

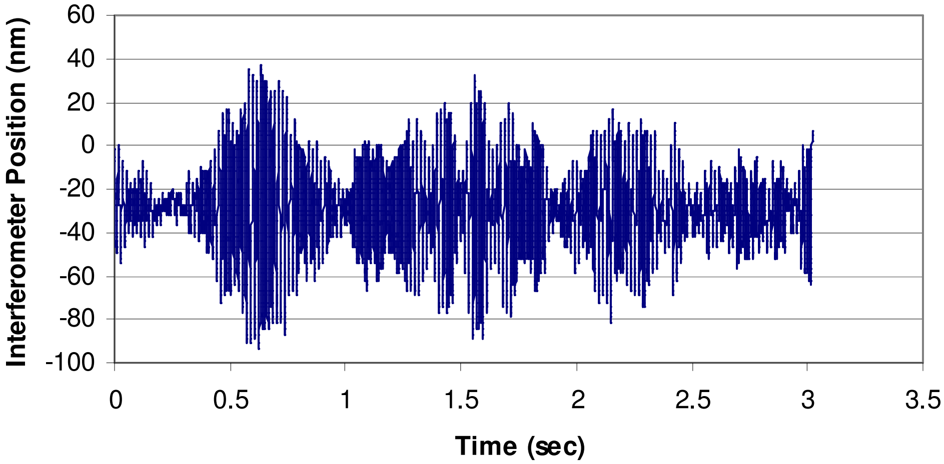

Figure 5.29 Noise of laser interferometer position

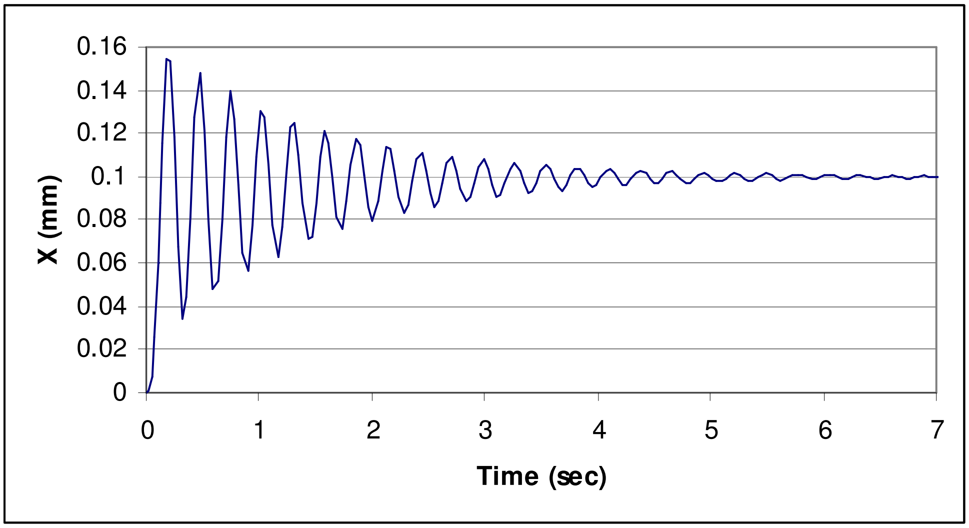

(a) Analytical Result

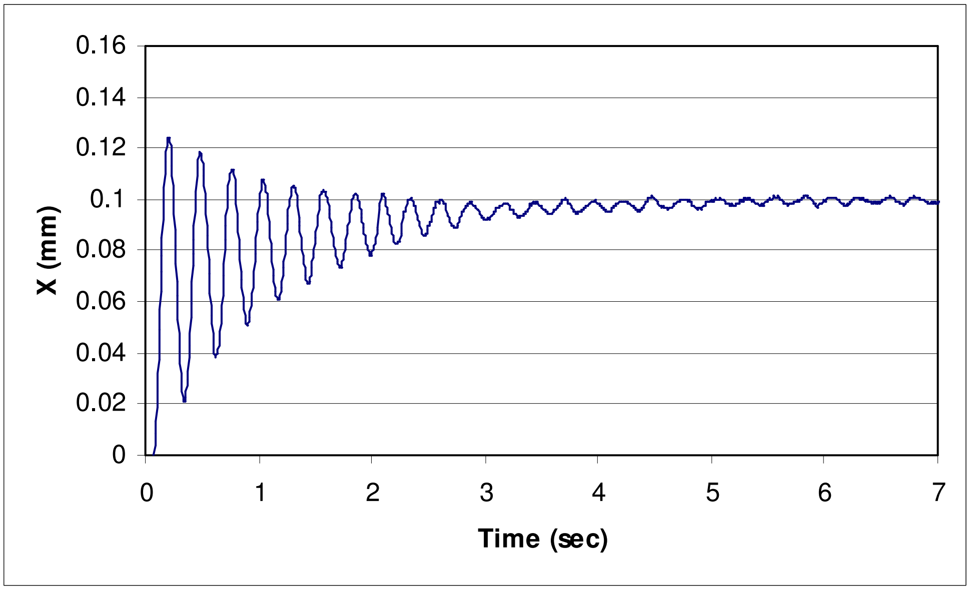

(b) Experimental Result

Figure 5.30 PID Position Control with 0.1 mm Step Input

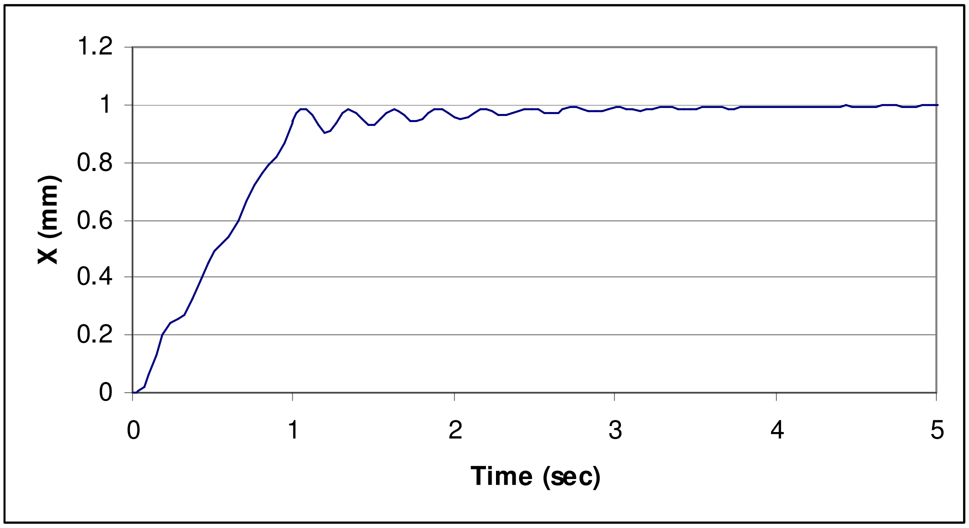

(a) Analytical Result

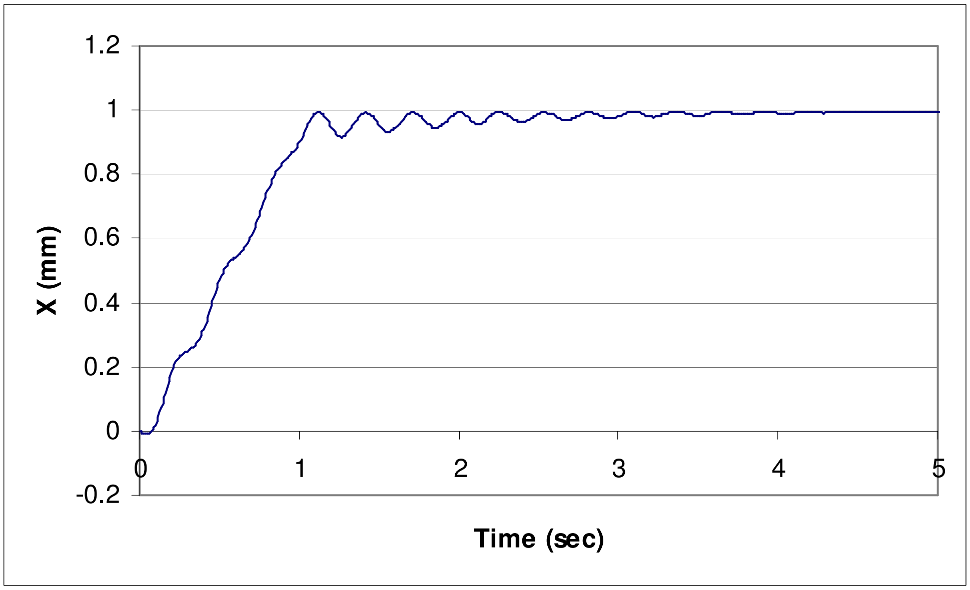

(b) Experimental Result

Figure 5.31 PID Position Control with 1 mm Step Input

The control stability test is performed for the motion axis under several step inputs. Initially the stage is positioned to its home position. The laser interferometer reading is initialized at the home position, and subsequently the stage is programmed to move to the position corresponding to the step input. After the stage is stabilized, the interferometer reading for the X axis is recorded.

Figure 5.32 shows a continuous step positioning of the flexure stage. A 1 mm step is repeated five times and a 5 mm displacement is obtained overall. The standard deviation of the X position is around 1.2~2.3 micron. Figure 5.33 represents the same test results with 10 micron stepwise input. The standard deviation of the X position is around 1.0~1.2 micron. The noise level of the X stage is higher than that of the linear motor test bed. By averaging the laser interferometer position, it can be smoothed as shown in Figure 5.34. The standard deviation of the smoothed positions is around 0.35 micron lower than the raw data. The control resolution of the designed flexure based stage is limited by microscopic vibration which is originated from low damping of the stage. Figure 5.35 shows the analytical results of the flexure stage with different derivative gains. Although the system error is decreased with increased derivative gain, the actual stage does not allow the cases of (b) and (c) because of the position reading noise. The derivative gain (Kd) is a virtual damper created by the controller. Noise can still erroneously be read as speed even when the motor is not moving. With a high Kd value, a minimal noise can be amplified to a high command voltage and hence cause the system to be unstable. Since insufficient damping with the current design limits the applicable control gain and achievable performance, a proper mechanical redesign should correct them in the future.

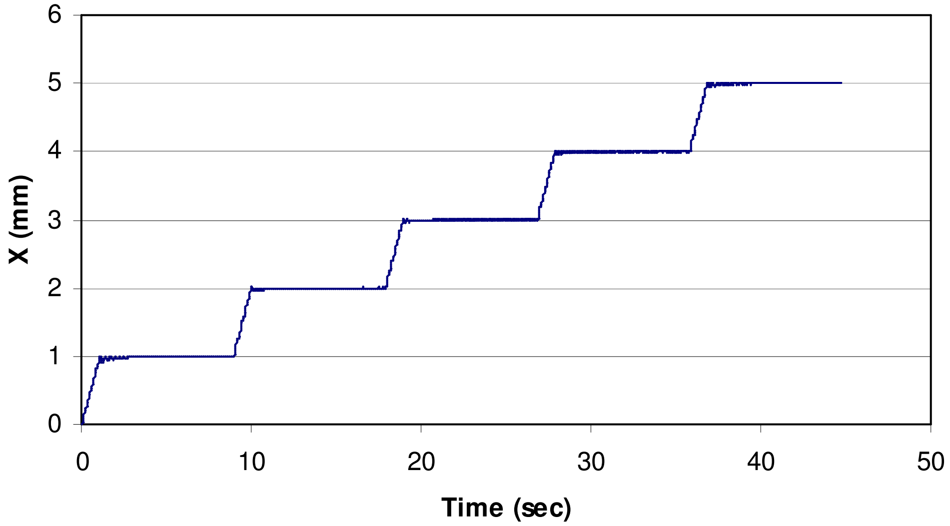

Figure 5.32 Control test result of the X stage with 1 mm step input

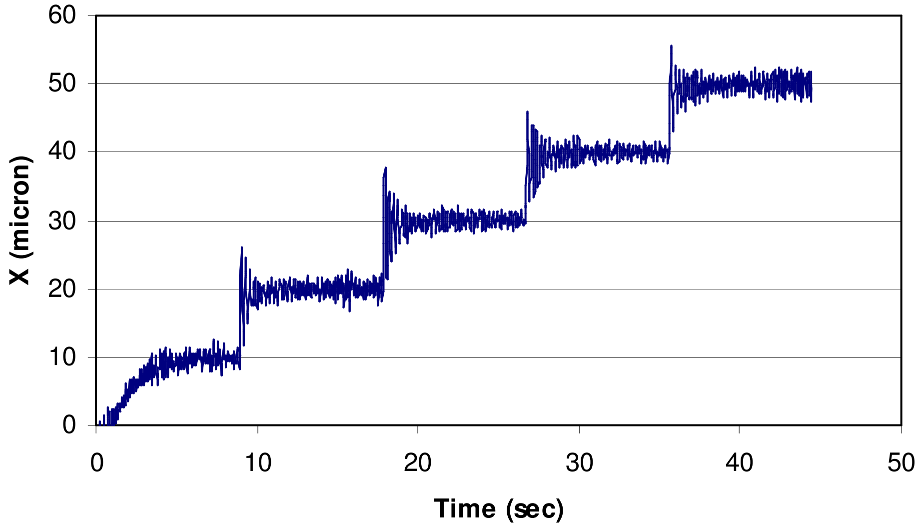

Figure 5.33 Control test result of the X stage with 10 µm step input

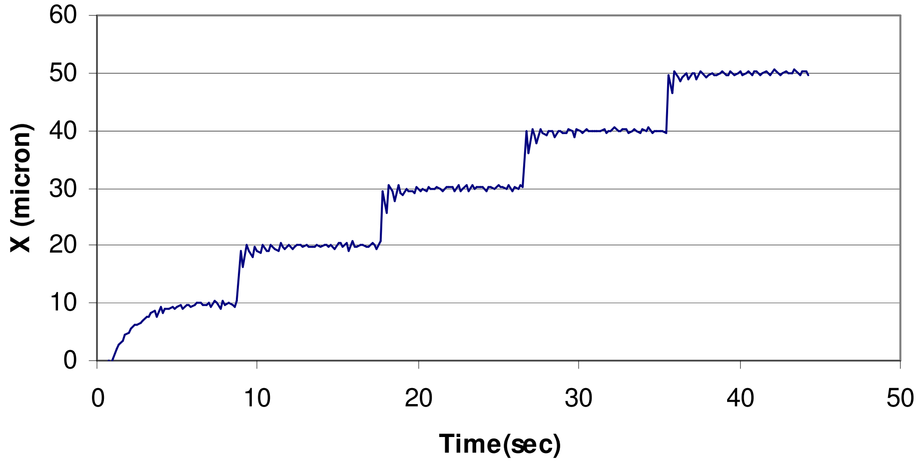

Figure 5.34 Smoothed results of Figure 5.33

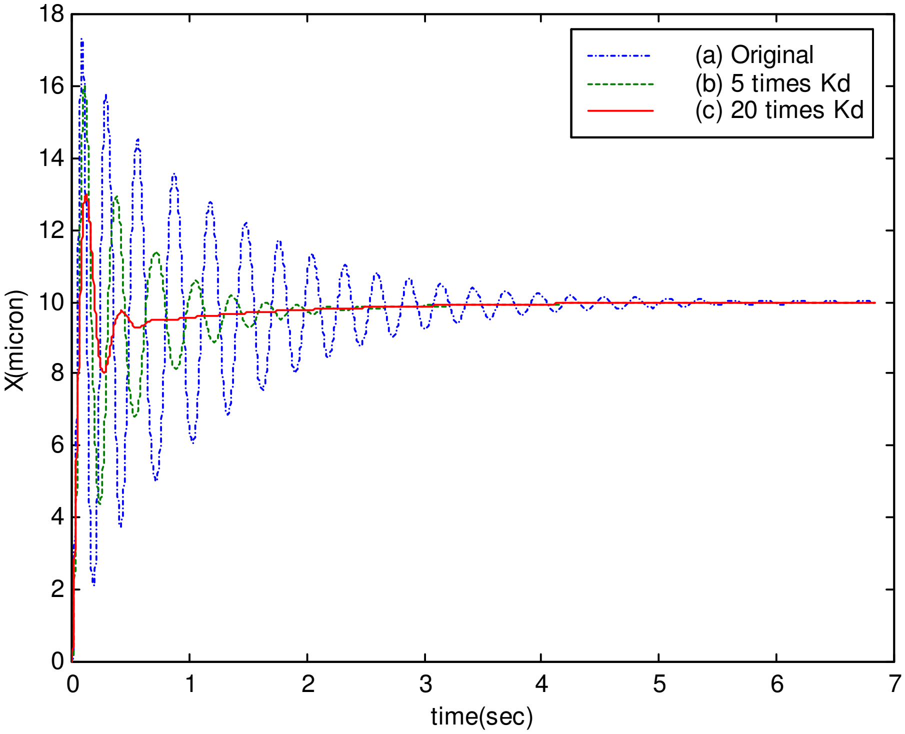

Figure 5.35 Ten microns step input analysis with several derivative gains

The damping coefficient of the stage is less than 0.1, which degrades control performance such as resolution and settling time. Two methods are suggested to increase the damping coefficient of the system. The active damping, the first one, uses a velocity feedback loop inside a position control loop. Since there is no differentiation with a velocity feedback sensor, it gives more stability than PID controller. Figure 5.36 and 5.37 show the analytical results of 10 micron step input responses of the system without and with velocity feedback, respectively. The feedback signal noise is added to both cases. The system with velocity feedback shows much smaller steady state error and faster settling time.

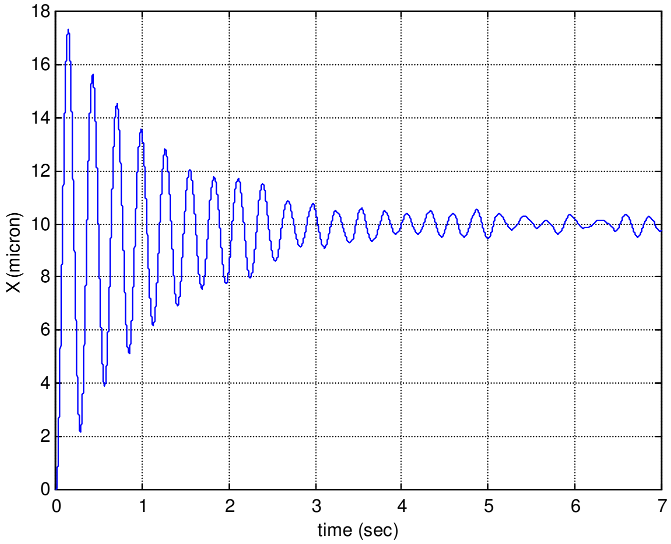

Figure 5.36 Analytical step responses without velocity feedback

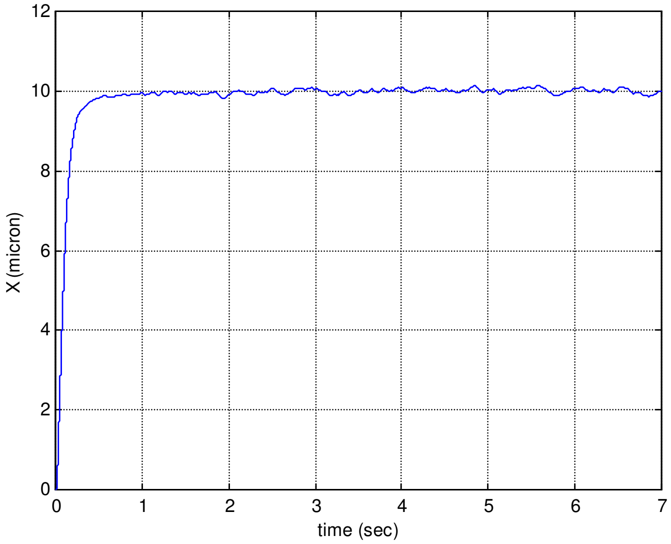

Figure 5.37 Analytical step responses with velocity feedback

The next method, passive damping, requires additional mechanical elements in the stage. Figure 5.38 shows the analytical result of 10 micron step response with passive damper of 5 times more damping than the original system. The control position noise of the system with passive damping is reduced compared to the original system. In order to verify this analytical result experimentally, a simple air cylinder type passive damper is attached to the system as shown in Figure 5.39. The position control test result to 10 micron step inputs is depicted in Figure 5.40. The standard deviation of the position at 30 microns is 0.5 micron lower than 0.7 micron of the original system without passive damper. By averaging the laser interferometer position, it can be smoothed, as shown in Figure 5.41. The standard deviation of the smoothed position at 30 microns is 0.25 micron lower than that of the original system (0.35 micron).

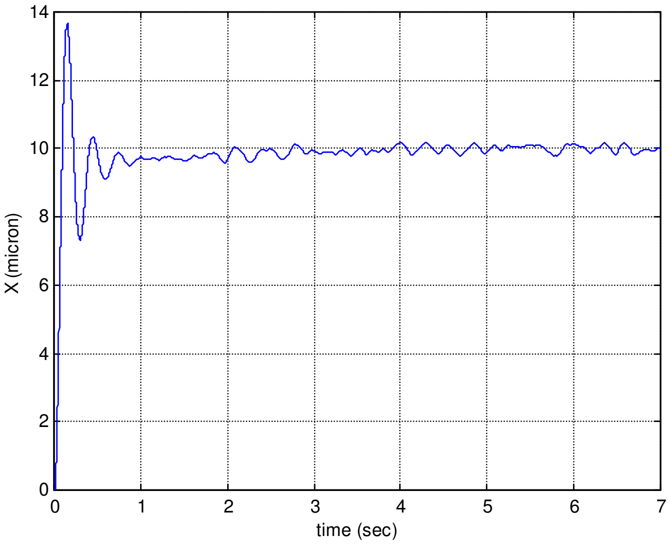

Figure 5.38 Analytical step responses with passive damping

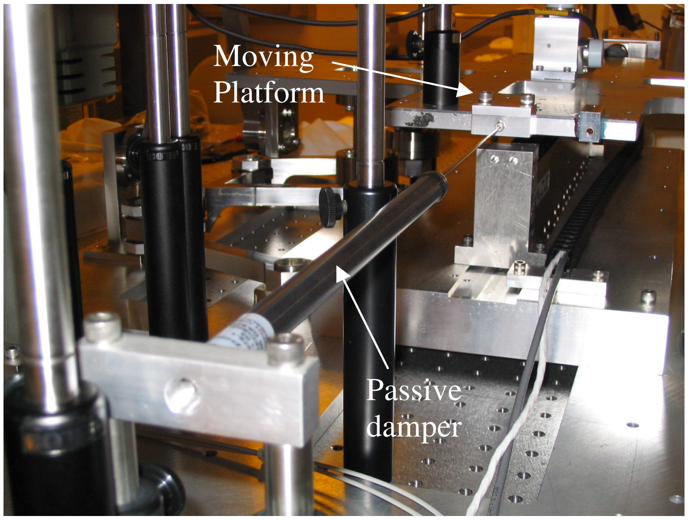

Figure 5.39 Photograph of passive damper installed in the stage

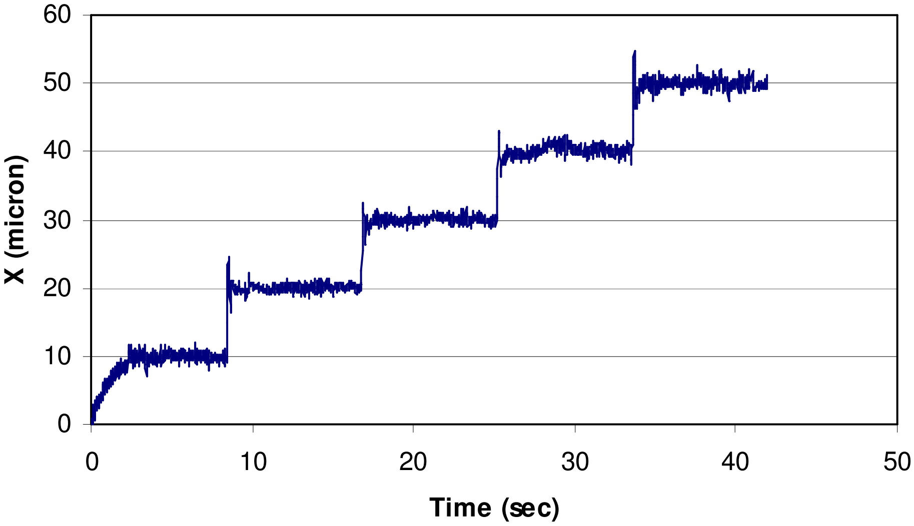

Figure 5.40 Control test result to 10 μm step inputs with a passive damper

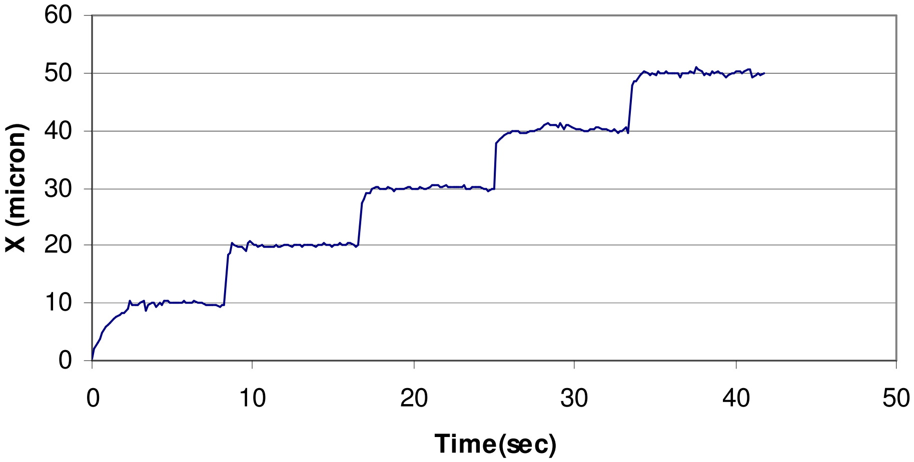

Figure 5.41 Smoothed results of Figure 4.22

One of the possible passive damping mechanisms is a kind of 'paddle in a bucket' configuration depicted in Figure 5.42. The bucket should keep upright because it hold liquid. The bucket can keep upright position and the stage can move horizontally with Scott Russell mechanism shown in Figure 5.43. However, these mechanisms can not be used inside vacuum environments. Coating viscoelastic material on the compliant elements needs to be studied for passive damper operating inside vacuum.

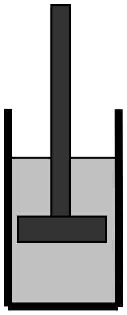

Figure 5.42 Configuration of Paddle in a Bucket

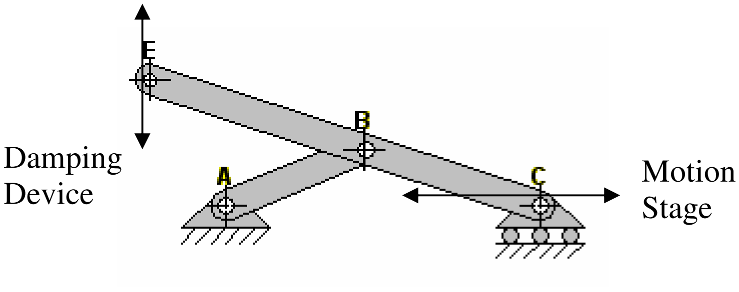

Figure 5.43 Scott Russell Mechanism

Chapter 6: Conclusions and Future Works

6.1 CONCLUSION

A large displacement flexure-based XY positioning stage has been designed for precision equipments in vacuum environments. A double compound notch type small motion rectilinear spring was employed as a basic mechanism to achieve translational motion. Commercially available crossed strip type flexure joints that provide large rotation range were used instead of traditional small displacement flexure joints. The side linkages were added to achieve one degree of freedom translation motion. An unexpected independent mode vibration problem occurred due to undesirable singularities in the mechanism during the preliminary assembly of the proposed motion stage. In order to prevent this vibration, the flexure joints were installed in the off-nominal configuration and the side linkage was modified. The prototype of the single axis flexure based motion stage was fabricated for experimental verification.

Kinematic and static analyses such as center shift analysis, mobility analysis, vertical deflection analysis, and position error analysis were performed. A new equation was suggested to find more accurate results of the center shift of the flexure joints. It predicted the catalog values and the computational results better than the previously developed equations. From the center shift analysis of the flexure joints, it was found that the center shift in the flexure based system is eliminated since the proposed design is a symmetric over-constrained mechanism. In order to verify the mobility of the double compound notch type rectilinear spring mechanism, the first order mobility analysis was performed by using screw system theory. From the mobility analysis, it was found that the mechanism has two degree of freedom. The vertical deflection analysis was performed to predict those errors. Position error analysis was performed to estimate the motion error induced by assembly or manufacturing errors. The yaw error induced by misalignment of linkages was calculated. Since there are a lot of error sources, it is difficult to estimate the position errors analytically.

The equation of motion for the motion stage was derived by using Lagrange's equation both in the nominal configuration and in the off-nominal configuration. Modal analysis was performed to predict the natural frequencies and the control bandwidths of the XY stage. The stage dynamics can be simplified as a simple spring and mass model since the flexure based linkage guide behaves as very close to a linear spring. The linear motor, the amplifier, and the motion controller were selected to control the motion stage. The linear motor test bed was built and tested before attach the linear motor to the actual stage. Then all control hardware including the linear motor was installed in the single axis flexure motion stage. The control stability tests were performed with several step inputs. The motion stage followed the input positions more than 10 micron well, but the low damping of the motion stage caused a slow and oscillatory operation with a small step input less than 10 micron. The damping coefficient of the stage needs to be improved by active and/or passive damping methods since the noise in the position reading does not allow increasing the derivative gain in the PID controller. The analytical results showed that the system with active or passive damping has better control performance and more tolerant to the feedback signal noise. Experimental results by attaching a simple air cylinder type passive damper showed better control performance with lower oscillation.

Horizontal straightness error and yaw were observed experimentally by using the laser interferometer. The somewhat large variation (around 80μm) in straightness was quite repeatable (see Figure 5.6). The variation can be linked to tolerances and a tolerance analysis such as Szarka [2003] can explain this. Variation in link length and variation in the flexure torsional spring rate are potential parameters causing these errors. There are other possible sources such as the surface accuracy in the measurement mirror and the sensor noise, but these errors have the magnitude of only a few hundreds nanometers. The repeatability tests were also performed since such errors can be eliminated by using a look-up table if undesirable lateral or vertical motion errors are repeatable. The straightness error and yaw test results showed very repeatable behavior. The stage showed a relatively large horizontal straightness repeatability error of 3.9 micron (3σ), but the stage has a very excellent yaw repeatability of 4.5 μ-radian. Since the low lateral stiffness of the current stage caused relatively large straightness repeatability error, modified designs such as buckled strips or Peaucellier linkage based mechanism were proposed to improve it. The laser interferometer setup was modified to measure the vertical deflection and pitch errors. The repeatability of the vertical deflection of the motion stage was less than 0.84 micron (3σ) which was better than the horizontal case. The stage showed a very excellent pitch repeatability of 2.97 μ-radian. Therefore, the stage has very excellent angular error repeatabilities in both yaw and pitch. Modal impact tests by using accelerometers were performed to find the resonant frequencies in the lateral and vertical direction. The lateral stiffness needs to be increased to raise the natural frequency, which supports the horizontal straightness repeatability test result.

This research is, to our knowledge, the first work for developing a macro motion stage that can support the weight of the stage and guide the motion by a mechanism based on flexure joints. Existing flexure-based translation stages usually have motion range to size ratio of less than 0.01 as compared 0.5 or higher in this research. It is believed that these large motion stages can be a cost-effective solution for semiconductor applications, particularly the ones that operate in vacuum. Especially flexure-based XY stages can be potentially used to accurately place photomasks and wafers in an electron beam lithography machine, semiconductor steppers, wafer handling equipment, defect analysis machines in semiconductor industry, chip inspection tools, and coordinate measuring machines.

6.2 CONTRIBUTIONS

The research contributions of this dissertation are listed below:

- Kinematic synthesis techniques were extended to the design of fully flexure-based motion stage. Large body of literature exists in classical linkages and small motion flexures, but there is almost no literature in large motion flexures.

- Symmetry and over-constraint was utilized to obtain better precision performance and singularity due to symmetry was overcome.
- An experimental characterization test-bed was developed to effectively compare air bearing technology to the new design developed in this dissertation to evaluate stage feasibility particularly for vacuum application.
- It was observed that stiffness parameters of the stage were correlated to system repeatability.
- Problems with low damping and internal strain energy were identified as it relates to feedback control and passive damping approach was used to improve the control performance.

6.3 FUTURE WORK

Since the current motion stage has low damping, active and/or passive damping methods need to be implemented to improve control performance. Analytically both the active damping and the passive damping improve the control performance and are also much more tolerant to the position reading noise. It is suggested to use a velocity feedback loop inside position control loop as an active damping method. A kind of 'paddle in a bucket' configuration is proposed as a passive damping mechanism, but it can not be used inside vacuum. Coating viscoelastic material on the compliant elements can be another candidate for passive damping. There are several design requirements for passive dampers. It should not introduce friction and should be operable inside vacuum. The actual hardware for active and/or passive damping control needs to be implemented to improve the overall control performance of the motion stage in the future.

A few modified designs are suggested to increase the lateral stiffness of the current motion stage. Adding a stack of buckled strips is proposed to increase the lateral stiffness. A motion stage using Peaucellier linkage is also suggested to improve the lateral stiffness. Since the motion stage using Peaucellier linkage has a large footprint compared to the commercial air bearing stages, decreasing the footprint is challenging work.

Since only the single axis motion stage was developed in this research, it is necessary to fabricate a complete flexure based XY motion stage in the future. The motion controller should include the lookup table of each motion stage in the XY stage.

Another suggestion as a future work is to design a flexure XY stage that is actuated by a planar motor. A planar motor consists of a light movable block, a platen base, and a driver block. Since planar motors have light weight and compact structure, it is very attractive as an actuator in the flexure based motion stage. It is necessary to design a new flexure based linkage mechanism to allow two degree of freedom motion. The new mechanism needs to have small vertical gap differences through the whole range of motion and generate small angular moments.

References

[1] Arai, T, Larsonneur, R., and Jaya, Y.M., 1993, "Calibration and Basic Motion of a Micro Hand Module," Proc. of the IECON '93, Maui, Hawaii, pp.1660-1665.

[2] Bisschops, T. and Vijfvinkel, J., 2001, "Large Ultra-precision Motion Feedthrough Designs," Vacuum 60, pp. 161-165.

[3] Formica, Mike, 2001, "Linear Motors Aid High-Volume Manufacture of Fiberoptic Devices," Laser Focus World, October 2001, pp. 103-106.

[4] Goldfarb, Michael and Speich, John E., 1998, "Compliant Micromanipulator Design for Scaled Bilateral Telemanipulation of Small-Scale Environments," ASME, Dynamic Systems and Control Division (Publication) DSC, Vol. 64, pp. 213-218.

[5] Goldfarb, Michael and Speich, John E., 1999, "A Well-Behaved Revolute Flexure Joint for Compliant Mechanism Design," Journal of Mechanical Design, Vol. 121, pp. 424-429.

[6] Haringx JA., 1949, "The Cross Spring Pivot as a Constructional Element," App. Sci. Res. A, Vol. 1, No. 4, pp. 313-332.

[7] Hunt KH., 1990, "Kinematic Geometry of Mechanisms," Oxford Engineering Science Series, Clarendon Press, Oxford, UK.

[8] Kim, W.-J. and Trumper, D.L., 1998, "High-Precision Magnetic Levitation Stage for Photolithography," Precision Engineering, Vol. 22, No. 2, April, pp. 66-77.

[9] Lee, Chang-Woo and Kim, Seung-Woo, 1997, "Ultraprecision Stage for Alignment of Wafers in Advanced Microlithography," Precision Engineering, Vol. 21, No. 2-3, pp. 113-122.

[10] Lee, D.S., Pahk, J.H., and Pahk, H.J., 1998, "Ultra Precision Positioning System for Servo Motor-Piezo Actuator Using the Dual Servo Loop and Digital Filter Implementation," Proc. ASPE, Vol. 18, pp. 287-290.

[11] Lucas Aerospace, 1999, "Free-Flex Pivot Catalog."

[12] Novak et al., 2000, “Nikon Electron Projection Lithography System: Mechanical and Metrology Issues,” ASPE 2000 Annual Meeting, Vol.22, pp. 517-520.

[13] Ohya, Y., Arai, T., Mae, Y., Inoue, K., and Tanikawa, T., 1999, “Development of 3-DOF Finger Module for Micro Manipulation,” Proc. IEEE Int. Conf. on Intelligent Robots and Systems, Kyongju, Korea, pp.894-899.

[14] Paros, J.M. and Weisbold, L., 1965, “How to Design Flexure Hinges,” Machine Design, pp. 151-156.

[15] Physik Instrumente, June 18, 2001, “The PI Online-Catalog,” Online Internet, Available on http://www.physikinstrumente.com/

[16] Rong, Yiming, Zhu, Yaoxiang, Luo, Zhenbi, and Liu, Xiangxi, 1994, “Design and Analysis of Flexure-Hinge Mechanism Used in Micro-Positioning Stages,” ASME, Production Engineering Division (Publication) PED 68-2, pp. 979-985.

[17] Ryu, J.W., Gweon, D.G., and Moon, K.S., 1997, “Optimal Design of a Flexure Hinge Based XYθ Wafer Stage,” Precision Engineering, Vol.21, pp. 18-28.

[18] Shamoto, Eiji and Moriwaki, Toshimichi, 1997, “Rigid XYθ Table for Ultraprecision Machine Tool Driven by Means of Walking Drive,” CIRP Annals - Manufacturing Technology V.46 N.1, pp. 301-304.

[19] Slocum, Alexander H., 1992, “Precision Machine Design: Macromachine Design Philosophy and Its Applicability to the Design of Micromachines,” Proceedings of the IEEE Micro Electro Mechanical Systems Workshop, pp. 37-42.

[20] Smith, S. T. and Chetwynd D.G., 1992, “Foundations of Ultraprecision Mechanism Design,” Gordon and Breach Science Publishers, Montreux, Switzerland.

[21] Smith ST., 2000, “Flexures,” Gordon and Breach Science Publishers, Amsterdam, The Netherlands.

[22] Sprenger, Bernhard and Siegwart, Roland, 1998, “Novel High Speed 3 DOF Linear Direct Drive Operating with Submicron Precision,” SPIE, Vol.3202, pp. 78-85.

[23] Szarka, Sara L., 2003, “Tolerance Analysis of a Nano-Precision Large Displacement Flexure-Based Overconstrained Planar Mechanism,” M.S. Thesis, The University of Texas at Austin.

[24] Tajbakhsh, H., Hale, L. Malsbury, Jensen, S., and Parker, J., 1998, “Three-Degree-of-Freedom Optic Mount for Extreme Ultraviolet Lithography,” Proc. ASPE, Vol. 18, pp. 359-362.

[25] Tomita, Yoshiyuki, Kodaira, Kazuho, Satoh, Fumiaki, Itoh, Kazuhiro, and Koyanagawa, Yasushi, 1992, “6-Axes Motion Control Method for Parallel-Linkage-Type Fine Motion Stage,” Journal of the Japan Society of Precision Engineering/Seimitsu Kogaku Kaishi, Vol. 58, No. 4, pp. 684-690.

[26] Tomita et al., 1996, “High-Response X-Y Stage System Driven by In-Parallel Linear Motors,” Annals of the CIRP, Vol.45/1, pp. 359-362.

[27] Troeger, H., 1962, “Considerations in the Application of Flexural Pivots,” Vol.17, No.4, Automatic Control Data Systems Engineering.

[28] Yang, Renyi, Jouaneh, Musa, and Schweizer, Rudolph, 1996, “Design and Characterization of a Low-profile Micropositioning Stage,” Precision Engineering, Vol.18, pp. 20-29.

[29] Williams, Mark, Faill, Peter, Bischoff, Paul M., Tracy, Steven P., and Arling, Bill, 1997, “Six Degrees of Freedom Mag-Lev Stage Development,” Proceedings of SPIE - The International Society for Optical Engineering, Vol. 3051, pp. 856-867.

Vita

Yeong-jun Choi was born in Daegu, Korea on January 17, 1968, the second son of Malh-soo Choi and Wang-kye Ha. After completing his work at Daegun High School at Daegu, Korea, in 1987, he entered The Korea Advanced Institute of Science and Technology in Daejon, Korea. He received the degree of Bachelor of Science in Mechanical Engineering in February 1991 and the degree of Master of Science in Precision Engineering in February 1993 from The Korea Advanced Institute of Science and Technology. During the following years he was employed as a research engineer at the Agency for Defense Development in Daejon, Korea. In August 1998, he entered the graduate school of The University of Texas at Austin to pursue his Doctor of Philosophy degree in Mechanical Engineering.

Permanent address: Eupnae-Dong Hyundai Apt. 111-904,
Sosan, Choong-Nam, Korea, 356-763

This dissertation was typed by Yeong-jun Choi.